PONTIFICIA
UNIVERSIDAD
CATÓLICA
DE CHILE

FACULTAD DE FÍSICA
INSTITUTO DE FÍSICA

An extensive study of models beyond the Standard Model

by

IVANIA MATURANA ÁVILA

Thesis inform presented to Instituto de Física of
Pontificia Universidad Católica de Chile, as requirement
to obtain the degree of PhD in Physics.

Advisor	:	Dr. Marco Aurelio Díaz (Física PUC, Chile)
Thesis Commitee	:	Dr. Benjamin Koch (Física PUC, Chile)
	:	Dr. Diego Aristizabal (Física UTFSM, Chile)

June 1, 2020 Santiago, Chile

"Of course it is happening inside your head, Harry, but why on earth should that mean that it is not real??"

Albus Dumbledore

Harry Potter

Acknowledgements

First, I would like to thanks to my family, especially to my grandparents for all the support that they give it to me during my carrier.

Second, I thanks my friends, those ones that I have met during the different periods of my life.

To Stefano, for making gray days turn sunny.

I would also like to thanks to my mates from Pontificia Universidad Católica de Chile (PUC), especially to members of **Mujeres en Física**.

I am very grateful to the members of my thesis committee and to the professors and the administrative personal from PUC. Particularly, I would like to thanks my advisor Dr. Marco Aurelio Díaz for all the advice that he gives me during the PhD period related to life and good practices on science.

Thanks to the AHEP group at Valencia especially to Dr. Valentina De Romeri. I would also like to thanks my friends and teachers of aerial acrobatics from Espai órbita in Valencia, Spain.

I cannot forget those women who have been doing science before me. Many thanks to them, especially those ones who fought in the past to bring the opportunity to women to practice and study science. Many thanks to the current women scientist that continue fighting to do science a more inclusive place with respect to gender equality.

This thesis was supported by ANID, Doctorado Nacional (2015) num. 21151255.

Abstract

The present work focused on the phenomenological study of tree extensions of the standard model: the Inert Higgs Doublet Model (IHDM), the Scotogenic model, and the Singlet + Triplet Scotogenic model (STSM). The motivations of these models imply physics beyond the Standard Model where some of the current open questions in physics can be explained. In all of them, we have considered a freeze-out scenario where the dark matter candidate is a scalar weak interactive massive particle (WIMP).

The first part of this work is related to the study of the main differences between the IHDM and the Scotogenic Model. We did a deep study about the dark matter phenomenology in both where we investigated results that survive to the main theoretical constraints and that can also be a candidate of dark matter, explaining the total dark matter abundance that exists in the Universe. We have studied a specific signal at the compact Linear Collider (CLIC) and we investigated the parameters that will contribute to different values in the cross-section of the Scotogenic Model in comparison with the one of the IHDM.

In the second part, we have reexamined the Singlet + Triplet Scotogenic Model which generalizes the original idea introduced in the simple Scotogenic model, making its phenomenology viable and substantially richer. The presence of singlet and triplet fermions automatically leads to two oscillation lengths associated with solar and atmospheric oscillations and leaving a massless neutrino. We did a more detailed phenomenological study of the scalar dark matter candidate updating the main constraints. We have investigated direct detection of dark matter in the current experiments and we have done an analysis of indirect probes via gamma-rays. Further, we realized a new collider study with relevant implications for future Large Hadron Collider (LHC) searches with higher luminosity.

Resumen

El presente trabajo se centró en el estudio fenomenológico de tres modelos que son extensiones del actual Modelo Estandar: El *Inert Higgs Doublet Model*, el *Scotogenic Model* and el *Singlet + Triplet Scotogenic Model*. La motivación de estudiar estos modelos se basa en que pueden explicar algunas de las preguntas existentes en física hoy en día; todos ellos presentan una particula que será candidato a materia oscura y los últimos dos proponen un mecanismo para dar masa a al menos dos neutrinos. En todos los modelos hemos considerado la generación de la abudancia de materia oscura en un escenario de *freeze-out* y la partícula candidata a materia oscura será un escalar massivo debilmente interactuante (WIMP definido por su nombre en inglés).

El primer trabajo está relacionado con estudiar las principales diferencias entre el *Inert Higgs Doiblet Model* and el *Scotogenic Model*. Hemos realizado un estudio profundo de la materia oscura en ambos, investigando puntos que sobrevivan a las cotas mas fuertes en física y en los actuales experimentos y también considerando que estos resultados pueden explicar la densidad de materia oscura en el Universo en su totalidad. Estudiando una señal expecífica en el *Compact Linear Collider* (CLIC), investigamos los parametros que contribuirán a obtener diferentes valores para la sección eficaz en ambos modelos.

En el segundo trabajo, hemos reexaminado el *Singlet + Triplet Scotogenic Model* el cual generaliza la idea introducida en el *Scotogenic model* simple, haciendo su fenomenología viable y mucho mas rica. Relalizamos un estudio fenomenológico detallado de la materia oscura escalar, actualizando las cotas actuales de los experimentos. Investigamos la detección directa de dark matter y la detección indirecta vía rayos gamma. Además, realizamos un estudio en colisionadores el cual tendrá relevantes implicaciones para las futuras búsquedas a alta luminosidad del *Large Hadron Collider* (LHC definido por su nombre en inglés).

Contents

List of Figures

List of Tables

1

The dark side of the Universe

"Every real story is a never ending story."

Michael Ende

The Neverending Story

To introduce the object of study in this thesis we must to do a review about the history of our Universe and to give an introduction about the main problems presented in the Standard Model due to the recent experimental results and astronomical observations.
This chapter will aboard a brief introduction of our early and present Universe and will point the open questions in physics remarking those that will be approached on this thesis.

1.1 A brief introduction to standard cosmology

1.1.1 The main parameters to understand our story

Over the years, scientists have been interested to determine the matter density of the Universe. One of the reasons is related to curiosity: find out what the Universe is made of. To understand the story of our Universe is important to define three main parameters:

The Hubble constant: it is the constant that describes the expansion of the Universe. If we fix two points in the Universe, these will move away from each other with a velocity that is proportional to their current distance r. The Hubble law is defined as [1]

$$\begin{aligned} H_0 &:= \frac{\dot{r}}{r} \approx 70 \frac{\text{km}}{\text{s Mpc}} \\ &= 1.5 \cdot 10^{-33} \text{ eV} \end{aligned} \tag{1.1}$$

A dimensionless parameter h can be written as

$$h := \frac{H_0}{100 \frac{\text{km}}{\text{s Mpc}}}. \tag{1.2}$$

In this way the Hubble "constant" is defined at a current point in time.

The cosmological constant: it describes most of the energy content in the Universe. This energy is defined through the gravitational Einstein-Hilbert action [28]. The cosmological constant Λ can also be related with the Hubble constant through a dimensionless parameter

$$\Omega_\Lambda := \frac{\Lambda}{3H_0^2}. \tag{1.3}$$

The matter content of the Universe: Over the years, scientists have been interested to determining the matter density of the Universe. We also know that the matter content changes with time. We

[1] In this thesis we will considered $\hbar = c = 1$.

can define

$$\Omega_m \coloneqq \frac{\rho_m}{\rho_c}, \tag{1.4}$$

$$\Omega_r \coloneqq \frac{\rho_r}{\rho_c}, \tag{1.5}$$

where ρ_m is defined as a mass density, ρ_r as the radiation density and ρ_c as the critical density separating an expanding from a collapsing Universe with $\Lambda = 0$. Today, we can separate the matter content present in the Universe. The dimensionless parameter that represent the non-relativistic baryonic matter content of the Universe is defined as

$$\Omega_b \coloneqq \frac{\rho_b}{\rho_c}. \tag{1.6}$$

The remain matter content is dark matter, which we define as $\Omega_\chi \coloneqq \Omega_m - \Omega_b$.

1.1.2 The dynamics of the Universe expansion

Our isotropic and homogeneous Universe can be described in terms of the Friedman-Lemaitre-Robertson-Walker (FLRW) metric

$$ds^2 = dt^2 - a^2(t)\left(\frac{dr^2}{1-kr^2} + r^2(d\theta^2 + \sin\theta \mathrm{d}\phi^2)\right) = g_{\mu\nu}dx^\mu dx^\nu. \tag{1.7}$$

The constant k corresponds to the spatial curvature. If $k = 0$ we have a flat Universe while for $k = -1$ and $k = +1$ we have a negative and positive curvature, respectively.
The Christoffel symbols are used to connect nearby tangent spaces and, in terms of the partial derivatives of the components of the metric tensor $\mathbf{g}$, can be defined as

$$\Gamma^\mu_{\nu\lambda} = \frac{1}{2}g^{\mu\sigma}(g_{\sigma\nu,\lambda} + g_{\sigma\lambda,\nu} - g_{\nu\lambda,\sigma}), \tag{1.8}$$

The scale parameter $a(t)$ defined in equation 1.7 controls the expansion of the Universe. More specifically, as we see in the last section the Hubble parameter can be defined similar to equation 1.1 as $H \equiv \frac{\dot{a}(t)}{a(t)}$, which encodes the rate at which the Universe is expanding. Thinking in an Universe dominated by radiation the Hubble parameter is $H = 1.66 g_*^{1/2}\frac{T^2}{M_P}$, where $M_P = 1.22 \times 10^{19}$ [GeV] is Planck's energy. We can also define a dimensionless parameter with $x = m/T$, where m will be the mass parameter of the dark matter. This yields to

$$H(m) = 1.66 g_*^{1/2}\frac{m^2}{M_P} = Hx^2, \tag{1.9}$$

where

$$g_* = \sum_{bosons} g\left(\frac{T_i}{T}\right)^4 + \frac{7}{8}\sum_{fermions} g\left(\frac{T_i}{T}\right)^4 \tag{1.10}$$

is the effective number of relativistic degrees of freedom. These number of degrees of freedom are counted by a factor g specific for each particle taking into account for example the color, the spin and the anti-

partcile [28].Here T and T_i are the temperture of the plasma in equilibrium and the effective temperture of each species, respectively. In order to be able to compute the relic density of the dark matter today, we must compute the time evolution of the number density of dark matter particles. The phase space distribution function f can describe the occupancy number in phase space for a given particle in kinetic equilibrium. Also it is different for fermions and bosons [29],

$$f = \frac{1}{e^{(E-\mu)/T} \pm 1}, \tag{1.11}$$

where the sign $(+)$ corresponds to fermions and the sign $(-)$ corresponds to bosons. E represents the energy and μ the chemical potential. We can integrate part of the phase space and calculate a series of observables in the Universe defined by the next expressions:

$$n = \frac{g}{(2\pi)^3} \int f(\mathbf{p}) d^3p, \tag{1.12}$$

$$\rho = \frac{g}{(2\pi)^3} \int E(\mathbf{p}) f(\mathbf{p}) d^3p, \tag{1.13}$$

$$p = \frac{g}{(2\pi)^3} \int \frac{|\mathbf{p}|^2}{3E(\mathbf{p})} f(\mathbf{p}) d^3p. \tag{1.14}$$

which represent the **number density of particles**, the **energy density** and the **pressure**, respectively.

An expanding Universe can be defined as a closed system and when it is in thermal equilibrium the total entropy is conserved

$$TdS = d(pV) + pdV = d((\rho + p)V) - Vdp = 0, \tag{1.15}$$

where $d((\rho + p)V) = Vdp$ and the entropy density $s = S/V = (\rho + p)/T$. Since the evolution of the Universe is isoentropic, the entropy density can be defined as $s = S/a^3$. Applying the last equation corresponding to the number density of particles [30], we define the yield

$$Y = \frac{n}{s}, \tag{1.16}$$

that in the absence of number-changing process, it will become a constant.
The evolution of the entropy density as a function of the temperature is given by

$$s = \frac{2\pi^2}{45} g_{*s} T^3. \tag{1.17}$$

where

$$g_{*s} = \sum_{bosons} g \left(\frac{T_i}{T}\right)^3 + \frac{7}{8} \sum_{fermions} g \left(\frac{T_i}{T}\right)^3 \tag{1.18}$$

is the effective number of relativistic degrees of freedom for entropy. Also the energy density can be written as

$$\rho = \frac{\pi^2}{30} g_* T^4, \tag{1.19}$$

where g_* is given by equation 1.10.
Solving the integral for the number density of particles explicitly for relativistic particles, we get

$$n = \frac{g_{\text{eff}}}{\pi} \zeta(3) T^3, \tag{1.20}$$

where $g_{\text{eff}} = g$ for bosons and $g_{\text{eff}} = (3/4)g$ for fermions. Here we are considering that $E = |\mathbf{p}|$ in the relativistic limit, and the integrals $\int_0^\infty p^2(e^p - 1)dp = 2\zeta(3)$ and $\int_0^\infty p^2(e^p + 1)dp = 3\zeta(3)/2$ in terms of the Riemann's Zeta functions
In the case of non-relativistic particles, when we solve the integral of the number density of particles we get

$$n = g \left(\frac{mT}{2\pi}\right)^{3/2} e^{-m/T}. \tag{1.21}$$

For both scenarios we can use equation 1.16 and the Yields at equilibrium as $Y^{\text{R}}_{\text{eqq}}$ for relativistic particles and $Y^{\text{NR}}_{\text{eqq}}$ for non-relativistic particles will read

$$Y^{\text{R}}_{\text{eqq}} = \frac{45}{2\pi^4} \zeta(3) \frac{g_{\text{eff}}}{g_{*s}} \approx 0.278 \frac{g_{\text{eff}}}{g_{*s}}, \tag{1.22}$$

$$Y^{\text{NR}}_{\text{eqq}} = \frac{45}{2\pi^4} \left(\frac{\pi}{8}\right)^{1/2} \frac{g}{g_{*s}} \left(\frac{m}{T}\right)^{3/2} e^{-m/T}. \tag{1.23}$$

1.1.3 Time evolution of the number density

The Liouville operator is defined as

$$\hat{L} = p^\mu \frac{\partial}{\partial x^\mu} - \Gamma^\mu_{\sigma\rho} p^\sigma p^\rho \frac{\partial}{\partial p^\mu}. \tag{1.24}$$

The evolution of the number density operator can be computed by applying the covariant form of the last operator to the corresponding phase distribution function,

$$\hat{L}[f] = C[f], \tag{1.25}$$

where $C[f]$ is the **collisional operator**, which takes into account the processes where the number of particles will change, as decays or annihilations[2].

[2]For the expression of the Liouville operator we have used the geodesic equation $\frac{dp^\mu}{d\tau} = \frac{d^2x^\mu}{d\tau^2} = -\Gamma^\mu_{\sigma\rho} p^\sigma p^\rho$. In the equation 1.24 gravity enters by the related connection,$\Gamma^\mu_{\sigma\rho}$ connection

In the case of a FRW Universe, where $f(x^\mu, p^\mu) = f(t, E)$, we have

$$\begin{aligned}\hat{L} &= E\frac{\partial}{\partial t} - \Gamma^0_{\sigma\rho}p^\sigma p^\rho \frac{\partial}{\partial E} \\ &= E\frac{\partial}{\partial t} - H|\mathbf{p}|^2\frac{\partial}{\partial E},\end{aligned} \tag{1.26}$$

where $H = \dot{a}/a$. If we integrate (1.25) over the momentum space we have

$$\frac{g}{(2\pi)^3}\int \frac{\hat{L}[f]}{E}d^3\mathbf{p} = \frac{g}{(2\pi)^3}\int \frac{C[f]}{E}d^3\mathbf{p}. \tag{1.27}$$

Performing some calculations the last equation reads

$$\frac{dn}{dt} + 3Hn = \frac{g}{(2\pi)^3}\int \frac{C[f]}{E}d^3\mathbf{p}. \tag{1.28}$$

The collisional operator $C[f]$ also incorporates all number-changing processes that create or deplete particles in the thermal bath. When there are no number changing dark matter interactions $C[f] = 0$. Considering only in annihilation processes [31], Standard Model particles (A, B) can annihilate to form a pair of dark matter particles labeled as χ_1, χ_2, or vice-versa (i. e. $A, B \leftrightarrow \chi_1, \chi_2$). The phase space corresponding to each particle is defined as

$$d\Pi_i = \frac{g_i}{(2\pi)^3}\frac{d^3\mathbf{p}_i}{2E_i}, \tag{1.29}$$

from where we can calculate the collision term as

$$\begin{aligned}\frac{g}{(2\pi)^3}\int \frac{C[f]}{E}d^3\mathbf{p} = &- \int d\Pi_A d\Pi_B d\Pi_{\chi_1} d\Pi_{\chi_2}(2\pi)^4\delta(p_A + p_B - p_{\chi_1} - p_{\chi_2}) \\ &[|\mathcal{M}_{\chi_1\chi_2\leftrightarrow AB}|^2 f_{\chi_1} f_{\chi_2} - |\mathcal{M}_{AB\leftrightarrow\chi_1\chi_2}|^2 f_A f_B].\end{aligned} \tag{1.30}$$

In order to reduce this expression to a more manageable form we can do the following assumptions [18]:

- First we have to consider that the temperature of each species satisfies $T_i << E_i - \mu_i$ with μ_i the chemical potential. Since they follow the Maxwell-Boltzmann distribution, $(1 \pm f) \sim 1$ and statistical mechanical factors in the calculation can be ignored.
- The kinetic equilibrium is maintained in order to have the phase-distribution in terms of the Fermi-Dirac or the Bose-Einstein forms.
- The Standard Model particles interacting are in thermal equilibrium with the photon bath.

According to the last considerations, assuming no CP violation in the dark matter sector

$$|\mathcal{M}_{\chi_1\chi_2\to AB}|^2 = |\mathcal{M}_{AB\to\chi_1\chi_2}|^2 \equiv |\mathcal{M}|^2.$$

Because of energy conservation in the annihilation process we have $E_A + E_B = E_{\chi_1} + E_{\chi_2}$, thus

$$f_A f_B = f_A^{eq} f_B^{eq} = e^{-\frac{E_A+E_B}{T}} = e^{-\frac{E_{\chi_1}+E_{\chi_2}}{T}} = f_{\chi_1}^{eq} f_{\chi_2}^{eq}. \tag{1.31}$$

Due to Standard Model particles are in equilibrium we have

$$\frac{g}{(2\pi)^3}\int \frac{C[f]}{E} d^3\mathbf{p} = -\langle\sigma v\rangle(n^2 - n_{eq}^2), \tag{1.32}$$

where

$$\langle\sigma v\rangle = \frac{1}{n_{eq}^2}\int d\Pi_A d\Pi_B d\Pi_{\chi_1} d\Pi_{\chi_2}(2\pi)^4\delta(p_A + p_B - p_{\chi_1} - p_{\chi_2})|\mathcal{M}|^2 f_{\chi_1}^{eq} f_{\chi_2}^{eq} \tag{1.33}$$

is the **thermally-average cross-section** and n_{eq} is the number density of particles in equilibrium. Due to the initial conditions, this does not corresponds to a well-defined energy and we have to integrate over to the possible energies that the particles in the thermal bath may have. Extra integrals in the phase space of incident particles with a given function distribution by $f_{\chi_1}^{eqq} f_{\chi_2}^{eqq}$ will appear. We are left with the familiar form of the Boltzmann equation,

$$\frac{dn}{dt} + 3Hn = -\langle\sigma v\rangle(n^2 - n_{eq}^2). \tag{1.34}$$

If the right side of the equation dominates, then n traces its equilibrium value $n \approx n_{eq}$. However, when $Hn > \langle\sigma v\rangle n^2$, then the right-hand-side can be neglected and the resulting differential equation $dn/n = -3da/a$ implies that $n \propto a^{-3}$. This means that the dark matter particles do not annihilate anymore and their number density decreases only because the scale factor of the Universe increases.

1.1.4 Thermal production of dark matter in the Universe

Particles that are in thermal equilibrium in the early Universe are called thermal relies. These particles would be decoupled from the primordial plasma at **freeze-out**[3], when the rate of annihilation of dark matter became smaller than the expansion rate of the Universe. After that, they will remains traveling in the Universe and depending of the can contribute to the total or partial average dark matter density. Particles produced by a non-thermal mechanism are known as non-thermal relics and are produced for example, gravitationally at the end of the inflation.

Freeze-out of relativistic species

Neutrinos are one example of relativistic particles and is important to consider their contribution to the total amount of dark matter. Since neutrino decouple while they are still relativistic, according to

[3]Dark matter abundance production can also be considered via freeze-in. After inflation, if the temperature of the Universe was not high enough for the dark matter particle to be in thermal equilibrium, the initial abundance of it will be zero. Interaction of particles in the thermal bath will be producing dark matter particles. The production rate is small, however, these particles do not annihilate or decay due to they are produced out of equilibrium, building a relic density.

equation 1.23 we have

$$Y_{eq} \approx 0.278 \frac{g_{eff}}{g_{*s}}. \tag{1.35}$$

Neutrinos decouple at a few MeV, when the species that were still relativistic are $e^{\pm}$, γ, ν and $\bar{\nu}$. The number of relativistic degrees of freedom is $g_* = g_{*s} = 10.75$. For one neutrino family, the effective number of degrees of freedom is $g_{eff} = 3g/4 = 3/2$. With these values we can calculate the relic density today

$$\begin{aligned} \Omega h^2 &= \frac{\sum_i m_{\nu_i} Y_\infty s_0 h^2}{\rho_c} \\ &\approx \frac{\sum_i m_{\nu_i}}{91\text{eV}}. \end{aligned} \tag{1.36}$$

Considering the current bound where $\sum_i m_{\nu_i} \approx 0.3eV$ we can quantify that the total contribution of neutrinos to the total amount of dark matter is $\Omega h^2 \leq 0.003$, that is less than the 3% of the total dark matter density.

Freeze-out of non-relativistic species

Boltzmann equation can be expressed as

$$\begin{aligned} \frac{dY}{dx} &= \frac{-sx\langle\sigma v\rangle}{H(m)}(Y^2 - Y_{eqq}^2) \\ &= \frac{-\lambda\langle\sigma v\rangle}{x^2}(Y^2 - Y_{eqq}^2). \end{aligned} \tag{1.37}$$

knowing as a Riccati equation. Here $\lambda = \approx 0.26(g_{*s}/g_*^{1/2})mM_P$. Now we can define the quantity $\Delta_Y = Y - Y_{eq}$ and a dimensionless variable $x = m/T$. To solve approximately Boltzmann equation, we can separate the solution in the early and late times.

For early times $1 < x << x_f$ where x_f is the freeze-out time, the yield follows closely its equilibrium value, $Y \approx Y_{eq}$ and we can assume $d\Delta Y/dx = 0$. We find

$$\Delta_Y = \frac{\frac{dY_{eq}}{dx}}{Y_{eq}} \frac{x^2}{2\lambda\langle\sigma v\rangle}. \tag{1.38}$$

At freeze-out using that for a large enough value of x and considering the non-relativistic yield at equilibrium, $\frac{dY_{eq}}{dx} \approx -Y_{eq}$ we have

$$\Delta_{Y_f} \approx \frac{x_f^2}{2\lambda\langle\sigma v\rangle}. \tag{1.39}$$

For late times $x >> x_f$, we can assume that $Y >> Y_{eq}$ and $\Delta_{T_\infty} \approx Y_\infty$. We have

$$\frac{d\Delta_Y}{dx} \approx -\frac{\lambda\langle\sigma v\rangle}{x^2}\Delta_Y^2. \tag{1.40}$$

We will integrate this equation from the the freeze-out time up to nowadays. Considering the value for which the equilibrium Yields has the right value when $x_f \approx 20$ we have

$$\Delta_{Y_\infty} = Y_\infty = \frac{x_f}{\lambda\left(a + \frac{b}{2x_f}\right)}. \tag{1.41}$$

where the thermally averaged annihilation cross section is expanded as $\langle\sigma v\rangle = a + \frac{b}{x}$. In terms of these results, the relic density can be expressed as

$$\begin{aligned} \Omega h^2 &= \frac{m_\chi Y_\infty s_0 h^2}{\rho_c} \\ &\approx \frac{10^{-10}[\text{GeV}]^{-2}}{a + \frac{b}{2x_f}} \\ &\approx \frac{3\times 10^{-27}\text{cm}^3\text{s}^{-1}}{a + \frac{b}{40}}. \end{aligned} \tag{1.42}$$

The expression shows that for larger values of the annihilation cross section, smaller values of the relic density are obtained. The evolution of this number will depends on both: the annihilation rate and the expansion rate. When the annihilation rate is much lower than the expansion rate $\Gamma << H$, the dark matter particles cannot find each other fast enough compared to the expansion rate and thus fall out of the equilibrium, $Y(x \leq xf) \approx Yeq(x)$ and $Y(x \neq x_f) \approx Yeq(x_f)$. Equation 1.42 can be analyze in some limiting cases to build intuition of how dark matter number density evolves with time.

1.2 Neutrino Physics

Considering the decays of heavy elements the following reaction is present, $A \rightarrow B + e^-$ where A and B are neutral and charged nucleus, respectively. When the distribution of beta particles were measured, the last result showed that there was a contradiction to the law of conservation of energy. In 1930 Wolfgang Pauli proposed an hypothesis trying to explain this, arguing that should be another particle involved in the last reaction in order to the equation be balanced. Considering a new particle called ***neutrino*** the correct energy distribution was obtained. In 1956, there was indirect evidence of this new neutral, spin 1/2 and light particle by Cowan and Reines experiment [32], where they measured the recoil of the nuclei that a particle emitted after absorbing an electron.

1.2.1 Neutrino mass problem

Nowadays, we know that neutrinos have mass, nevertheless in the Standard Model neutrinos remain massless. The non observation of right-handed neutrinos in the experiments keep them apart from the theory and there is not mass term generated for these particles. The mechanism of how neutrinos acquire mass is one of the actual open questions presents in physics keeping many physicist proposing and generating new models and ideas about it.

In 1957, Pontecorvo proposed that neutrinos could oscillate between flavors. In 1960 and 1062, a version about the idea of Pontecorvo explaining the oscillation mechanism was performed, including only two neutrino flavors [33, 34]. Supposing the idea that only two neutrino flavors exist, we have

$$\begin{aligned} |\nu_\alpha\rangle &= U_{\alpha j}|\nu_j\rangle \\ U_{\alpha j} &= \begin{pmatrix} \cos\theta & \sin\theta \\ -\sin\theta & \cos\theta \end{pmatrix} \end{aligned} \tag{1.43}$$

where the index α and j labels the neutrino mass eigenvalue basis and the electroweak basis, respectively. if we label the mass eigenvalues as m_1 and m_2, the probability of oscillation from the flavor i to j with $i \neq j$, can be written as

$$P_{i\to j} = \sin^2(2\theta)\sin^2\left(\frac{\Delta \mathrm{m}^2 \mathrm{L}}{4\mathrm{E}}\right). \tag{1.44}$$

Here E is the energy of the neutrino in the experiment and L is the distance traveled by the neutrino. According to equation 1.44, the probability of converting one neutrino flavor into another is because there are not more than one neutrino massless and the square mass difference Δm^2 is different than zero. Considering three neutrino flavors, equation 1.44 get more complicated but the idea remains, also taking into account that the probability will depends on the mixing angle between the different neutrino flavors.

One of the neutrino oscillation parameters is the squared mass difference for neutrinos, which is defined as $m_i^2 - m_j^2$. Here i and j are labeling different mass eigenvalues for neutrinos. We can define these masses as m_1, m_2 and m_3. Up to now, there are not precise values for each neutrino mass nor an idea of the corresponding ordering which can be defined as normal or inverted hierarchy of neutrino masses. Normal ordering assumes that neutrino masses increase ordering by the values of m_1, m_2 and m_3. Inverted ordering assumes the decreasing ordering m_2, m_1 and m_3. The squared mass differences will control the frequency of the flavor oscillation in the weak basis.
The most general parametrization of the neutrino mixing matrix includes three rotations. When CP violation is allowed, also three unitary phases are added. The following unitary matrix, known as the

Pontecorvo-Maki-Nakagawa-Sakata matrix (PMNS)

$$
\begin{aligned}
|\nu_\alpha\rangle &= U_{\alpha j}|\nu_j\rangle \\
U_{\alpha j} &= \begin{pmatrix} 1 & 0 & 0 \\ 0 & \cos\theta_{23} & \sin\theta_{23} \\ 0 & -\sin\theta_{23} & \cos\theta_{23} \end{pmatrix} \times \begin{pmatrix} \cos\theta_{13} & 0 & \sin\theta_{13}\mathrm{e}^{-\mathrm{i}\delta} \\ 0 & 1 & 0 \\ -\sin\theta_{13}\mathrm{e}^{-\mathrm{i}\delta} & 0 & \cos\theta_{13} \end{pmatrix} \\
&\times \begin{pmatrix} \cos\theta_{12} & \sin\theta_{12} & 0 \\ -\sin\theta_{12} & \cos\theta_{12} & 0 \\ 0 & 0 & 1 \end{pmatrix} \times \begin{pmatrix} e^{i\alpha_1/2} & 0 & 0 \\ 0 & e^{i\alpha_2/2} & 0 \\ 0 & 0 & 1 \end{pmatrix}
\end{aligned} \tag{1.45}
$$

represents the rotation matrix for a system of three neutrino flavor, where δ (for Dirac neutrinos) and $\alpha_{1,2}$ (for majorana neutrinos) are the CP violation phases.

1.2.2 Neutrino mass generation

There are two possibilities for neutrino masses that have been studied extensively. Neutrinos can get a Dirac mass term or a Majorana mass term [35, 36]. For the charged fermions, only Dirac mass terms are allowed due to conservation of electric charge. In this thesis we have considered that neutrinos are Majorana, nevertheless we will give a brief explanation of both scenarios [37].

Dirac masses

In the case of a Dirac mass term, a Dirac neutrino by a four component Dirac spinor ν will be written as

$$
\nu = \begin{pmatrix} \chi \\ \sigma_2\phi^* \end{pmatrix} \tag{1.46}
$$

where σ_2 is a Pauli matrix and χ and ϕ are the two-component Weyl spinors. Neutrinos can be defined as:

$$
\nu_L = P_L\nu \tag{1.47}
$$

$$
\nu_R = P_R\nu, \tag{1.48}
$$

as left-handed and right-handed neutrinos, respectively according to their chirality properties. Here $P_{L,R} = \frac{1}{2}(1 \mp \gamma_5)$ are the chirality projectors. Hence, in terms of Dirac spinors we have:

$$
\nu_L = \begin{pmatrix} \chi \\ 0 \end{pmatrix} \tag{1.49}
$$

$$
\nu_R = \begin{pmatrix} 0 \\ \sigma_2\phi^* \end{pmatrix}. \tag{1.50}
$$

Applying the charge conjugation to the field defined in (1.46) we obtain:

$$\begin{aligned} \nu^c = C\bar{\nu}^T &= -\gamma^2\gamma^0\bar{\nu}^T \\ &= \begin{pmatrix} \phi \\ \sigma_2\chi^* \end{pmatrix} \end{aligned} \tag{1.51}$$

where the Weyl spinors χ and ϕ get exchanged because for Dirac neutrinos the antineutrino does not coincide with the neutrino (as it happens for Majorana neutrinos), i.e. $\nu \neq \nu^c$.
The Lagrangian mass term for Dirac neutrino masses can be defined as

$$\mathcal{L}_D = -m_\nu^D \bar{\nu}_L \nu_R + h.c. \tag{1.52}$$

Considering that three families of singlet right-handed neutrinos ν_R, all of them under the Standard Model gauge group, with their respective Yukawa coupling are added to the particle content of the Standard Model. The mass term $m_\nu^D = Y_\nu \langle v \rangle$ where $\langle v \rangle \sim 100$ [GeV] is the expectation value for the Higgs boson, would come from the Lagrangian term after electroweak symmetry breaking as:

$$\mathcal{L}_Y = -Y_\nu \langle v \rangle L \nu_R, \tag{1.53}$$

where Y_ν is a 3×3 matrix. Considering that neutrino masses are the order below $\sim$ eV, the value for Y_ν must be below 10^{-11}, saying that right-handed neutrinos couple very weakly to the rest of matter. Right-handed neutrinos are not included in the Standard Model spectrum since experiments related with weak interaction have not detected them.

Majorana masses

The Dirac Lagrangian for any free fermion field which can be either charged or not is

$$\mathcal{L}_\mathcal{D} = \frac{1}{2}\bar{\nu}(i\not{\partial} - m)\nu, \tag{1.54}$$

where $\nu = (\nu_L \quad \nu_R)^T$. The mass term can be written in terms of the chiral bispinors. Using the definition of the adjoint spinor we have

$$\mathcal{L}_{(\mathcal{D})} = -m_D \nu\bar{\nu} + ... = -m_D(\bar{\nu_L}\nu_R + \bar{\nu_R}\nu_L) + ... \tag{1.55}$$

As it was described when we presented the Dirac scenario for neutrino masses, the Lagrangian above is the one that will be introduced when right-handed neutrinos acquire a Dirac mass term. If the fermion is neutral, a relation between the bispinors ν_L and ν_R can be established and yields into

$$\begin{aligned} \bar{\nu} &= (\bar{\nu_L} \quad \nu_L^c)^\dagger \gamma_0 \\ &= (\bar{\nu_L^c} \quad \bar{\nu_L}). \end{aligned} \tag{1.56}$$

Thus, the mass term in the Dirac Lagrangian will be

$$\begin{aligned}\mathcal{L}_{(D)} &= -\frac{m}{2}\bar{\nu}\nu + ... \\ &= -\frac{m}{2}\left(\bar{\nu_R}^c\nu_L + \bar{\nu_L}\nu_R^c + h.c. \right). \end{aligned} \tag{1.57}$$

Neutral fermions with left and right components relate with $\nu_L = \nu_R^c$ are known as Majorana spinors [38]. The Majorana mass term annihilates a **left-handed neutrino** and creates a **right-handed antineutrino**, which means that it changes a particle to an antiparticle. It can be shown that a Majorana particle with a twin brother of equal mass will describe a Dirac fermion [39]. This is the reason why Majorana mass term violates lepton number by two units. As we have notice in the Lagrangian, Majorana mass term are forbidden for charged fermions such as the electron, due to they have non zero electric charge and $U(1)$ must be invariant.

There are phenomenological implications to the nature of neutrinos. One of these is related with neutrinoless double beta decay [40] that it is only possible if neutrinos are Majorana. This phenomenon will be explained later due to the implications that will have to this work.
We will continue our discussion first, listing the mechanisms to give masses to neutrinos. One of the most popular is known as the ***seesaw* mechanism** [39, 41, 42, 43, 44] which can be realized in many possible ways. Here, we will considered only the ones that are the most important to this work.

Weinberg Operator

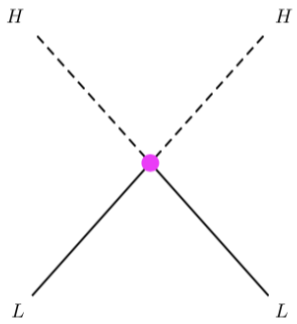

Figure 1.1: Weinberg operator. Majorana mass terms give rise when the electroweak symmetry is broken. The dot in the center represent the new physics that can be introduced at high scales of energy.

Above energies given by a cut off scale Λ, new physics might appear. The new physics can be explained by effective operators which are non-renormalizable operators (NRO) that summarizes essential ingredients of a model. We can assume that there is new physics at a high scale Λ and it will manifest itself by some non-renormalizable operator suppressed at energies much lower than Λ, $E << \Lambda$, by powers of E/Λ. In 1979 Weinberg postulated a theory to extend the Standard Model and give masses to neutrinos [45]. With

a non-renormalizable interaction between the Higgs field and neutrinos, a Majorana mass term can be generated. Let's assume that the form of the Weinberg operator is:

$$\mathcal{O}_W = \frac{1}{\Lambda} L_i L_j \phi\phi \tag{1.58}$$

where L_i and L_j are lepton doublets and ϕ is the Standard Model Higgs doublet field. After the electroweak symmetry breaking, through the nonzero vacuum expectation value (vev) of the Higgs ($v = 246.22$ [GeV]), Weinberg operator will generate a Majorana mass term for neutrinos,

$$\mathcal{O}_W = \frac{1}{\Lambda} \nu_i \nu_j \langle\phi^0\rangle\langle\phi^0\rangle \tag{1.59}$$

where $\langle\phi^0\rangle = \frac{v}{\sqrt{2}}$ and thus will leads the dependence $m_\nu \propto \frac{\langle v\rangle^2}{\Lambda}$. The last dependence is in contrast with the other fermions whose masses are linear to the vev. Due to Λ is the energy scale where the Weinberg operator is generated (see figure (1.1)), it can have a high value. This idea can explain the small value of neutrinos masses, which will be suppressed by Λ.
There are many different models whose at low scales of energy give rise to the Weinberg operator. At tree level, there are three posible realizations of the Weinberg operator:

- Type I seesaw [43, 46]
- Type II seesaw [41, 44, 47]
- Type III seesaw [48]

The Feynman diagrams for the different types of seesaw mechanism are shown in figure (1.2)

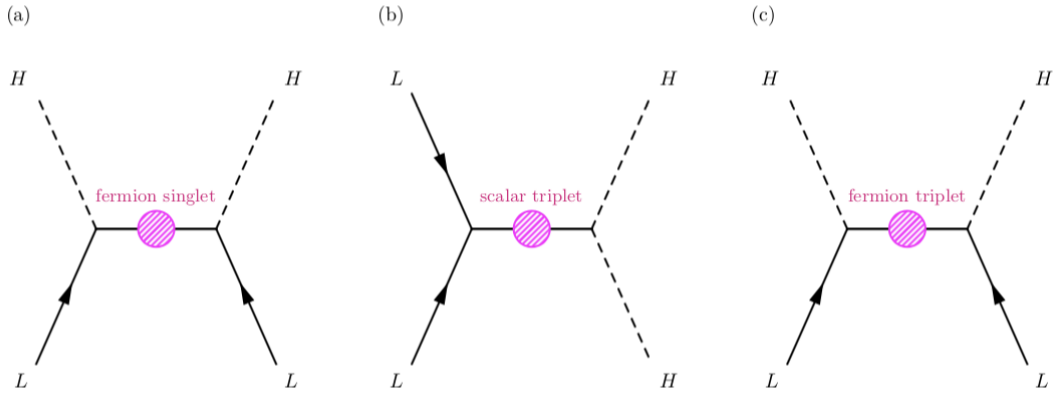

Figure 1.2: Feynman diagrams for different seesaw mechanism types: (a) seesaw type I, (b) seesaw type II, (c) seesaw type III..

Type I Seesaw mechanism

Considering that neutrino masses are Majorana masses they will be given by $m_{LL}\bar{\nu_L}\nu_L^c$ where $\bar{\nu_L}$ is a left-handed neutrino field and ν_c^c is a right-handed antineutrino field [4]. Neutrino Majorana masses violate lepton number conservation and assuming only Higgs doublet fields are present in the Standard Model, these are forbidden at the renormalisable level by gauge invariance. The type I seesaw mechanism assumes that these terms are generated effectively when right handed neutrinos are introduced, but are zero at the beginning. If Y_{ν_R} is the coupling $\phi L \nu_R$, we can write the mass term in the Lagrangian as

$$\mathcal{L}_\nu = -\frac{1}{2}\begin{pmatrix} \bar{\nu_L} & \bar{\nu_L}^c \end{pmatrix} \mathcal{M} \begin{pmatrix} {\nu_R}^c \\ \nu_R \end{pmatrix} + h.c. \tag{1.60}$$

where

$$\mathcal{M} = \begin{pmatrix} 0 & m_D \\ m_D^T & M_R \end{pmatrix} \tag{1.61}$$

is the mass matrix for the neutrino, where both Dirac mass term m_D and Majorana mass term M_R are included. if we assume that $M_R >> m_D$, the mass matrix $\mathcal{M}$ can be diagonalized and give rise to three light eigenstates and three heavy eigenstates,

$$m_\nu^{\text{light}} = -m_D^T \cdot M_R^{-1} \cdot m_D = \frac{Y_{\nu_R}^2 v^2}{2M_R}, \tag{1.62}$$

$$M^{\text{heavy}} = M_R. \tag{1.63}$$

In this case we will have *pure Majorana neutrinos* with mass $m_\nu = Y_{\nu_R} v$. On the other hand, when $M_R = 0$ the mass matrix will give three *pure Dirac neutrinos*. In that case, lepton number conservation is restored and to get the correct value of neutrino masses the Yukawa coupling will be much smaller (of order $\sim 10^{-12}$) than the other Yukawa coupling of the Standard Model. Also, pseudo Dirac neutrinos will be present if $M_{\nu_R} << Y_{\nu_R} v$.

Type II seesaw mechanism

In this case of seesaw a scalar triplet, Δ with hypercharge 1 and under the $SU(2)_L$ is added. We can add one Higgs-like triplet field Δ, composed by three components with charge $0, +1, +2$. The Lagrangian mass term becomes

$$\mathcal{L} = -M_\Delta^2 |\Delta|^2 - \lambda_\Delta L \Delta L - \mu_1 \phi \Delta \phi + h.c. \tag{1.64}$$

Integrating out, the heavy triplets generates the Majorana mass operator $(LH)^2$ as in the previous case. As similar as in the case of the seesaw type I, the presence of the last two terms will breaks the lepton number by two units. After the electroweak symmetry breaking when the Higgs field gets a vev, considering

[4] Due to Majorana masses are forbidden by electric charge violation, the interaction is possible due to both the neutrino and antineutrino are electrically neutral.

$M_\Delta >> v$ we have that the mass for the light Standard Model neutrino is

$$m_\nu = \frac{\lambda_\Delta \mu_1 v^2}{2M_\Delta^2}. \tag{1.65}$$

As we can see, the lightness of Standard Model neutrino masses at low energies is explained by the heavy masses of another field. In this case is the triplet Δ.

Type III seesaw mechanism

Lepton fields and the Higgs doublet field ϕ will combine to form a fermion triplet. The intermediary particle must be a fermion triplet Σ as well, which is added to the Standard Model and is a $SU(2)_L$ triplet with zero hypercharge. The Lagrangian mass term will be

$$\mathcal{L}^{\text{mass}} = -\frac{M_\Sigma}{2}\Sigma\Sigma - \lambda_\Sigma \Sigma L H + h.c. \tag{1.66}$$

The mass for the left-handed neutrino will be

$$m_\nu = \frac{\lambda_\Sigma^2 v^2}{2M_\Sigma} \tag{1.67}$$

which looks similar to the case of the type I seesaw.

1.3 Dark Matter

In this thesis we are considering dark matter as a **weakly interactive particle** (WIMP). In the next section we present the main astronomical evidences of dark matter and we give a brief description about the different dark matter candidates that exist. Also, we present the experimental searches to a WIMP-like dark matter particle: direct searches, indirect searches and collider searches.

1.3.1 Dark matter motivations

Astrophysical evidence of dark matter is based on gravitational effects that cannot be explained by just the observed baryonic matter. For example, these gravitational effects can be perceived through the observation of the deflections of light by gravitational lensing or dynamical effects. One of the ways to address these problems is the inclusion of more matter that does not emit any light. Another scenario to solve the problem is related to the modification of Newtonian equations. Nevertheless, with this last solution the problem is solved only at galactic scales, also leaving problems as reproducing the anisotropies of the CMB without a solution or explanation.
The elementary particles that compose the actual Standard Model are not candidates to be a sub-dominant dark matter particle, giving us one reason to extend this model. In order to understand the motivations

of a dark matter particle, we present the astrophysical and cosmological evidence that indicates that at least the $\sim 27\%$ of the Universe mass density is dark.

Galactic scale

From standard Newtonian gravity we find the relation

$$v = \sqrt{\frac{GM(r)}{r}}, \tag{1.68}$$

where v is the rotation velocity of the objects in the galaxy and $M(r)$ the mass contained within the radio r. Gauss Law says that the mass M should remains constant assuming that all the mass is concentrated in the bulge and $v \propto r^{-1/2}$. Observations of rotation curves of spiral galaxies by Vera Rubin et al. [49, 1] showed that the circular velocity curve flattens out at large radial distances as we can see in figure (1.3). Already observations imply $M(r) \propto r$. If a new mass component that satisfy this relation is included the flatness of rotation curves can be obtained[5]. Because of that, it is necessary an additional component of matter of non-interacting particles.

According to rotation curves, we can infer that dark matter mass density distribution is

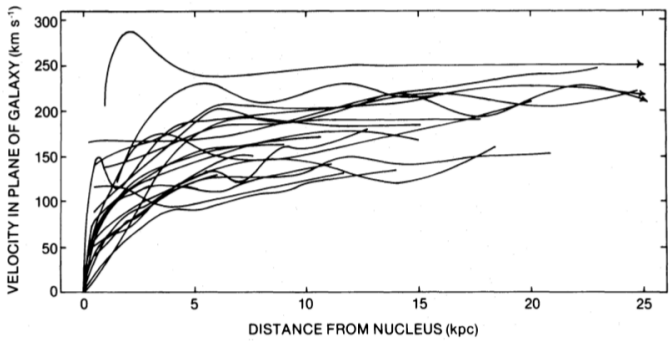

Figure 1.3: 21 Sc rotation curves measured by Vera Rubin et al. [1].

$$\rho(r) \sim \frac{1}{r^2}. \tag{1.69}$$

This halo of dark matter can extend up to ten times the size of the galactic disk and contains approximately an 80% of the total mass of the galaxy.

Galaxy clusters

Dynamical systems. One of the arguments in favor of dark matter and in contradiction to MOND

[5]Some works by Bosma [50] and van Alba et al [51]. showed that this flatness could not be reproduced by modifying the relative weight of the diverse galactic components.

(Modified Newtonian Dynamics) theories is the Bullet Cluster (1E 0657-558) [2]. It consist of two clusters of galaxies that collide. The visible component of the cluster display a characteristic shock wave. Weak-lensing analyses using data took it by the Hubble Space Telescope have revealed that most of the mass of the system is displaced from the visible components. The conclusion is that the dark matter components of the cluster do not interact significantly. In the case of MOND theories, we would expect that the lensing occur due to the baryonic matter, i.e. in the center where the mass interact not in two separated areas as is shown in figure (1.4).

Dark matter filaments structure. Observations of luminous matter distribution have shown that it

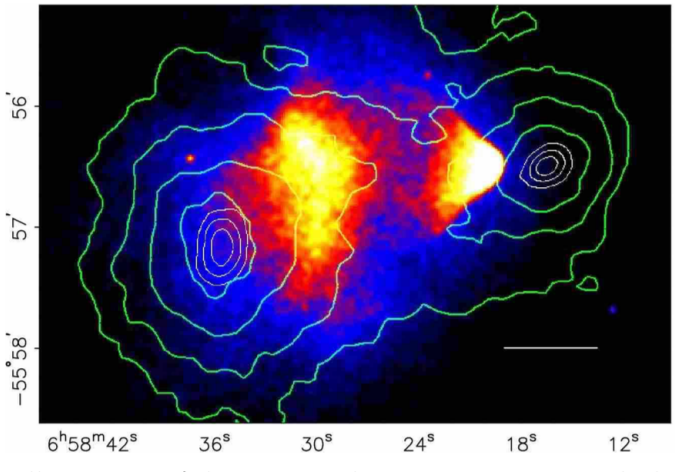

Figure 1.4: 500 ks Chandra image of the Bullet cluster. Green contour shown the weak lensing κ (the surface mass density of the lens divided by a scaling constant) reconstruction with the outer contour level at $\kappa = 0.16$ [2].

follows a filamentary structure at large scale. This feature can be reproduced with numerical simulations of cold dark matter, which plays an important role in the creation of this filamentary structure, trapping the luminous matter via gravity interaction. Figure (1.5) shows the existence of a possible dark matter filament joining the two clusters of the Abell 222/223 supercluster [3].

Motion of galaxy clusters. Assuming that the Coma galaxy cluster is an isolated system, Fritz Zwicky studied the motion of galaxies on it [52]. A relation between the average velocity of objects with the gravitational potential can be established using the virial theorem. The results show that the ratio of mass to light was much larger than the one expected in comparison with other systems [53]. An explanation could be related with a large amount of missing mass which can be attributed to dark matter.

Cosmological scale

The determination of the cosmological parameters of the Universe comes from the analysis of the

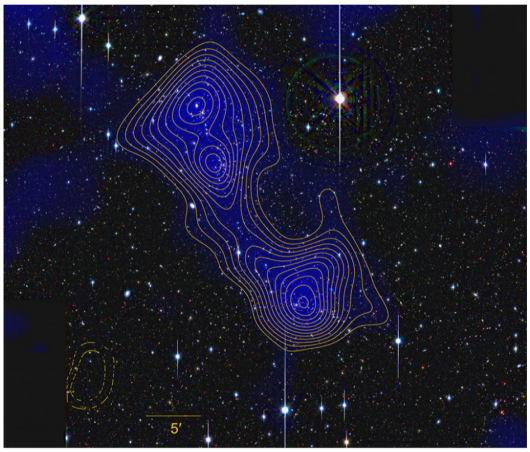

Figure 1.5: Dark filamentary structure in the system Abell 222/223 [3]. The image was reconstructed using weak lensing technics.

Cosmic Microwave Background (CMB) fluctuations made by WMAP [54] and Planck satellites and the Atacama Cosmology Telescope (ACT) [55]. The data obtained by satellites as the COsmic Background Explorer (COBE) [56] confirm that we live in a flat Universe, dominated by dark matter and dark energy. The cosmological abundance of dark matter have been determinated by Planck satellite [20]

$$\Omega_\chi h^2 = 0.1196 \pm 0.0031. \tag{1.70}$$

We can infer that dark matter is responsible of the 26% of the Universe energy density while 69% is by dark energy.

1.4 Dark matter candidates and searches

One of the main questions about dark matter is what it is made off. Many evidence have shown that dark matter is a kind of particle that is

- **non-baryonic**. Recent analysis of the CMB [20] gives information about the values for the cosmological density of baryons $\Omega_b h^2 = 0.02242 \pm 0.00014$, dark matter $\Omega_\chi h^2 = 0.11933 \pm 0.00091$, matter $\Omega_m h^2 = 0.3111 \pm 0.00056$ and dark energy $\Omega_\Lambda h^2 = 0.6889 \pm 0.00056$. The discrepancy between Ω_b and Ω_m insinuates that non-baryonic matter (dark matter) will dominate energy and mass density.
- **neutral**. If dark matter was not neutral, it would scatter light and it would not be dark.
- **non-relativistic**. Relativistic dark matter (hot dark matter) has inconsistencies with observations.
- **very long-lived**. If dark matter is not stable, should be a long-lived particle. We know that stable candidates for dark matter are common in models where an extra symmetry is imposed ensuring the stability of the lightest particle. Nevertheless, dark matter can be long-lived and decay whenever

their lifetime is longer than the age of the Universe. This kind of dark matter, as the gravitino, feature small couplings.

- **collisionless** (or not very collisional). A dark matter particle must be very weakly interacting with baryonic particles. Dark matter self-interactions are not ruled out, but upper limits on $\sigma_{\chi\chi}/m_\chi$ are computed to be $\leq 0.3\text{cm}^2/\text{g}$ [57] coming from observations of the surfaces densities of dark matter halos and $\leq 0.7 - 1.3\text{cm}^2/\text{g}$ [58] from observations of the Bullet Cluster.

One of the main candidates proposed in literature in the past are the Standard Model neutrinos. Neutrinos are particles of the Standard Model that have a very small mass. We know that they are very abundant in the Universe and interact very feebly, through the electroweak force, with ordinary matter. At the beginning, scientist believed that neutrinos was the total dark matter of the Universe but many arguments show that they only contribute to a very small part of it. Neutrino's thermal relic abundance can be computed through the study of the neutrino decoupling in the early Universe. When they decoupled, they are relativistic particles yielding

$$\Omega_\nu h^2 \propto \frac{\Sigma_i m_i}{91\text{eV}}. \tag{1.71}$$

Using the current upper bounds of neutrino mass difference [59], we get that $\Omega_\nu h^2 < 0.003$ that is only a small part of the total relic abundance measured by Planck. Also, neutrinos are considered hot dark matter (relativistic) and leads to a different hierarchy of structure formation inconsistent with observations.

As we mentioned before, in this work we focus on a WIMP dark matter candidate. Other kind of dark matter candidates to study are:

- Sterile neutrinos [60].
- Axions or axion-like particles [61]
- Supersymmetry candidates [62]
- Ultra-light dark matter [63].
- WIMPzillas [64].
- Primordial black holes [65].

The parameter space of these possible dark matter candidates and others is described in figure (1.6).

1.4.1 A dark matter particle

WIMPs are considered a good dark matter candidate because they are massive particles that are feeble interacting and long-lived providing a non-relativistic cold candidate that is compatible with cosmology. This particle interacts via weak force and its range of mass can arises until the TeV scale. This kind of particles can be bosons and fermions and are proposed as many candidates coming from extensions of the Standard Model. Different classes of WIMPs have been studied [66, 67]: one of them corresponds to the extension of the Standard Model Higgs sector, adding an extra Higgs doublet; another case is the

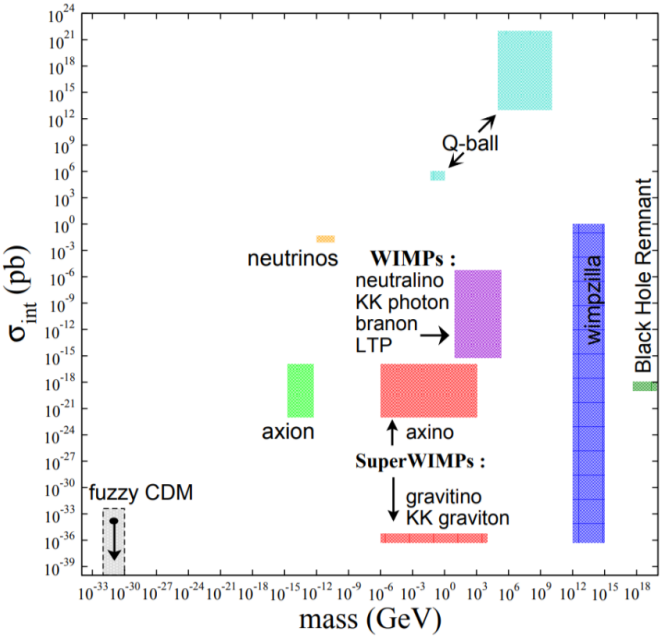

Figure 1.6: Interaction cross section versus the mass of different dark matter candidates. Figure from [4].

supersymmetric extension of the Standard Model.

Proposing a WIMP as a dark matter candidate, implies that is necessary a mechanism of its production in the early Universe, that be able to explain the current observed dark matter abundance in the Universe. The freeze-out scenario is the most common mechanism for WIMPs dark matter generation. If WIMPs interactions are enough efficient, the annihilation rate exceeds the Hubble expansion rate and the WIMP dark matter is in thermal equilibrium with the primordial thermal bath. When temperature drops below the dark matter mass, the yield Y_χ becomes Boltzmann suppressed, i.e. Y_χ is approximately constant with time. The WIMP number density decrease while the Universe expands and cools down. When they cannot self-annihilate anymore nor can they be created by the inverse process, WIMPs would decoupled from the primordial plasma at freeze-out temperature. Figure 1.7 shown that the dark matter abundance is inversely proportional to the thermally-average cross-section of dark matter $\langle \sigma v \rangle$. By solving the Boltzmann equation we can notice that, in order to get the correct experimental value for the dark matter relic density $\Omega_\chi h^2 \approx 0.12$, the value of the thermally-average cross-section is $\langle \sigma v \rangle \sim 10^{-26}$ cm^{3}s^{-1} for a WIMP dark matter mass around the 100 [GeV] to the 10 [TeV]. The masses close to the weak scale that reproduce the correct dark matter abundance of the Universe call this as the *"WIMP miracle"*.
In order to detect a possible WIMP dark matter three scenarios, illustrated in figure (1.8) of dark matter detection have been studied: direct detection, indirect detection and collider searches.

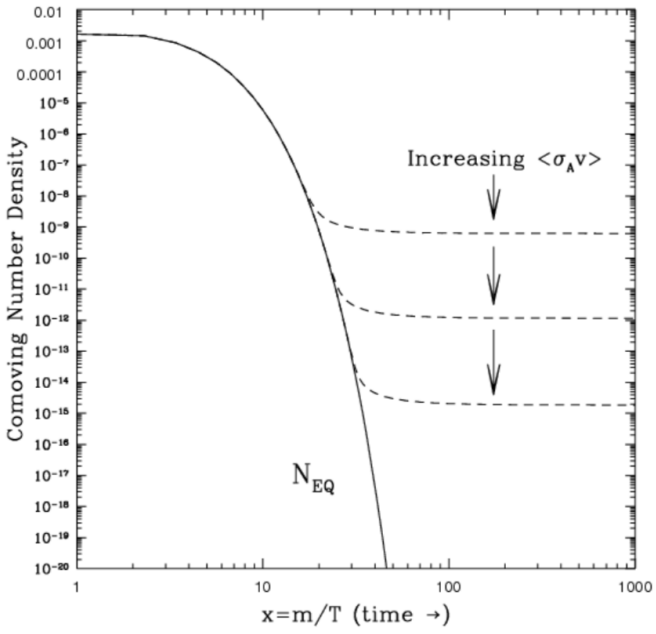

Figure 1.7: Dark matter number density versus $x = m/T$. The number density of dark matter particles drops until the freeze out moment when the dark matter would decoupled and its abundance remains stable. Higher dark matter abundance values are gotten when $\langle\sigma v\rangle$ decrease. Figure form [5].

1.4.2 Direct searches

The idea of direct searches is measuring the recoil of a nuclei after scattering with a WIMP like dark matter particle in underground detectors. The mean velocity of WIMPs presumed is similar to that of galactic objects, i.e. $10^{-3}c$ so it expects the recoil kinetic energy to be about tens or hundreds of keV. For this process we can choose the optimal nuclear target.

The direct detection rate of a WIMP χ depends on many parameters: the mass of the WIMP-like dark matter m_χ and its cross section on the target nuclei $\sigma_\chi N$, the local halo density ρ_0 and the velocity distribution of WIMPs around the galaxy $f(v)$. This differential rate is given by

$$\frac{dR}{dE_R} = \frac{\rho_0}{m_N m_\chi} \int_{v_{\min}}^{\infty} v f(v) \frac{d\sigma_\chi N}{dE_R}(v, E_R) dv, \tag{1.72}$$

where m_N the mass of the nucleus, $v_{\min} = \sqrt{(m_N E_R)/2\mu_N^2}$ is the minimum velocity of the WIMP which can cause a recoil of energy E_R and $\frac{d\sigma_\chi N}{dE_R}(v, E_R)$ is the differential cross section for the WIMP-nucleus elastic scattering [68]. The differential event rate is typically expressed in therms of count/kg/day/keV. The elastic scattering occurs in the extreme non-relativistic limit since the WIMP-nucleon relative speed is ~ 100 km^{-1}s^{-1}. We calculate the recoil energy of the nucleon in terms of the scattering angle θ^* on the frame of the center of mass

$$E_R = \frac{\mu_N^2 v^2 (1 - \cos\theta^*)}{m_N}, \tag{1.73}$$

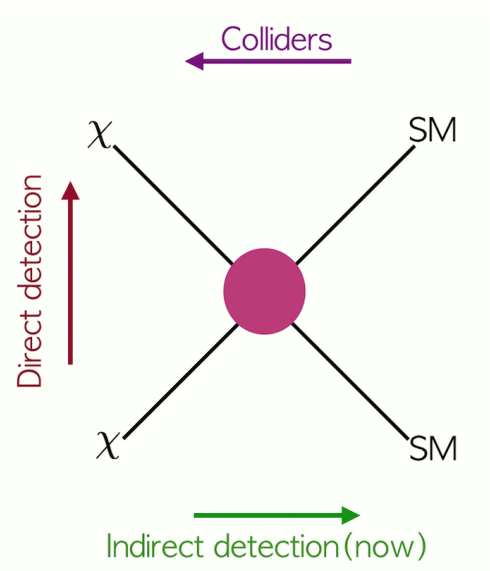

Figure 1.8: Scheme of different types of searches for a WIMP-like dark matter which is valid only in absence of resonances and coannihilations. The term "now" in indirect searches indicates that the dark matter annihilation is at present and do not in the early times of the Universe. The figure depicts the interaction between a WIMP χ and SM particles. Cross section for thermal production in the early Universe, for indirect detection and direct detection are related to each other [5]. In the case of collider searches, the production of new particles which have been interpreted as dark matter particles, is shown.

where $\mu_N = m_\chi m_N/(m_\chi + m_N)$ is the WIMP-nucleon reduced mass.
The total event rate is found by integrating the differential event rate over all the possible recoil energies:

$$R = \int_{E_T}^{\infty} dE_R \frac{\rho_0}{m_N m_\chi} \int_{v_{\min}}^{\infty} v f(v) \frac{d\sigma_{\chi N}}{dE_R}(v, E_R) dv, \tag{1.74}$$

where E_T is the smallest recoil energy that the detector is capable of measuring. The WIMP-nucleus differential cross section depends fundamentally on the WIMP-quark interaction strength, calculated from the microscopic description of the model, in terms of an effective Lagrangian describing the interaction of quarks and gluons with WIMP-like dark matter candidate. The WIMP-nucleus cross section is then obtained through the use of the hadronic matrix elements which also can be separated in two contributions, one spin-independent and other spin-dependent,

$$\frac{d\sigma_{\chi N}}{dE_R} = \left(\frac{d\sigma_{\chi N}}{dE_R}\right)_{SI} + \left(\frac{d\sigma_{\chi N}}{dE_R}\right)_{SD}. \tag{1.75}$$

Finally, the total cross section between the WIMP and nucleus is calculated by adding the above spin-dependent and spin-independent components, using the nuclear waves functions. There will exists a form factor $F(E_R)$ encoding the dependence of the momentum transfer $q = \sqrt{2m_N E_R}$, and accounts for the coherence loss which leads to a suppression in the event rate for heavy nucleons of heavy WIMPs. The

differential cross section can be expressed as

$$\frac{d\sigma_{\chi N}}{dE_R} = \frac{m_N}{2\mu_N^2 v^2}(\sigma_0^{\rm SI} F_{\rm SI}^2(E_R) + \sigma_0^{\rm SD} F_{\rm SD}^2(E_R)), \tag{1.76}$$

where the cross section at zero momentum transfer have been separated in a spin-independent contribution $\sigma_0^{\rm SI}$ and a spin dependent contribution $\sigma_0^{\rm SD}$.
Analysing the Lagrangian that describes the interaction of the WIMP with the quarks, we can see the origin of the different contributions. The contribution to the spin-dependent part of the cross section arises from the axial-vector couplings while the contribution to the part of spin-independent cross section comes from the scalar and vector couplings. In this work, since we are considering a WIMP scalar dark matter candidate, the contribution for the dark matter-nucleus differential cross section will be spin independent.

For WIMP signals, the **annual modulation** of the recoil rate due to the Earth speed variation is an experimental signature expected in direct detection experiments. Dark matter has not preference to any direction of motion with respect to the Galactic rest frame. If we are in the laboratory rest frame, dark matter velocities will be oriented in the opposite direction to the motion of the Sun and there will be a wind of dark matter in the solar rest frame (figure (1.9)). Since the Earth moves around the Sun, during June the Earth will pass towards this wind and an observer will see more high velocity particles. As a result, the dark matter flux is larger in the summer compared to the winter (for the northern hemisphere).

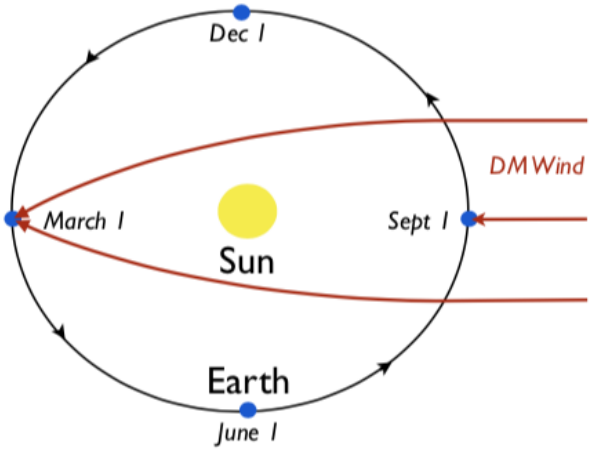

Figure 1.9: Schematic representation of the orbit of the Earth around the Sun with a relative orientation of the incident wind of dark matter (figure from [6])).

What determines the sensitivity of the experiment to a WIMP signal is illustrated in figure (1.10).

We have three important contributions:

- Energy threshold: We notice that, for a given recoil energy E_R, we require a minimal velocity of the WIMPs dark matter. Experiments are sensitive to dark matter interactions above a certain energy threshold and we only can prove part of the WIMP velocity distribution function, depending on the dark matter mass. Since the dark matter particles in the halo have a maximum velocity, the threshold is a limitation to explore dark matter with low mass
- Target: Among many other parameters, the WIMP recoil rate depends on two factors: the total mass of the detector and the nuclear composition of the detector target. A target will have implications on the experimental sensitivity to light and heavy WIMPs. As a target material, direct detection experiments usually make use of either Xe (xenon), Ge (germanium), Si (silicon), Na (sodium), I (iodine) or Ar (argon).
- Background and exposure: it will determine the total sensitivity of the experiment trying to exclude the background of similar signals to dark matter, pushing the limits to lower scattering cross section.

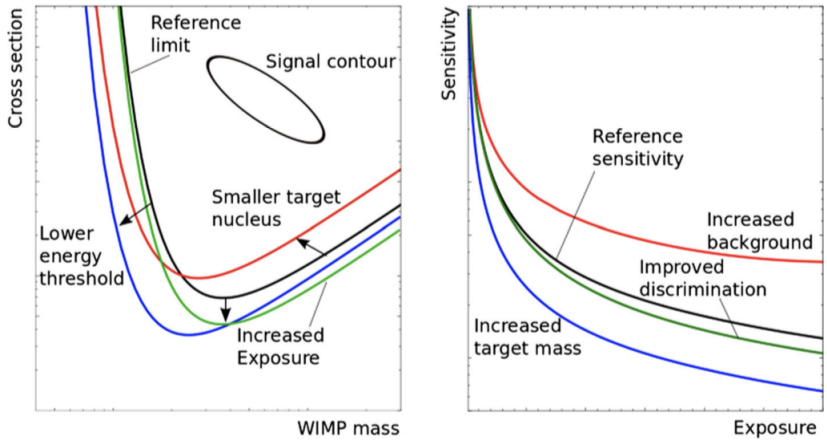

Figure 1.10: Illustration of a dark matter direct detection cross section versus the WIMP mass. Left: We can see in the solid blue and black curves that for low WIMP masses the energy threshold will determine the smallest mass of a WIMP accessible to a given direct detection experiment. Here the black line is the limit and signal for reference and the blue line refers to a direct detection experiment with lower energy threshold (colored lines are illustrating the variation of an upper limit due to changes in the detector). With larger exposure, stronger bounds of the scattering cross section are gotten (green solid line). Right: Background and exposure impact on the sensitivity. Black curve is a reference curve. Red and green curves show the impact when the background is discriminated [7].

Until today, direct detection dark matter experiments have improved considerably, especially in the low-mass range, but dark matter has not been detected yet. The goal for direct detection experiments is to shield the radioactive background. Since the event rate of dark matter particles is much smaller than the flux of cosmic rays, they are installed underground to block cosmic muons which will produce neutrons simulating WIMP signals. Other background sources must be analize as those produced by gamma rays and neutrinos [7].

There are many competing experiments trying to detect dark matter with either light or high masses. CRESST [69, 70], CDMS [71, 72, 73, 74] and SuperCDMS [75, 76, 77] are cryogenic detectors operating at low temperatures ($\lesssim$Mk). There are experiments using noble liquid gas: LUX [78], XENON [79, 80, 81, 82, 83], PandaX-II [84, 85] and Zeplin-III [86] uses Xe, while DarkSide [87, 88, 89], ArDM [90, 91], and WArP [92] are experiments based on Ar as the noble gas that scintillates from particle interaction. Experiments as PICO [93, 94, 95], that was formed from the merges of PICASSO and COUPP experiments, are searching for galactic dark matter using bubble chambers.
Since our work is focusing in one in particular dark matter mass range, we present a discussion only about XENON1T experiment and DAMA [96, 97, 98, 99], that have reported possible detection signals of dark matter. Other experiments as CDMS-II, CoGeNT [100, 101] and CRESST also report a possible WIMP-like dark matter detection or some anomalies in the data.

XENON: The experiment started in 2005 at Gran Sasso underground laboratory in Italy. As the target, the recoil energy that Xenon can achieve is in the order of a few hundred [GeV]. In 2006 the XENON experiments started with XENON10 [81] where limits of WIMP-nucleon cross sections were set around 10^{-43}cm^{-2} for a WIMP mass of 30 [GeV]. The detector was updated to XENON100 in 2008 with no success in the observation of a dark matter signal above the expected background. Presently, XENON1T [102, 103] is operative, whose fiducial volume contains 1.3 tonnes of liquid xenon. The project is being improved to XENONnT [12] that utilizes a total of 8.3 tonnes of xenon with a fiducial volume of 4 tonnes.
This dual-phase noble liquid detector works through the scintillation and ionization produced by the particle interactions inside this noble gas, which is not absorbed by the medium and is extracted from large volumes of detector material. The interaction of the WIMP with the noble gas creates electron-hole pairs and a strong electric field is then applied. The electrons are guided towards the part of the detector where the gas is held in equilibrium and then, electrons produce ionization that leads to another scintillation. This secondary scintillation is used to discriminate between electron recoil, that is coming typically from gamma and beta radiation, and nuclear recoil, typically coming from neutrons and WIMPs.
Other experiments as LUX that contains a dual-phase 350 kg of liquid xenon are being improve. The LUX-Zeplin experiment (LZ) [104], merged from the groups LUX and ZEPLIN, expects to start in 2020.

DAMA: This direct detection experiment [105, 96, 106] is searching for WIMPs located in the galactic halo using radiopure scintillators (NaI, Xe). Between 1996 to 2002 the first generation of detectors DAMA/NaI [107, 108] were operated, and the second generation, DAMA/LIBRA [99, 109, 110] started at 2003. DAMA/NaI was conceived to investigate the model independent annual modulation signature expected for dark matter. Since 1997, the experiment has reported a positive model independent evidence of a cosine-like annual modulation signal that, according to DAMA collaboration, is compatible with the presence of dark matter particles in the galactic halo [96, 106, 110, 111, 112, 113]. The second generation experiment DAMA/LIBRA has also confirmed a peculiar annual modulation signal with all the characteristics of a dark matter-induced signal in the 2-6 keV energy region, at 7.5σ level. Including

the data of both, DAMA/NaI and DAMA/LIBRA experiments, the C.L. increases to 9.3σ [106, 110]. The interpretation of this signal as WIMP-like dark matter evidence has raised many questions. Due to the non observation of this signal with other experiments, the DAMA collaboration claims that it is not a straightforward direct comparison with other experiments using different target materials. Many studies had been made [114, 115, 116] in order to understand the nature of the DAMA annual modulation.
The particle detector experiment ANAIS (Annual modulation with NAI Scintillators) [117, 118] has adopted the same target material and the same experimental technique than DAMA/LIBRA. The experiment located at the Canfranc Underground Laboratory is taking data since August 2017. The goal of ANAIS is to confirm or refute the signal detected by DAMA and helps to settle this controversial situation. The first result threw by ANAIS in March 2019 [119], supports the goal of reaching a 3σ sensitivity to DAMA / LIBRA results considering 5 years of taking data. Additionally, there are several other experiments trying to test the model-independent signal of DAMA. Those are COSINE- 100 [120, 121, 122, 123] that is using the same target material than DAMA (NaI-TI), DM-Ice17 [124] and KIMS [125].

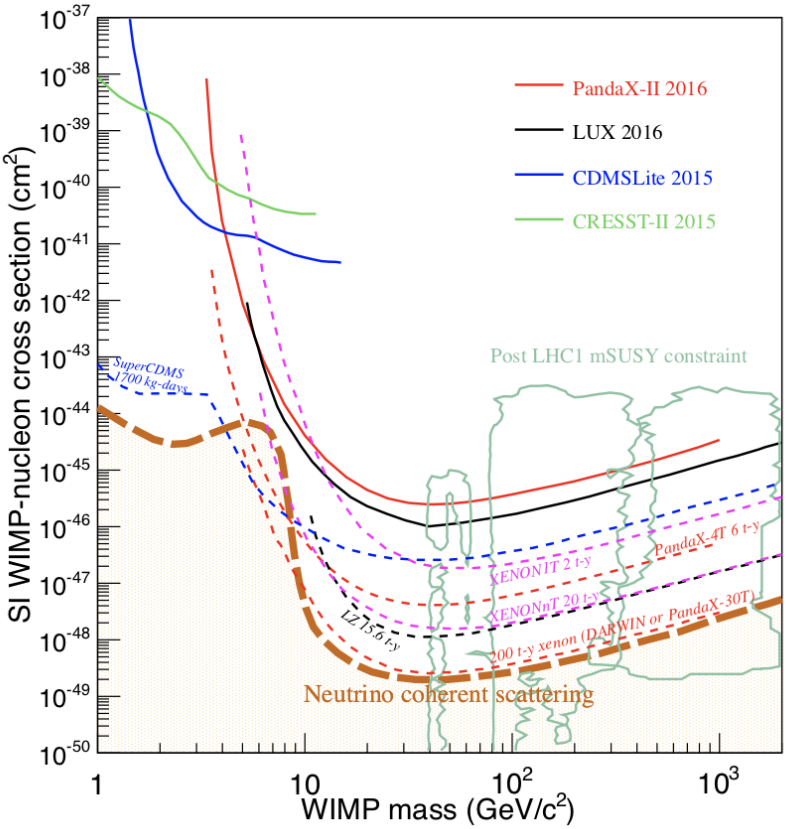

Figure 1.11: Spin independent (SI) WIMP-nucleon scattering cross section versus the dark matter mass. The solid lines represent the upper limits on the SI WIMP-nucleon scattering cross section set by the current leading experiments including PandaX-II [8], LUX [9], CDMSLite 2015 [10] and CRESST-II [11]. Dashed curves are the projected sensitivity on the direct detection cross section, whise the ones included are XENON1T [12], PandaX-4T, XENONnT [12], LZ [13], DARWIN [14], SuperCDMS. The neutrino coherent scattering background curve data [15] (dashed grey orange curve) is included for comparison [16].

1.4.3 Indirect searches

Dark matter particles can be detected *indirectly* using particles from the space. The idea consist in searching the annihilation products of WIMPs dark matter into SM particles, such as

$$\chi + \chi \to q\bar{q}, \tau^+\tau^-, ... \to \gamma, e^+, \nu, \bar{p}, \bar{D}, \tag{1.77}$$

where positrons, neutrinos, anti-protons and anti-nuclei (antimatter) is also produced [126] (see figure (1.12)). We can search anomalous components in the cosmic radiation if these annihilation are significant in the dark matter structure contains in our Universe. Is expected that such radiation is proportional to the annihilation or decay rate which depends on the square of the dark matter density in the case of annihilation and on the dark matter density in the case of decays.

In annihilation process, final states consists typically of a partcile and its antiparticle. Most of these par-

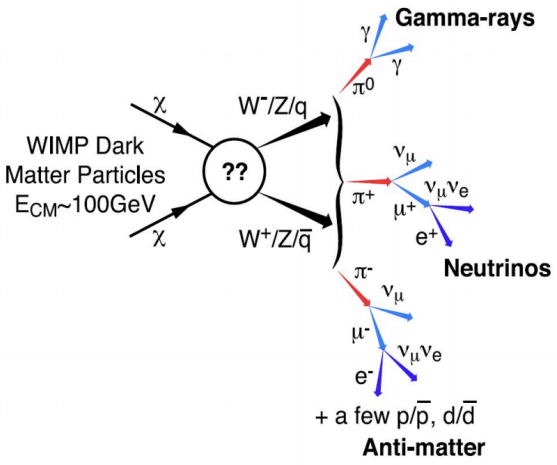

Figure 1.12: Dark matter annihilation into a pair of quarks or vector boson where the final states are photons, neutrinos or antimatter [17].

ticles decay fast and the final products of these interactions will be only stable particles. Final states can consist of e^-e^+ and $\mu^-\mu^+$ which can produce a hard $e^\pm$ spectrum while muons also can produce neutrinos. Pions, protons and anti-pions, nuclei and anti-nuclei will be present when WIMPs annihilate (decay) into quarks, gluons and weak gauge bosons. Charged pions produce electrons, positrons and neutrinos, whereas neutral pions will decay into gamma rays. In the case of $\tau^+\tau^-$, they can decay hadronically to pions, thus leading to gamma rays flux or produce a neutrinos and $e^\pm$ flux. When the final states are neutrinos, they will not decay and they will only produce a neutrino spectrum.

Photon flux from dark matter annihilation

When WIMPs self-annihilate or decay into SM particles, gamma-ray photons would produce a continuous gamma-ray spectrum, called it ***prompt emission***. The prompt comming from primary Gamma-rays can come from differents kind of annihilation. The annihilation of WIMPs into **pair of** $\gamma\gamma$, γH, γZ or into a **photon plus a neutral state** would give rise to a signal of dark matter evidence. This signal will be a *line* of gamma-rays that astrophysical sources are unlikely to produce. The signal coming from monocromatics gamma-rays with energy $E_\gamma = m_{\rm DM}$ for $\gamma\gamma$ ($E_\gamma = m_{\rm DM}\left(1 - \frac{m^2_{Z,H}}{4m^2_{\rm DM}}\right)$ for γH and γZ) will proceed from the annihilation via loops of charged particles (or some others mediators), so this annihilation channel will be suppressed by $\mathcal{O}(\alpha^2_{\rm em})$. Signals at tree level originates when dark matter particles annihilate into s pair of **quarks**, **leptons**, **gauge bosons** and **Higgs boson**. The decay or annihilation of these primary annihilation products will lead to a continuum gamma-rays signal. The spectra for the different annihilation channels can ve calculated with event generators depending of the model that give origen to the dark matter particles [127]. A flux of gamma-rays can also arise via internal bremsstrahlung (IB) whenever WIMPs annihilate into pairs of charged particles. IB consist in the emision of an additional photon in the final states. It can be separated into *Virtual internal bremsstrahlung* (VIB), originated by one of the internal particles in the annihilation diagram of this process [128, 129] and *Final state radiation* (FSR) when photons are directly radiated from the external legs. FSP is dominated by collinear photons (i.e. the final state particles are almost on mass-shell) and it will give rise to a continuum of gamma-rays which will show a pronounced signal at energies smaller than the mass of the dark matter. Photons coming from FSP are often the main source for IB. Nevertheless, other interactions can lead VIB as the dominated process in the signal [128]. Figure (1.13) shown different diagrams to WIMPs annihilation into a pair charge particle final state. The FSR process is shown in diagrams (a) and (b). VIB, when photons radiated from virtual charged particles, is shown in (c). Secondary emissions of gamma-rays can

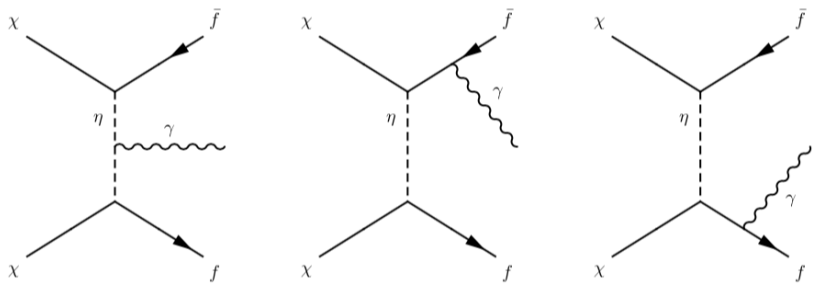

Figure 1.13: Different diagrams to WIMPs annihilation into a pair charge particle final state. Diagrams (a) and (b) refers to FSR process while (c) corresponds to VIB.

be produced in processes as *Inverse Compton scattering* [130] and *Bremsstrahlung* [131] giving an extra contribution of the signal.

Given a solid angle $d\Omega$ in a given direction the prompt differential gamma-ray flux for annihilating dark

matter per unit of energy interval is

$$\frac{d\phi_\chi}{dEd\Omega} = \frac{1}{4\pi}\frac{\langle\sigma v\rangle}{2} r_\odot \frac{\rho_\odot^2}{m_\chi^2} \sum_f \left(\frac{dN_f}{dE} B_f\right) \mathcal{J}(\psi), \tag{1.78}$$

In the case of dark matter annihilations of particles which are non self-conjugated, a factor 1/2 must be added to the last equation. Parameter m_χ is the mass of the dark matter particle, $r_\odot = 8.5$ kpc is the distance from the Sun to the center of the Milky way [132, 133] and $\rho_\odot = 0.4[\text{GeV}]\text{cm}^{-3}$ the dark matter density at $r_o dot$. The differential gamma-ray spectrum is given by $\frac{dN_f}{dE} B_f$ and will yield by the annihilation of dark matter into Standard Model particles f with a branching ratio B_f. The term $\mathcal{J}(\psi)$ is the astrophysical J-factor given by

$$\mathcal{J}(\psi) = \frac{1}{r_o dot} \int_{l.o.s} \left(\frac{\rho[r(l)]}{\rho_{odot}}\right)^2 dl(\psi). \tag{1.79}$$

the J-factor quantifies the integral of the dark matter profile along the line-of-sight (l.o.s) l. The term $\rho(r)$ denotes the dark matter density profile as a function of the radius of the Milky Way r and the l.o.s., l, as a measure of the Galactic position of the Sun is given by

$$r(l,\psi) = \sqrt{r^{2_{odot}} + l^2 - 2r_{odot} l \cos\psi}.$$

The angle ψ represent the angle pointing to the galactic center and the direction of observation.

Sommerfeld Enhancement

We will consider a scenario where dark matter self-interations by the theory are allowed. Assuming that the annihilation of the dark matter particles into the Standard Model particles is a localized interaction, if there are not self interactions between the dark matter particles, the annihilation process looks normal, as in the left part of figure (1.14). With self-interactions of dark matter, the scenario changes to the right side of figure (1.14). Dark matter particle can interact with itself via long-range force before the annihilation take place. the figure shown that if we introduce a new scalar A that couples to the dark matter as $\bar{\chi}\chi A$, then the two legs of the diagram can exchange multiples states of A before the hard annihilation occurs at the origin. This exchange will alters the wave function of the dark matter particles so the probability of finding them at the annihilation site will depend of the modified wave function in the presence of an interaction potential. The last effect is known as the Sommerfeld enhancement. Due to it is not the purpose of this thesis, we will not enter in more details and for a full explanation we strongly suggest check [18].

There are different experiments searching for gamma-rays in the sky. Indirect gamma-rays signal coming

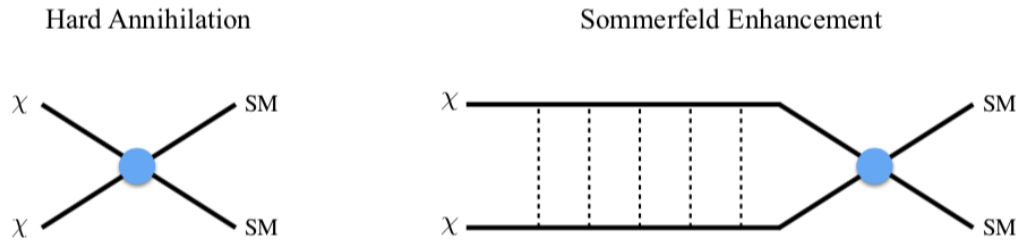

Figure 1.14: Scheme of the annihilation of dark matter without (left) and with (right) considering Sommerfeld enhancement [18].

from annihilation of dark matter have been explored from the Fermi-Lat telescope. Fermi Gamma-ray Space Telescope was launched in 2008. With a large field of view of 2.4 sr, it is enables to look at large portion of the sky in a once. MAGIC, HESS, HAWC and VERITAS telescopes have tested the same signal at the scale of TeV energies. These experiment can achieve larger effective areas, lower thresholds and lower background. Gamma-rays originated from the annihilation of dark matter are expected from targets coming from Galactic and extragalactic dark matter structures as the dark matter halo located in our galaxy [86] and the Galactic center [134, 135]. Extragalactic dark matter searches are performed and exploring the cumulative contribution from group of galaxies, the anisotropies in the isotropic diffuse gamma-ray background (IGRB) [136] and via cross-correlations of the gamma ray signals [137]. HESS collaboration has observed a strong gamma-ray signal that is coming from the center of the galaxy, consistent with a point source [134]. Dwarfs spheroidal galaxies (dSph) [138, 139] is one of the most investigated regions for Galactic searches due to the very low background coming from cosmic rays interactions and because is dominated by dark matter. VERITAS telescope has observed the galactic center [140], a galaxy cluster [141] and some dwarf spheroidal galaxies [142, 143]. The Fermi-LAT collaboration has realized many dark matter searches about satellite galaxies [144, 145], IGRB [146], the galactic diffuse [147], clusters of galaxies Ackermann:2010rg, and gamma-ray lines [148, 149, 150].
There have been many *claims* for dark matter from the public Fermi-LAT data [151, 152]. Nevertheless, in all the cases the signals have their origin due to astrophysical [153] or instrumentation reasons. Best targets to search gamma-rays annihilation signals are dense and/or places where the astrophysical background is low.

- **Galactic center (GC)** is a highly dense target but with a lot of background. The GC is maybe the brightest source of gamma-rays originated from dark matter annihilation. Data collected by Fermi-LAT shown a bright excess in the region around the GC at energies of 2 [GeV] [154]. At the beginning, the gamma-ray excess was associated to WIMP dark matter annihilating in the Galactic halo, with a mass of ≈ 50 [GeV]. Currently, gamma-rays emissions source is associated to a stellar bulge [52, 155] and sub-threshold millisecond pulsar-like point sources [156, 157, 158]. For the other hand, a gamma-ray emission at 511 KeV originated around the GC has been observed over more than four decades [159, 160]. The signal is uncorrelated with known astrophysical sources and will

be indicating the injection of positrons of low energies located in the inner kiloparsec around the center of our Galaxy. The dark matter interpretation of light dark matter annihilation with masses around $1 - 100$ MeV [161, 162] is has been currently challenged by cosmological arguments [163]

- **Dwarf Galaxies)** are satellite galaxies of the Milky Way and are considered as dark matter dominated and with low astrophysical background. Dwarf spheroidal galaxies such as Indus II, Reticulum II and Tucana III show an excess of gamma-rays [158]. The signal could be an indication of dark matter annihilation with a mass about $40 - 100$ [GeV]. Due to the astrophysical J factor estimates that for these king of objects the uncertainties are significant, new data coming from Fermi-LAT [25] and radio searches ATCA/SKA [164] will clarify the origin of the gamma-rays excess in the next years.

- **Galaxy clusters** are considered the most massive dark matter structures in the Universe and are considered good targets for indirect searches of dark matterc̃iteJeltema:2008vu, Pinzke:2011ek. Numerical simulation predict that galaxy cluster should hots a large population of dark matter substructures, enhancing the possibility of detect dark matter. Constraints obtained from this population exclude the thermal cross sections of WIMPs with masses up to 100 [GeV], nevertheless is affected by a big uncertainty in the modeling. An unknown X-ray line at 3.5 keV has been reported in galaxy clusters by several groups [165]. One of the possibilities of the origin of this signal is by an imperfect model of atomic transitions [166] of by phenomena such dark matter annihilation or axion to photon conversion [167].

A significant isotropic radio emission between 22 MHz and 1- GHz has been detected by ARCADE-2 [168]. Extra galactic dark matter annihilation [169] is one of the possibles explanation to the signal. Future measurements of the radio background would clarify the origin of this emission [170] that at present is unknown.
Concerning the future prospects of dark matter indirect detection through gamma-rays, the next years will bring a big quantity of big data. New data will allow to identify a signal or exclude many of the main common dark matter scenarios setting stronger constraints. Ground based telescope as HESS [**?**] and the Cherenkov telescope array (CTA) [26] will improve the dark matter searches scenario.

For another scenario, anti-matter particles are not so abundant and the background is less important. Because of that, they can be an excellent signature of WIMP annihilation even if they are more difficult to detect than gamma-rays. For example, an excess in the measured rate of the flux of cosmic positrons over the predicted rate could be due to the product of dark matter annihilations. This kind of signal was looked by PAMELA [171]. Also, antiprotons may be produced by WIMP annihilation in the galactic halo and the signal has been explored by the Alpha Magnetic Spectrometer (AMS-02) [172].

1.4.4 Collider searches

The possible production of new neutral and weakly interacting particles at colliders might be interpreted as dark matter only if they characteristic are sustained by astrophysical observations. In fact, colliders cannot determine if what they are seeing is the dark matter that surrounds the Universe. Only direct and indirect reaches can provide a way to confirm whether a potential signal is due to dark matter [173]. In case that we can produce dark matter at colliders, we will have to comprehend the forces that connect dark matter to ordinary matter due to, as in indirect searches, dark matter relies upon the existence of interactions between the colliding to Standard Model particles.

There are many types of colliders in the past and at present that are testing the Standard Model as well as new physics. These include proton-proton collider as the Large Hadron Collider (LHC), providing a center of mass energy up to 14 TeV and the Large Electron-Positron collider (LEP) which can provides stringent measurements of particular interactions types, due to the relatively clean electron beam source. Collider searches of dark matter are based on the detection of the visible counterpart of the signal, as jets, photons or charged leptons and dark matter will be manifested as missing energy. Missing traverse energy or momentum (MET) is the key experimental parameter used to hunt dark matter. The most popular searches of dark matter at the LHC are referred to as "mono-X" searches and consist of a Standard Model particle recoiling against the missing energy that was attributed to the weakly or non interacting dark matter particle. ATLAS and CMS [174, 175, 176, 177, 27, 178, 179, 180, 181] are the leading experiments searching for these kind of signals at the LHC. To date, strong constraints can be set on the dark matter parameter space considering that there is not a signal of dark matter yet.

2

Models Beyond the Standard Model

"I mean, it's sort of exciting isn't it? Breaking the rules."

Hermione Granger

Harry Potter and the Order of the Phoenix

In the next chapter we will define the different models that we studied in our research. We will list the main features and the differences between the models and also give some motivations about the importance of study them. Finally, we will present the main constrains that we considered in our research in the tree models.

2.1 Inert Higgs Doublet Model

The Inert Higgs Doublet Model (IHDM) includes a second inert Higgs doublet field η. Additionally, a discrete $\mathbb{Z}_2$ symmetry is added in order to make the lightest particle of the new field completely stable, considering a Weakly Interactive Massive Particle (WIMP) as the dark matter particle in a freeze-out scenario. The new scalar field η is odd under $\mathbb{Z}_2$ symmetry while the Standard Model particles are even. The new symmetry also avoid *Flavor Changing Neutral Currents (FCNC)* [182] in the model, forbidding some interactions terms between η and the fermions of the Standard Model.
There are two types of two doublet fields models that satisfy the FCNC conditions:

- Type I, where the Standard Model fermions will only couple to the Higgs doublet ϕ. This is the case of the IHDM.
- Type II, as in the MSSM case ,the up-like fermions will couple to the Higgs doublet ϕ while the down-like fermions will couple to the inert Higgs doublet η.

The most general renormalizable scalar potential for IHDM is

$$\begin{aligned}\mathcal{V} &= m_\phi^2\phi^\dagger\phi + m_\eta^2\eta^\dagger\eta + \lambda_1(\phi^\dagger\phi)^2 + \lambda_2(\eta^\dagger\eta)^2 + \lambda_3(\phi^\dagger\phi)(\eta^\dagger\eta) + \lambda_4(\phi^\dagger\eta)(\eta^\dagger\phi) \\ &+ \frac{\lambda_5}{2}\left((\phi^\dagger\eta) + (\eta^\dagger\phi)\right)^2, \end{aligned} \tag{2.1}$$

where m_ϕ^2, m_η^2 and λ_{1-5} will be real. For the other hand, λ_5 can be a complex parameter that is made real adding an extra phase (Apendix A.3) and keeping the potential invariant [183].
To ensure the scalar potential stability, the next conditions are necessary [184]

$$\lambda_1, \lambda_2 > 0; \qquad \lambda_3, \lambda_3 + \lambda_4 - |\lambda_5| > -2\sqrt{\lambda_1\lambda_2}. \tag{2.2}$$

To choose the lightest neutral particle of the inert doublet field as the dark matter candidate at tree level, we considered the conditions

$$\lambda_4 + \lambda_5 < 0, \tag{2.3}$$

$$\lambda_5 < 0. \tag{2.4}$$

In order to calculate tadpole equations we must to evaluating the fields at the vacuum in

$$\frac{\partial V}{\partial \psi}|_{\psi_k} = \langle\psi\rangle = \frac{\partial V^\dagger}{\partial \psi}|_\psi = \langle\psi\rangle = 0, \tag{2.5}$$

where ψ can be both, ϕ or η. Both the Higgs doublet field ϕ and the inert doublet field η, will transform under $SU(2)$ as

$$\psi \to \psi' = U\psi, \quad U = e^{i\vec{\alpha}\cdot\vec{\sigma}}, \tag{2.6}$$

where $\vec{\sigma}$ are the respective group generators where we can see three free parameters, α_j (j=1,2,3). Due to we want that $\mathbb{Z}_2$ symmetry continue unalterable in the vacuum, we fix the unitary gauge and the field η will not acquire a vacuum expectation value (vev). The expression of the doublet fields in the vacuum are

$$\langle\phi\rangle = \frac{1}{\sqrt{2}}\begin{pmatrix} 0 \\ v \end{pmatrix}, \qquad \langle\eta\rangle = \frac{1}{\sqrt{2}}\begin{pmatrix} .0 \\ 0 \end{pmatrix} \tag{2.7}$$

Tadpole equation obtained is

$$m_1^2 + \lambda_1 v^2 = 0. \tag{2.8}$$

where we considered that $SU(2) \times U(1)$ is broken spontaneously. Here, $v = 256$ [GeV] as the same value that the Higgs field acquire in the vacuum. Expanding the fields ϕ and η around the vacuum, we get

$$\phi = \begin{pmatrix} 0 \\ (v+\phi)/\sqrt{2} \end{pmatrix}, \tag{2.9}$$

$$\eta = \begin{pmatrix} \eta^{\pm} \\ (\eta_R + i\eta_I)/\sqrt{2} \end{pmatrix}. \tag{2.10}$$

Here, ϕ is the physical Higgs boson Standard Model-like. The gauge bosons G^0 y $G^{\pm}$ are absent due, as we mention before, to we are working in the unitary gauge. For the other hand, we can see four new fields coming from the inert sector: a neutral scalar CP-even η_R , a neutral scalar CP-odd η_I and two charged complex scalars $\eta^{\pm}$.

Calculating the mass matrix elements at tree level considering the equation (2.8), we get that the physical mass terms are

$$m_{\phi}^2 = 2\lambda_1 v^2, \tag{2.11}$$

$$m_{\eta^{\pm}}^2 = m_{\eta}^2 + \frac{\lambda_3}{2}v^2, \tag{2.12}$$

$$m_{\eta_R}^2 = m_{\eta}^2 + (\lambda_3 + \lambda_4 + \lambda_5)\frac{v^2}{2}, \tag{2.13}$$

$$m_{\eta_I}^2 = m_{\eta}^2 + (\lambda_3 + \lambda_4 - \lambda_5)\frac{v^2}{2}. \tag{2.14}$$

The next equations can be written If we want to study the dependence of the parameters $lambda_k$ ($k = 3, 4, 5$) and m_η with respect to the physical masses described above

$$\begin{aligned}
\lambda_3 &= \frac{2}{v^2}\left(m_\phi^2 - m_{\eta_R}^2 + \lambda_{345}\frac{v^2}{2}\right), \\
\lambda_4 &= \frac{m_{\eta_R}^2 + m_{\eta_I}^2 - 2m_\phi^2}{v^2}, \\
\lambda_5 &= \frac{m_{\eta_R}^2 - m_{\eta_I}^2}{v^2}, \\
m_2^2 &= m_{\eta_R}^2 - \frac{v^2}{2}\lambda_{345},
\end{aligned} \tag{2.15}$$

with $\lambda_{345} = \lambda_3 + \lambda_4 + \lambda_5$ and fixing the mass of the Higgs according to the experimental data $m_\phi^2 = 125$ [GeV].

2.2 The simple Scotogenic Model

The Scotogenic model, introduced by Ernest Ma in 2006 [185] is considered one of the simple models containing a WIMP-like dark matter particle that can be a scalar or a fermion. The model includes some of the features of the IHDM as the $\mathbb{Z}_2$ symmetry to stabilize the dark matter particle and forbids interactions to produce neutrino masses tree level. Using the particles of the dark sector, neutrino masses are generated at 1-loop level. The particle content of the model, including the transformations laws under the new symmetry and their respective quantum numbers are listed in the Table 2.1. The scalar

	Standard Model			Fermions	Scalar
	L	e	ϕ	N	η
$SU(2)_L$	2	1	2	1	2
Y	-1	-2	1	0	1
Z_2	+	+	+	−	−
l	1	1	0	0	0

Table 2.1: Particle content and quantum numbers of the model.

sector is composed by one new doublet field η where the respective physical masses were described in equation (2.14). The fermionic sector is composed by three Majorana neutral heavy fermions N_i, with $i = 1, 2, 3$, all of them odd under $\mathbb{Z}_2$. The scalar potential to the Scotogenic model is the one described by the equation 2.1. New terms of interaction will appear in the Lagrangian

$$\mathcal{L}_{int} \subset -Y_N^{\alpha\beta}\bar{N}_\alpha\tilde{\eta}^\dagger L_\beta - \frac{1}{2}\bar{N^\alpha}M_{\alpha\beta}N^{\beta\,c} + h.c. \tag{2.16}$$

The last one is the Majorana mass term considering M_{ij} as a mass matrix. The terms Y_N are the new yukawa terms and the only interaction couplings between the new fermions N_i and the Standard Model leptons.

2.2.1 Neutrino mass generation

The term $-Y_{ij}\bar{L}^i\tilde{\phi}N_R^j + h.c$ ($\tilde{\phi} = i\sigma_2\phi^*$) is forbidden due to $\mathbb{Z}_2$ symmetry and cannot lead to a tree level neutrino masses. Involving the new scalars and fermions, after symmetry breaking the resulting formula for the mass of the lightest neutrinos matrix at one loop is

$$\mathcal{M}^{\nu}_{\alpha\beta} = \frac{Y^N_{\alpha i}Y^N_{\beta i}}{32\pi^2} m_{N_i}\left[\frac{m^2_{\eta_R}}{m^2_{\eta_R}-m^2_{N_i}}\ln\left(\frac{m^2_{\eta_R}}{m^2_{N_i}}\right) - \frac{m^2_{\eta_I}}{m^2_{\eta_I}-m^2_{N_i}}\ln\left(\frac{m^2_{\eta_I}}{m^2_{N_i}}\right)\right]. \tag{2.17}$$

where m_{η_R} and m_{η_I} are the respectively masses of η_R and η_I. Equation 2.17 can be defined as

$$\mathcal{M}^{\nu}_{\alpha\beta} = (Y^{N,T}\Lambda Y^N)_{\alpha\beta}, \tag{2.18}$$

where Λ is defined as

$$\Lambda_i = \frac{N_i}{32\pi^2}\left[\frac{m^2_R}{m^2_R-N^2_i}\ln\left(\frac{m^2_R}{N^2_i}\right) - \frac{m^2_I}{m^2_I-N^2_i}\ln\left(\frac{m^2_I}{N^2_i}\right)\right], \tag{2.19}$$

considering

$$\Lambda = \begin{pmatrix} \Lambda_1 & 0 & 0 \\ 0 & \Lambda_2 & 0 \\ 0 & 0 & \Lambda_3 \end{pmatrix}. \tag{2.20}$$

Using the Casas-Ibarra parametrization [186], the new yukawa matrix can be written as

$$Y^N = \sqrt{\Lambda^{-1}}\rho\sqrt{m_\nu}U^\dagger_\nu, \tag{2.21}$$

where ρ is an complex orthogonal matrix, U_ν is the Pontecorvo-Maki-Nakagawa-Sakata matrix and m_ν is the diagonalized neutrino mass matrix. For the Scotogenic model in this research, all the neutrinos will acquire mass.

2.3 The Singlet + Triplet Scotogenic Model

In this section we will review the Singlet + Triplet Scotogenic Model. This generalization of the scotogenic model [185] was proposed in [187] and further studied in several papers [188, 189, 190, 191]. In addition to the SM gauge symmetry there is a discrete $\mathbb{Z}_2$ symmetry, whose role is to make the lightest $\mathbb{Z}_2$-odd or "dark" particle stable and to ensure the radiative generation of neutrino masses. The SM particle content is augmented by the inclusion of a Majorana fermion triplet Σ and a Majorana fermion singlet F, both odd under the $\mathbb{Z}_2$ symmetry. Moreover, the model includes a new scalar doublet η — odd under the $\mathbb{Z}_2$ symmetry, which does not acquire a vacuum expectation value (VEV) — and a triplet scalar Ω, which allows for the mixing of the neutral parts of the new fermions. This triplet scalar field has a zero hypercharge and it is even under the $\mathbb{Z}_2$ symmetry, thus, its neutral component can acquire a

nonzero VEV. The full particle content of the model is given in Table 2.2, with the corresponding charge assignment under the different symmetry groups.

	Standard Model			new fermions		new scalars	
	L	e	ϕ	Σ	F	η	Ω
Generations	3	3	1	1	1	1	1
$SU(3)_C$	1	1	1	1	1	1	1
$SU(2)_L$	2	1	2	3	1	2	3
$U(1)_Y$	-1	-2	1	0	0	1	0
$\mathbb{Z}_2$	+	+	+	−	−	−	+
L	1	1	0	0	0	-1	0

Table 2.2: Particle content and quantum numbers of the Singlet + Triplet Scotogenic Model. The charge assignments of the fields under the global Lepton Number symmetry (L) are also shown.

Taking into account the new fields and symmetries of the model, the relevant terms of the Lagrangian read

$$\begin{aligned}\mathcal{L} \;\subset\; & -Y^{\alpha\beta}L_\alpha e_\beta \phi - Y_F^\alpha(\bar{L}_\alpha\tilde{\eta})F - Y_\Sigma^\alpha \bar{L}_\alpha^c \Sigma^\dagger \tilde{\eta} - Y_\Omega \mathrm{Tr}\left[\bar{\Sigma}\Omega\right] F \\ & - \frac{1}{4}M_\Sigma \mathrm{Tr}\left(\overline{\Sigma}^c\Sigma\right) - \frac{M_F}{2}\overline{F^c}F + h.c. \end{aligned} \tag{2.22}$$

where $\tilde{\eta} = i\sigma_2\eta^*$. The first Yukawa term $Y^{\alpha\beta}$ is the standard model interaction for leptons, which we can assume to be diagonal in flavor (Greek indices stand for family indices).

2.3.1 Scalar sector

The scalar potential $\mathcal{V}$ invariant under the $SU(2)\times U(1)\times\mathbb{Z}_2$ symmetry is

$$\begin{aligned}\mathcal{V} \;=\; & -m_\phi^2\phi^\dagger\phi + m_\eta^2\eta^\dagger\eta - \frac{m_\Omega^2}{2}\mathrm{Tr}\left(\Omega^\dagger\Omega\right) \\ & + \frac{\lambda_1}{2}\left(\phi^\dagger\phi\right)^2 + \frac{\lambda_2}{2}\left(\eta^\dagger\eta\right)^2 + \frac{\lambda_3}{2}\left(\phi^\dagger\phi\right)\left(\eta^\dagger\eta\right) + \lambda_4\left(\phi^\dagger\eta\right)\left(\eta^\dagger\phi\right) + \frac{\lambda_5}{2}\left[\left(\phi^\dagger\eta\right)^2 + \left(\eta^\dagger\phi\right)^2\right] \\ & + \mu_1\phi^\dagger\Omega\phi + \mu_2\eta^\dagger\Omega\eta \\ & + \frac{\lambda_1^\Omega}{2}\left(\phi^\dagger\phi\right)\mathrm{Tr}\left(\Omega^\dagger\Omega\right) + \frac{\lambda_2^\Omega}{4}\left[\mathrm{Tr}\left(\Omega^\dagger\Omega\right)\right]^2 + \frac{\lambda_\eta^\Omega}{2}\left(\eta^\dagger\eta\right)\mathrm{Tr}\left(\Omega^\dagger\Omega\right), \end{aligned} \tag{2.23}$$

where we make the conservative assumption that m_ϕ^2, m_η^2 and m_Ω^2 are all positive, so that the spontaneous electroweak symmetry breaking will be driven by ϕ and (sub-dominantly) by the neutral component of Ω, while η cannot acquire a VEV. Notice that we are using the standard 2×2 matrix notation for the $SU(2)_L$ triplets:

$$\Sigma = \begin{pmatrix} \frac{\Sigma^0}{\sqrt{2}} & \Sigma^+ \\ \Sigma^- & -\frac{\Sigma^0}{\sqrt{2}} \end{pmatrix}, \quad \Omega = \begin{pmatrix} \frac{\Omega^0}{\sqrt{2}} & \Omega^+ \\ \Omega^- & -\frac{\Omega^0}{\sqrt{2}} \end{pmatrix}. \tag{2.24}$$

The other couplings appearing in Eq. 2.23 are constrained by a number of theoretical considerations. First, they must comply with the condition that the potential is bounded from below in order to have a stable minimum. This requirement leads to the following conditions [188, 189]

$$\lambda_1 \geq 0, \quad \lambda_2 \geq 0, \quad \lambda_2^{\Omega} \geq 0, \tag{2.25}$$

$$\lambda_3 + \sqrt{\lambda_1 \lambda_2} \geq 0, \quad \lambda_3 + \lambda_4 - |\lambda_5| + \sqrt{\lambda_1 \lambda_2} \geq 0, \tag{2.26}$$

$$\lambda_1^{\Omega} + \sqrt{2\lambda_1 \lambda_2^{\Omega}} \geq 0, \quad \lambda_\eta^{\Omega} + \sqrt{2\lambda_2 \lambda_2^{\Omega}} \geq 0, \tag{2.27}$$

$$\sqrt{2\lambda_1 \lambda_2 \lambda_2^{\Omega}} + \lambda_3 \sqrt{2\lambda_2^{\Omega}} + \lambda_1^{\Omega} \sqrt{\lambda_2} + \lambda_\eta^{\Omega} \sqrt{\lambda_1} + \sqrt{\left(\lambda_3 + \sqrt{\lambda_1 \lambda_2}\right)\left(\lambda_1^{\Omega} + 2\sqrt{\lambda_1 \lambda_2^{\Omega}}\right)\left(\lambda_\eta^{\Omega} + \sqrt{\lambda_2 \lambda_2^{\Omega}}\right)} \geq 0. \tag{2.28}$$

It is worth noticing that while these conditions ensure that $\mathcal{V}$ is consistently bounded from below at the electroweak scale, the running of the RGEs may lead to breaking of the $\mathbb{Z}_2$ symmetry at some higher energy scale. Another theory restriction comes from the requirement that the expansion of the potential $\mathcal{V}$ around its minimum must be perturbatively valid. In order to ensure this we require that the scalar quartic couplings in Eq. 2.23 are $\lesssim 1$.

As mentioned before, η does not acquire a VEV and therefore the symmetry breaking is driven only by ϕ and Ω, which have non-zero vevs:

$$\langle \phi^0 \rangle = v_\phi, \quad \langle \Omega^0 \rangle = v_\Omega \tag{2.29}$$

The fields η, ϕ and Ω are written as follows

$$\eta = \begin{pmatrix} \eta^+ \\ (\eta_R + i\eta_I)/\sqrt{2} \end{pmatrix}, \quad \phi = \begin{pmatrix} \varphi^+ \\ (h_0 + v_\phi + i\psi)/\sqrt{2} \end{pmatrix}, \quad \Omega = \begin{pmatrix} (\Omega_0 + v_\Omega)/\sqrt{2} & \Omega^+ \\ \Omega^- & -(\Omega_0 + v_\Omega)/\sqrt{2} \end{pmatrix}, \tag{2.30}$$

where Ω_0 is real and does not contribute to the CP-odd scalar sector. After symmetry breaking there are three charged scalar fields (only two of which are physical, since one is absorbed by the W boson), plus three CP-even neutral fields, and one physical CP-odd neutral field (since the other is absorbed by the Z boson). The VEVs in Eq. 2.29 are restricted by the following tadpole equations or minimization conditions

$$\begin{aligned} \frac{\partial \mathcal{V}}{\partial \phi} &= v_\phi \left(-m_\phi^2 + \frac{1}{2}\lambda_1 v_\phi^2 - \frac{\mu_1}{2} v_\Omega + \frac{\lambda_1^{\Omega}}{4} v_\Omega^2 \right) = 0, \\ \frac{\partial \mathcal{V}}{\partial \Omega} &= -2 m_\Omega^2 v_\Omega + \lambda_2^{\Omega} v_\Omega^3 + v_\phi^2 \left(\lambda_1^{\Omega} v_\Omega - \mu_1 \right) = 0, \end{aligned} \tag{2.31}$$

which we solve for m_ϕ^2 and m_Ω^2.

As for the neutral sector, the mass matrix of the CP-even (and $\mathbb{Z}_2-$even) neutral scalars in the basis

(ϕ_0, Ω_0) reads

$$\mathcal{M}_h^2 = \begin{pmatrix} \Big(-m_\phi^2 + \frac{3}{2}\lambda_1 v_\phi^2 + v_\Omega\Big(-\mu_1 + \frac{\lambda_1^\Omega}{4} v_\Omega\Big)\Big) & \frac{1}{2}v\Big(\lambda_1^\Omega v_\Omega - 2\mu_1\Big) \\ \frac{1}{2}v_\phi\Big(\lambda_1^\Omega v_\Omega - 2\mu_1\Big) & \Big(-\frac{1}{2}m_\Omega^2 + \frac{3}{4}\lambda_2^\Omega v_\Omega^2 + \frac{1}{4}\lambda_1^\Omega v_\phi^2\Big) \end{pmatrix}. \tag{2.32}$$

The lightest of the neutral scalar mass eigenstates is identified with the SM Higgs boson, h^0 with mass ~ 125 [GeV], while the second state, H is a heavier neutral scalar.

On the other hand, the mass matrix for the charged scalars is given as

$$\mathcal{M}_{H^\pm}^2 = \begin{pmatrix} \frac{1}{4}\Big(2\lambda_1 v_\phi^2 - 4m_\phi^2 + v_\Omega\Big(4\mu_1 + \lambda_1^\Omega v_\Omega\Big)\Big) & \sqrt{2}\mu_1 v_\phi \\ \sqrt{2}\mu_1 v & \frac{1}{2}\Big(-2m_\Omega^2 + \lambda_1^\Omega v_\phi^2 + \lambda_2^\Omega v_\Omega^2\Big) \end{pmatrix}. \tag{2.33}$$

Note that, while the Z boson gets its longitudinal component only from the Higgs doublet ϕ and not from the triplet (because Ω^0 is real), the charged Goldstone boson is instead a linear combination of ϕ^+ and Ω^+. The VEV of Ω will then contribute to the W boson mass, thus leading to an upper limit $v_\Omega \lesssim 5$ [GeV] [192, 193]:

$$\begin{aligned} m_Z^2 &= \frac{1}{4}\left(g^2 + g'^2\right) v_\phi^2\,, \\ m_W^2 &= \frac{1}{4} g^2 \left(v_\phi^2 + 4\, v_\Omega^2\right)\,. \end{aligned} \tag{2.34}$$

The mass of the new charged scalar bosons will be

$$m_{H^\pm}^2 = 2\mu_1 \frac{(v_\phi^2 + v_\Omega^2)}{v_\Omega}, \tag{2.35}$$

$$m_{\eta^\pm}^2 = m_\eta^2 + \frac{1}{2}\lambda_3 v_\phi^2 + \frac{1}{\sqrt{2}}\mu_2 v_\Omega + \frac{1}{2}\lambda_\eta^\Omega v_\Omega^2. \tag{2.36}$$

Because of the conservation of the $\mathbb{Z}_2$ symmetry, the $\mathbb{Z}_2$-odd scalar field η does not mix with any other scalar. It proves convenient to write it in terms of its CP-even and CP-odd components:

$$\eta^0 = \frac{(\eta_R + i\eta_I)}{\sqrt{2}}.$$

The physical masses of the neutral η field are easily determined as

$$m_{\eta_R}^2 = m_\eta^2 + \frac{1}{2}(\lambda_3 + \lambda_4 + \lambda_5)v_\phi^2 + \frac{1}{2}\lambda_\eta^\Omega v_\Omega^2 - \frac{1}{\sqrt{2}}\mu_2 v_\Omega, \tag{2.37}$$

$$m_{\eta_I}^2 = m_\eta^2 + \frac{1}{2}(\lambda_3 + \lambda_4 - \lambda_5)v_\phi^2 + \frac{1}{2}\lambda_\eta^\Omega v_\Omega^2 - \frac{1}{\sqrt{2}}\mu_2 v_\Omega. \tag{2.38}$$

The difference $m_{\eta_R}^2 - m_{\eta_I}^2$ depends only on the parameter λ_5 which, as we shall see in the next paragraph, is also responsible for the smallness of neutrino masses. In the limit $\lambda_5 \to 0$ lepton number conservation is restored. Hence, by construction, neutrino masses are "natural", in 't Hooft's sense [194],

i.e. they are "symmetry-protected". Moreover, the $\mathbb{Z}_2$ symmetry conservation also makes the lightest of the two eigenstates $\eta_{R,I}$ a viable dark matter candidate, as we will discuss in detail in section **??**.

2.3.2 Fermionic sector

Concerning the fermionic sector, the new triplet scalar Ω allows for a mixing between the singlet and triplet fermion fields — F and Σ — through the Yukawa coupling Y_Ω, as shown in Eq. 2.22: The mass matrix for the new fermions, in the basis (Σ_0, F) is given as

$$\mathcal{M}_\chi = \begin{pmatrix} M_\Sigma & \frac{1}{\sqrt{2}} Y_\Omega v_\Omega \\ \frac{1}{\sqrt{2}} Y_\Omega v_\Omega & M_F \end{pmatrix}. \tag{2.39}$$

When the neutral part of Ω acquires a VEV $v_\Omega \neq 0$, the diagonalization of the mass matrix Eq. 2.39 leads to eigenstates with the following masses (at tree level):

$$m_\chi^\pm = M_\Sigma, \tag{2.40}$$

$$m_{\chi_1^0} = \frac{1}{2}\left(M_\Sigma + M_F - \sqrt{(M_\Sigma - M_F)^2 + 4(2Y_\Omega v_\Omega)^2}\right), \tag{2.41}$$

$$m_{\chi_2^0} = \frac{1}{2}\left(M_\Sigma + M_F + \sqrt{(M_\Sigma - M_F)^2 + 4(2Y_\Omega v_\Omega)^2}\right), \tag{2.42}$$

$$\tan(2\theta) = \frac{4Y_\Omega v_\Omega}{M_\Sigma - M_F}, \tag{2.43}$$

where θ is the mixing angle between the neutral fermion triplet Σ_0 and F, M_Σ and M_F are the Majorana mass terms for the triplet and the singlet, respectively. Although we will not consider this case here, it is interesting to notice that the lightest neutral eigenstate, χ_1^0 or χ_2^0 may also play the role of the dark matter [187], for more recent analyses see [190, 191].

2.3.3 Neutrino masses

The previous subsection has been dedicated to the spectrum of the new fermions. Let us now comment on neutrino masses. By construcion, in the *scotogenic* approach, the dark matter candidate acts as a messenger for neutrino mass generation. Since the $\mathbb{Z}_2$ symmetry is exact, all vertices including new particles must contain an even number of $\mathbb{Z}_2$-odd fields. For this reason neutrinos cannot acquire a tree-level mass term, their masses arising only at the loop level as portrayed in Fig. 2.1.

The relevant interactions for the generation of neutrino masses arise from equations 2.22 and 2.23. The expression for the neutrino mass matrix is [187, 188, 189]

$$\begin{aligned} \mathcal{M}^\nu_{\alpha\beta} &= \sum_{\sigma=1,2} \frac{Y^\nu_{\alpha\sigma} Y^\nu_{\beta\sigma}}{32\pi^2} \mathcal{I}_\sigma(m^2_{\chi_\sigma}, m^2_{\eta_R}, m^2_{\eta_I}) \\ &= \sum_{\sigma=1,2} \frac{Y^\nu_{\alpha\sigma} Y^\nu_{\beta\sigma}}{32\pi^2} m_{\chi_\sigma} \left(\frac{m^2_{\eta_R}}{m^2_{\eta_R} - m^2_{\chi_\sigma}} \ln\left(\frac{m^2_{\eta_R}}{m^2_{\chi_\sigma}}\right) - \frac{m^2_{\eta_I}}{m^2_{\eta_I} - m^2_{\chi_\sigma}} \ln\left(\frac{m^2_{\eta_I}}{m^2_{\chi_\sigma}}\right)\right), \end{aligned} \tag{2.44}$$

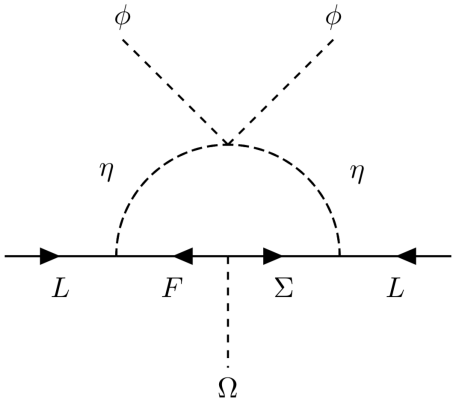

Figure 2.1: "Scotogenic" neutrino masses. After electroweak symmetry breaking the SM-like Higgs acquires a VEV $\langle\phi_0\rangle$.

where α and β are generation indices ($\alpha, \beta = 1, 2, 3$), m_{χ_σ} are the masses of the $\chi^0_{1,2}$ fermion fields and $Y^\nu_{\alpha\beta}$ are the new neutrino Yukawa couplings introduced as a 3×2 matrix [1],

$$Y^\nu \quad = \quad \begin{pmatrix} Y^1_\Sigma & Y^1_F \\ Y^2_\Sigma & Y^2_F \\ Y^3_\Sigma & Y^3_F \end{pmatrix} \cdot V(\theta)\,. \tag{2.45}$$

The matrix $V(\theta)$ is a 2×2 orthogonal matrix that diagonalizes the fermionic mass matrix $\mathcal{M}_\chi$ given in Eq. (2.39). As already noticed before, in the limit $\lambda_5 \to 0$ the two eigenstates m_{η_R} and m_{η_I} are degenerate, hence neutrino masses are zero and the lepton number symmetry is restored. This limit would correspond to an exact cancellation between the η_R and η_I loops. The expression $\mathcal{I}_\sigma(m^2_{\chi_\sigma}, m^2_{\eta_R}, m^2_{\eta_I})$ in Eq. 2.44 involves differences of Passarino-Veltman functions B_0 [195], evaluated in the limit of vanishing external momentum.

We can then rewrite Eq. 2.39 more compactly as:

$$\mathcal{M}^\nu_{\alpha\beta} = Y^\nu_{\alpha\beta} v_\phi \cdot \frac{\mathcal{F}}{v^2_\phi} \cdot Y^{\nu,T}_{\alpha\beta} v_\phi \sim m_D \frac{1}{M_R} m^T_D, \tag{2.46}$$

where

$$\mathcal{F} = \begin{pmatrix} \frac{\mathcal{I}_1}{32\pi^2} & 0 \\ 0 & \frac{\mathcal{I}_2}{32\pi^2} \end{pmatrix}. \tag{2.47}$$

This recalls the structure of the standard type-I seesaw neutrino mass relation, with the Dirac mass term given by $Y^\nu_{\alpha\beta} v_\phi$ and $M_R^{-1} = \frac{\mathcal{F}}{v^2_\phi}$ where $\mathcal{F}$ includes the loop functions. In order to compare with the current determination of neutrino oscillation parameters [59], we will apply a Casas-Ibarra parametrization [186]:

[1] The new fermions Σ and F match exactly the minimum set needed to describe neutrino oscillations. Indeed, if only one of them is present, the neutrino mass matrix would have only one nonzero eigenvalue, hence unable to account for the solar and atmospheric scales.

$$Y^{\nu}_{\alpha\beta} = U_{\nu}\sqrt{m_{\nu}}\rho\sqrt{\mathcal{F}}^{-1}, \tag{2.48}$$

where U_ν is the lepton mixing matrix, m_ν are the neutrino masses (whose squared differences are constrained as in [59]) and the matrix ρ is an arbitrary 2×3 rotation matrix that can be parametrized as [187]

$$\rho \;=\; \begin{pmatrix} 0 & \cos(\beta) & \pm\sin(\beta) \\ 0 & -\sin(\beta) & \pm\cos(\beta) \end{pmatrix}. \tag{2.49}$$

An interesting prediction of this model is that the lightest neutrino is massless. This feature is reminiscent of the "missing partner" nature of this "radiative" seesaw mechanism, in which one of the "right-handed" fermions is missing (there is only one Σ and one F). As a consequence one of the "left" neutrinos can not pair-off and hence remains massless [39].

2.3.4 Neutrinoless double beta decay

Within the symmetrical parametrisation of the lepton mixing matrix [39] the $0\nu2\beta$ effective mass parameter can be neatly expressed as [196]

$$\langle m_{ee}\rangle = \left|\sum_j U^2_{\nu,ej} m_j\right| = \left|\cos\theta^2_{12}\cos\theta^2_{13}\mathrm{m}_1 + \sin\theta^2_{12}\cos\theta^2_{13}\mathrm{m}_2\mathrm{e}^{2\mathrm{i}\phi_{12}} + \sin\theta^2_{13}\mathrm{m}_3\mathrm{e}^{2\mathrm{i}\phi_{13}}\right|, \tag{2.50}$$

where m_i are the three neutrino masses and θ_{1x} are the neutrino mixing angles measured in oscillation experiments. Note that in our case the lightest neutrino is massless ($m_1 = 0$), so that there is only one physical Majorana phase ($\phi \equiv \phi_{12} - \phi_{13}$). Since there is currently no restriction on its value, this phase is a free parameter. Except for this, all other parameters are well measured in oscillation experiments.

We show in Fig. 2.2 the dependence of $\langle m_{ee}\rangle$ on this phase. One sees that, in contrast to the general case where the three active Majorana neutrinos are massive, here the effective mass parameter describing the $0\nu2\beta$ decay amplitude has a lower limit [197, 198].

The pink (light green) band refers to the 3σ C.L. region allowed by current oscillation experiments [59] for normal (inverted) mass ordering. The black lines correspond to the best fit values for both cases. We also show for comparison the 90% C.L. upper limits (shaded regions) from different experiments: CUORE ($\langle m_{\beta\beta}\rangle < 110 - 520$ [meV]) [199], EXO-200 Phase II ($147 - 398$ [meV]) [200], GERDA Phase II ($120 - 260$ [meV]) [201] and KamLAND-Zen ($61 - 165$ [meV]) [202] experiments. The width of these bands is mainly a reflection of the uncertainty in the relevant nuclear matrix elements. The black dashed lines represent the most optimistic future sensitivities for SNO+ Phase II ($19 - 46$ [meV]) [203], LEGEND ($15 - 50$ [meV]) [204] and nEXO after 10 years of data taking ($5.7 - 17.7$ [meV]) [205].

In order to compare, figure (2.3) shows the case where the tree neutrinos have mass. Future sensitivities are represented with the same code than in the case of figure (2.2).

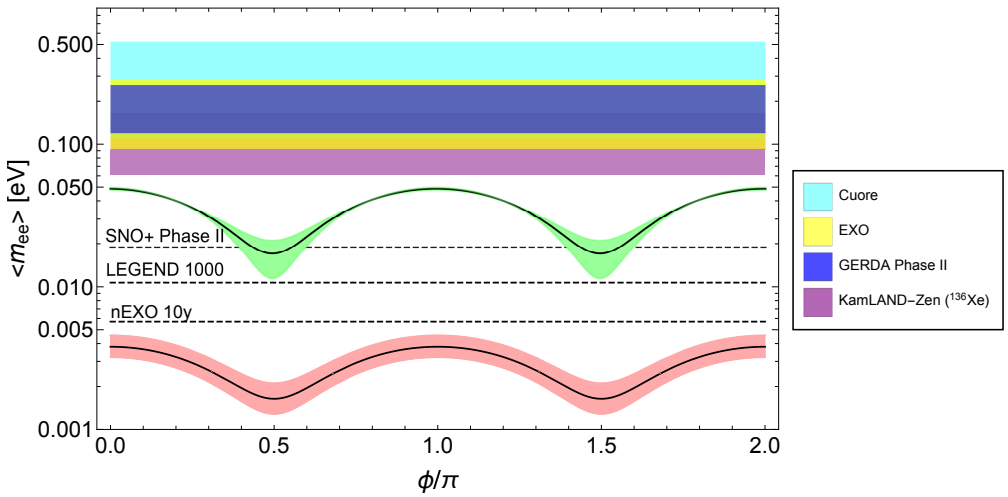

Figure 2.2: Effective $0\nu2\beta$ Majorana mass parameter versus the Majorana phase. The pink (light green) band represents the prediction for the 3σ C.L. region allowed by current oscillation experiments for normal (inverted) mass ordering.

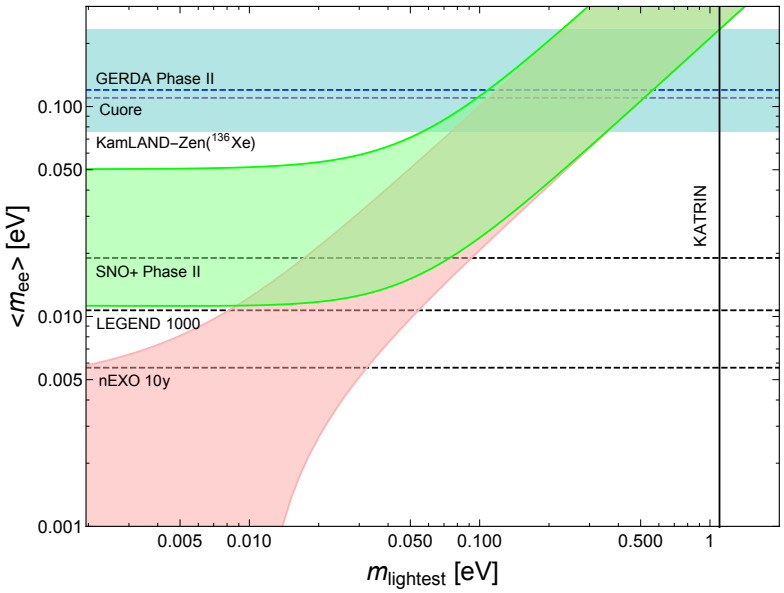

Figure 2.3: Effective $0\nu2\beta$ Majorana mass parameter versus the mass of the lightest neutrino. The purple (blue) dashed line represent the stronger limit for Cuore (Gerda) experiment. The light cyan band represent the lower and upper limits for KamLAND-Zen. The vertical line is the limits for KATRIN for 1.1 eV. The pink (light green) band represents the prediction for the 3σ C.L. region allowed by current oscillation experiments for normal (inverted) mass ordering.

2.4 Constraints

The presence of new particles, absent in the Standard Model, will induce departures from the Standard Model predictions for a number of observables. Throughout our analysis in all the models, we take into account the following constraints.

Theoretical constraints As already discussed in Chapter 2, the coupling and mass parameters appearing in the Lagrangians Eq. 2.16 and Eq. 2.22 are subject to several theoretical constraints. First of all, we must ensure that the scalar potential is bounded from below, which we do by applying the conditions summarised in Eqs. 2.2 for the Inert Higgs Doublet model and Scotogenic model and Eqs. 2.25 for the Singlet + Triplet Scotogenic model. Moreover we must ensure the perturbativity of the couplings, i.e. the scalar quartic couplings are assumed to be $\lesssim \mathcal{O}(1)$. Another theoretical consideration concerns the validity of the $\mathbb{Z}_2$ parity symmetry which is an essential ingredient of both Scotogenic models. Its role is indeed twofold: it stabilizes the dark matter candidate η_R and it justifies the one-loop radiative seesaw mechanism which gives mass to neutrinos. In the case of the Simple + Triplet Scotogenic model compared to the simple simple Scotogenic model initially proposed, the spontaneous breaking of the $\mathbb{Z}_2$ parity symmetry can be naturally avoided in this extension thanks to the effect on the running of the couplings in the scalar sector induced by the inclusion of $\mathbb{Z}_2$-even scalar triplets. Nevertheless, even if the scalar potential is $\mathbb{Z}_2$-preserving at the electroweak scale, the RGEs running could lead to situations where the $\mathbb{Z}_2$ is broken at some higher energy scale [206] [188] (see appendix **??**).
While a thorough analysis of the RGE running is beyond the scope of this thesis, we have not ignored this restriction. Following the prescriptions in [206] for the Scotogenic model and [188] for the Singlet + Triplet Scotogenic model we have avoided this problem by fixing the ranges of variation of the relevant parameters so that the $\mathbb{Z}_2$ parity symmetry is in principle safe up to some high energy scale. Moreover, we have checked numerically that m_η^2 is positive at all energy scales for the benchmark point in the analysis of the Scotogenic model at CLIC and for both benchmark points chosen for the collider study in the Singlet + Triplet Scotogenic model – see Sec. 3.3 and Sec. 4.5, respectively. Finally for the Singlet + Triplet Scotogenic model, although experimental constraints place no upper limit on the mass of the heavy neutral scalar H, we require that its decay width should comply with the perturbative unitarity condition, i.e. $\frac{\Gamma_H}{m_H} < \frac{1}{2}$.

Neutrino oscillation parameters One of the main motivation of all the kind of Scotogenic models is to provide an explanation to the generation of neutrino masses. To ensure this, throughout our analysis we require compatibility with the best-fit ranges of the neutrino oscillation parameters. This is enforced via Eq. 2.48, where the mixing angles and squared mass differences are fixed according to Ref. [59]. For simplicity, the yet unknown Dirac and Majorana phases in U_ν are set to zero. We further assume the currently preferred normal ordering of the light neutrino masses. Interestingly, as already mentioned, the Singlet + Triplet Scotogenic model predicts the lightest active neutrino to be massless.

Lepton flavour violation Both Scotogenic models could be in principle probed through the observation of charged lepton flavour violation, for example, at high intensity muon facilities [207, 208]. However, the negative results of charged lepton flavor violation searches can be used to set constraints on the parameters of the model, in particular on λ_5 which controls the magnitude of the Yukawa couplings. We apply the most stringent limits to date on the branching fraction of some of such rare processes, namely $\mathrm{BR}(\mu \to e\gamma) < 4.2\times10^{-13}$ [209], $\mathrm{BR}(\mu \to eee) < 1.\times10^{-12}$ [210], $\mathrm{CR}(\mu^-, \mathrm{Au} \to e^-, \mathrm{Au}) < 7\times10^{-13}$ [211].

Electroweak precision tests The presence of new physics will affect the gauge boson self-energies, parameterised by the oblique parameters [212]. The most important constraint is expected from the T parameter, which is sensitive to the mass splitting between the neutral and charged components of the scalar fields. For the Singlet + Triplet Scotogenic model due to one of the new fields adquire a vev, we require consistency with electroweak precision data by requiring $v_\Omega \lesssim 5$ [GeV], in order to get a negligible deviation of the ρ parameter from one [188], namely we impose $-0.00018 \lesssim \delta\rho \lesssim 0.00096$ (3σ). Moreover, we fix the Higgs VEV v_ϕ in order to get the correct mass of the W boson, inside its experimental range.

Invisible decay widths of the Higgs boson In both models, if the new neutral scalar masses $m_{\eta_{R,I}}$ are small enough, there can appear new invisible decay channels – at tree level – of the Higgs boson into the lighter stable particles. In the region of parameters where these new invisible decays are possible we enforce that $\mathrm{BR}(h^0 \to \mathrm{inv}) \lesssim 24\%$ [213]. At the loop level, the decay of the Higgs boson into two photons may also be modified by its coupling to the charged scalars. We require consistency at the 3σ level, that is $0.62 \lesssim \mathrm{BR}(h^0 \to \gamma\gamma)/\mathrm{BR}(h^0 \to \gamma\gamma)_{\mathrm{SM}} \lesssim 1.7$.

Dipole moments of leptons At the one-loop level the charged scalars present in our model may also induce sizeable contributions to the magnetic dipole moments of leptons. We have required that the contributions to the anomalous muon magnetic dipole moment induced by the new physics do not exceed the allowed discrepancy between the measured value and the one predicted within the SM [213], $\Delta(a_\mu) = a_\mu^{\mathrm{exp}} - a_\mu^{\mathrm{SM}} = 268(63)(43) \times 10^{-11}$. Contributions to the electric dipole moments arise instead only at the two-loop level, so they are suppressed [214].

Dark matter and cosmological observations In the following, we assume a standard cosmological scenario, where the dark matter candidate, the scalar η_R, was in thermal equilibrium with the Standard Model particles in the early Universe. If η_R is the only candidate contributing to the cosmological dark matter, its relic density must comply with the cosmological limits for cold dark matter derived by the Planck satellite data [19, 20]: $0.1126 \leq \Omega_{\eta_R} h^2 \leq 0.1246$ (3σ range). Values of $\Omega_{\eta_R} h^2 \leq 0.1126$ are also allowed, if η_R is a subdominant component of the cosmological dark matter and allowing for the existence of another candidate. Moreover, our scenario can be tested at direct detection (DD) experiments, which are meant to probe the nuclear recoil in the scattering of galactic η_R off-nuclei inside the detector. We apply the current most stringent limit on WIMP-nucleon spin-independent (SI) elastic scattering cross section, which has been set by the XENON1T experiment at LNGS [21].

Colliders Existing searches for new charged particles at colliders such as LEP and LHC, already set lower limits on their masses in the region below 100 GeV or so [213]. In our analysis we apply the following limits: $m_{H^\pm} \geq 80\,\mathrm{GeV}$ and $122\,\mathrm{GeV} \leq m_{h^0} \leq 128\,\mathrm{GeV}$, the latter to take into account numerical uncertainties.

3

Discrimination between the simple Scotogenic model and the IHDM

"I'm afraid I can't explain myself, sir. Because I am not myself, you see?"

Lewis Carroll

Alice in Wonderland

In the next chapter, we will describe our research in the simple Scotogenic model and the Inert Higgs Doublet model [215]. In order to analyze a specific signature at the future linear collider (CLIC) we studied first the dark matter phenomenology content in both models. We wanted to investigate a feasible benchmark point, capable to explain the total dark matter abundance that exists in the Universe. In the first section, we will describe the numerical analysis that we made to study the relic abundance, the direct detection searches, and their respective main results. Later, we will present our study for a specific signal at CLIC.

3.1 Dark Matter phenomenology

3.1.1 Numerical analysis for the Inert Higgs Scotogenic model and the Scotogenic model

We have developed our own python code for the Montercarlo simulation. The models implementation have done using **SARAH 9.3.1**. The principal decays of the model and the physical particle spectrum have been calculated by `SPHENO 4.0.3` [216, 217] and `FlavourKit` [218] with the files generated by `SARAH` [219, 220]. Dark matter abundance, and dark matter-nucleon Spin independent cross section at tree level have been calculated by `Micromegas 5.0.2` [221]. We had aleatory run 20000 points where the ranges of the principal parameters in both models are listed in table 3.1.

Parameter	Parameter range	Units
λ_1	$[10^-8\ ,\ 1]$	-
λ_2	$[10^-8\ ,\ 1]$	-
λ_3	$[10^-8\ ,\ 1]$	-
λ_4	$[10^-8\ ,\ 1]$	-
$\lvert\lambda_5\rvert$	$[10^-5\ ,\ 1]$	-
m_η^2	$[50^2\ ,\ 700^2]$	$(\mathrm{GeV})^2$
MN_1	$[10^3\ ,\ 5\times10^3]$	(GeV)
MN_2	$[10^3\ ,\ 5\times10^3]$	(GeV)
MN_3	$[10^3\ ,\ 5\times10^3]$	(GeV)

Table 3.1: Input parameters used in the numerical scan for the dark matter study with their respective ranges of variation. All the input of the parameter were considered for the Inert Higgs Doublet model and the Scotogenic model.

3.1.2 Relic density and direct searches

Figures (3.1) and (3.2) show the dark matter abundance versus the dark matter mass of η_R in the Scotogenic model and the Inert Higgs Doublet model, respectively. In both the black tiny band represent the range of relic density for cold dark matter measured by Planck Satellite at 3σ. The cyan (magenta) dots are the results falling exactly over the Planck band and can explain the total relic abundance that exists in the Universe for the Scotogenic model (Inert Higgs Doublet model). For the two models these

points are located in masses close to $400-700$ GeV. In the case of the pink (blue) dots, the neutral scalar η_R in the Scotogenic model (Inert Higgs Doublet model) is a subdominant candidate of dark matter and another dark matter candidate is required. In both, the dark grey points represents the results that are not allowed by the current limits by XENON1T [21] for WIMP-nucleon spin independent elastic scattering cross sections which will be explained in the next section. Light grey points depict the results that are forbidden for any of the constraints listed in section (2.4) as the ones excluded by the relic abundance scenario.

Lets now describe the plots in both figures. The first drop at ~ 60 GeV correspond to the Z boson generation when $m_{\eta_R} \sim M_Z/2$. The second drop is for the Higgs boson generation when $m_{\eta_R} \sim M_{h^0}/2$. Both annihilation channels are via s-channel. For masses around 90 GeV quartic interactions become important and η_R annihilate into W^+W^- that is the third drop that appear in the figure. Also, coannihilation of η_R with η_I and $\eta^\pm$ that contribute to lowering relic abundance may appear in all regions of the parameter space where the splitting between the masses is small. In the case of the simple Scotogenic model, for scales of energy equivalent to the mass of the lightest fermion N_i, **dark matter will annihilate into charge and neutral Standard Model leptons when the propagator is at least one of the new neutral fermions**. That also will contribute to lower the value of dark matter abundance in comparison with the Inert Higgs Doublet model where the neutral fermions N_i are not included. All the Feynman diagrams contributing to the annihilation and coannihilation of η_R are in Appendix (D.1).

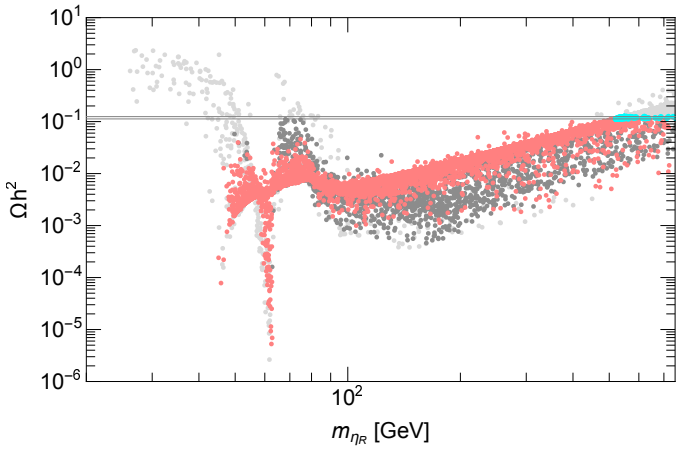

Figure 3.1: Relic density $\Omega_{\eta_R} h^2$ vs the mass m_{η_R}. Cyan points are falling within the 3σ C.L. band measured by Planck [19, 20] for cold dark matter scenario. Pink points represent the solutions with a relic density allowed by the experimental results. Light grey dots are excluded for one or more of the constrains mentioned at section 2.4. Dark gray results are excluded by the current limit of direct searches imposed by XENON1T [21].

Our dark matter scenario can be proved by direct searches. The Feynman diagrams for direct detection searches are summarized in figure (3.4). We can notice that the tree level η_R-nucleon spin independent elastic scattering cross section will mediated through the Higgs boson h^0 and the Z boson when the mas splitting between η_R and η_I is small. Figure (3.3) shows the results for direct searches at tree level in the Scotogenic model (up) and the Inert Higgs Doublet model (down). The vertical axis represent the η_R-nucleon spin independent elastic scattering cross section where each point have been weighted

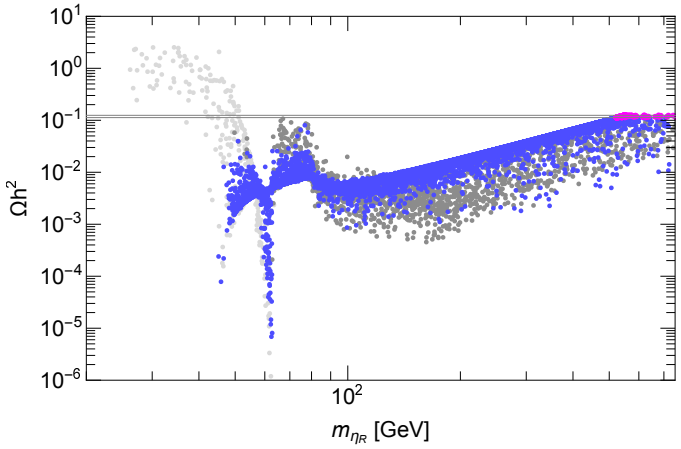

Figure 3.2: Relic density $\Omega_{\eta_R}h^2$ vs the mass m_{η_R}. Magenta points are falling within the 3σ C.L. band measured by Planck [19, 20] for cold dark matter scenario. Blue points represent the solutions with a relic density allowed by the experimental results. Light grey dots are excluded for one or more of the constrains mentioned at section **??**. Dark gray results are excluded by the current limit of direct searches imposed by XENON1T [21].

by $\xi = \Omega_{\eta_R}/\Omega_{\text{Planck}}$. In the horizontal axis we have the mass of η_R. The color code is the same used in figure (3.1) and figure (3.2). Lets analize both plots related with direct searches in both models in figure (3.3). simple Scotogenic model (Inert Higgs Doublet model): the dark magenta line represent the recent upper limit set by XENON1T experiment on WIMP-nucleon spin independent elastic scattering cross section[21]. The results into the dark blue (dark magenta) region are excluded. The non excluded points that can be considered as the only dark matter candidate fall in the region of masses around $500 - 600$ GeV in contrast with the points of masses below 100 GeV that are excluded by XENON1T. The interaction of η_R with the nucleon via the Higgs will be the dominant in the full parameter space due to the interaction with Z boson will depend of the mass splitting between η_R and η_I. The vertex with the Higgs boson is shown in fig. (D.3) where we can notice that there is a strong dependence of the parameter $\lambda_{345} = \lambda_3 + \lambda_4 - \lambda_5$. Contrarily, for some extensions of the Scotogenic model when more particles are added, the same vertex will count with an extra contribution that will helps to decrease the value of the η_R-nucleon cross section [222].

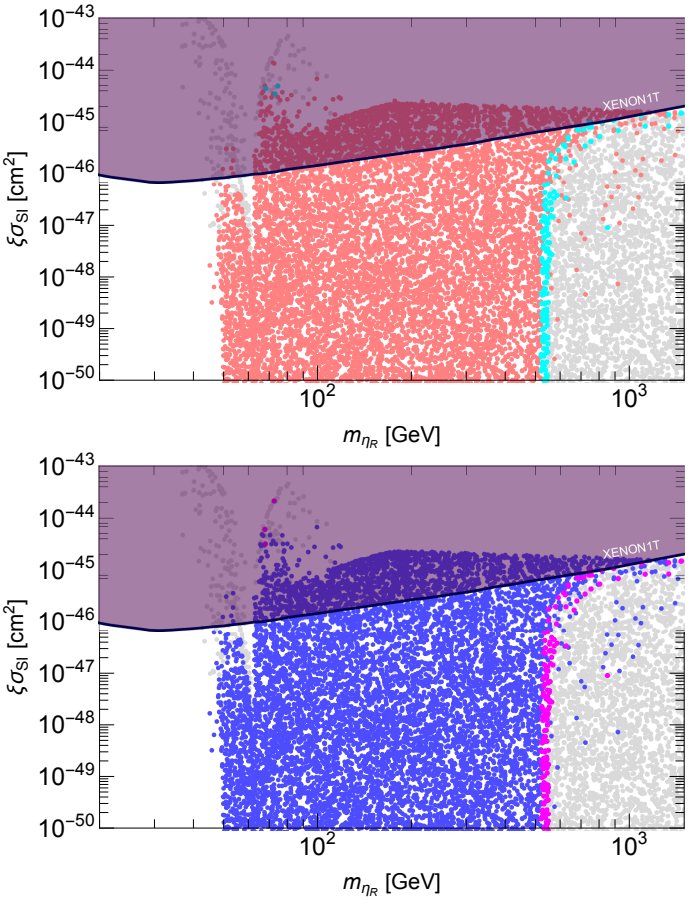

Figure 3.3: Up(Down): η_R-nucleon spin independent elastic scattering cross section versus the mas of η_R for the Scotogenic model (Inert Higgs Doublet model). Color code displayed on the text. The dark magenta line denotes the upper bound from XENON1T [21] .

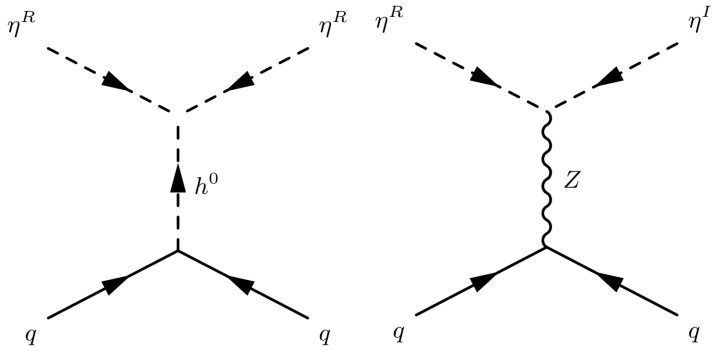

Figure 3.4: Diagrams contributing to the η_R-nuclei elastic scattering at tree level via Higgs exchange on the left and Z boson exchange on the right.

3.2 Analysis of the $\mathbb{Z}_2$ symmetry

One of the main theoretical constrains in the Scotogenic model, is the preservation of the $\mathbb{Z}_2$ symmetry to large scales of energy, in order to keep the dark matter particle stable. For analyze it, we have selected a benchmark point given in table 3.2 that survive all the constrains given in Section 2.4 focus attention on that it is representing the total dark matter abundance contained in the Universe. The analysis is made

Parameter	Value	Units
λ_1	0.259518	-
λ_2	0.000041324	-
λ_3	0.0118591	-
λ_4	-0.0000396669	-
λ_5	-0.0000454048	-
m_η^2	274591	$(\text{GeV})^2$
MN_1	1233.51	(GeV)
MN_2	9970.5	(GeV)
MN_3	12888.2	(GeV)

Table 3.2: Benchmark point that respects all the constraints considered at section 2.4.

using the renormalization groups equations (Appendix B) for the Scotogenic model where we have made the following assumptions

- We have started our analysis at the scale of the mass of the last heavy fermion $M_{N_3} = 12888.2$ GeV running first the RGE until the GUT scale. After that, we have go back in the scale of energy until the mass of the second heavy fermion $M_{N_2} = 9970.5$.
- New heavy fermions N_i, and the parameter m_η are integrated out in their respective scale of energy.
- Light neutrinos masses, their respecting yukawa couplings and standard model yukawa coupling will not present large changes among the evolution for the electroweak scale of energy to the10^{16} GeV that represents the Grand Unification Scale (GUT). Neutrino masses are generated at one loop because of the contribution of the dark sector of the model. Nevertheless, neutrino masses are generated before than this particles were integrated out because they still having contribution to low energy physics as is considered in [223].
- For simplicity, we have not considered the contribution of the evolution of effective field theories as it is considered in [224], due to the evolution of the model among the different scales of energies is not the purpose of this thesis.

We have calculate the evolution of the parameter m_η^2 and studied if it become negative. Their respective RGE is given by

$$\mathcal{D}m_\eta^2 = 6\lambda_2 m_\eta^2 + (4\lambda_3 + 2\lambda_4)m_\phi^2 + m_\eta^2\left[2\text{Tr}(Y^{N\dagger}Y^N) - \frac{3}{2}(g_1^2 + 3g_2^2)\right] - 4\sum_{i=1} M_{N_i}(Y^N Y^{N\dagger})_{ii} \tag{3.1}$$

Figure (3.5) shows the running of the parameter m_η along the different energy scales, from the mass of m_η until 8 TeV. The initial values for the RGEs of each parameter are given by the benchmark point shown in table (3.2) considering the points listed before. We can notice that for out benchmark point the parameter m_η will not become negative in any scale of energy and the $\mathbb{Z}_2$ symmetry is "safe". Seeing the equation 3.1 we can notice that one of the main problems will arise from the mass of the heavy fermions N_i and the values of the new yukawa coupling Y^N due to when they are larger than the other parameters that contribute to the evolution of m_η, the parameter can become negative. This can be controlled considering the value of λ_5 not smaller than 10^{-9} in order to keep the yukawa coupling Y^N smaller enough to do not present problems to the stability of the $\mathbb{Z}_2$ symmetry.

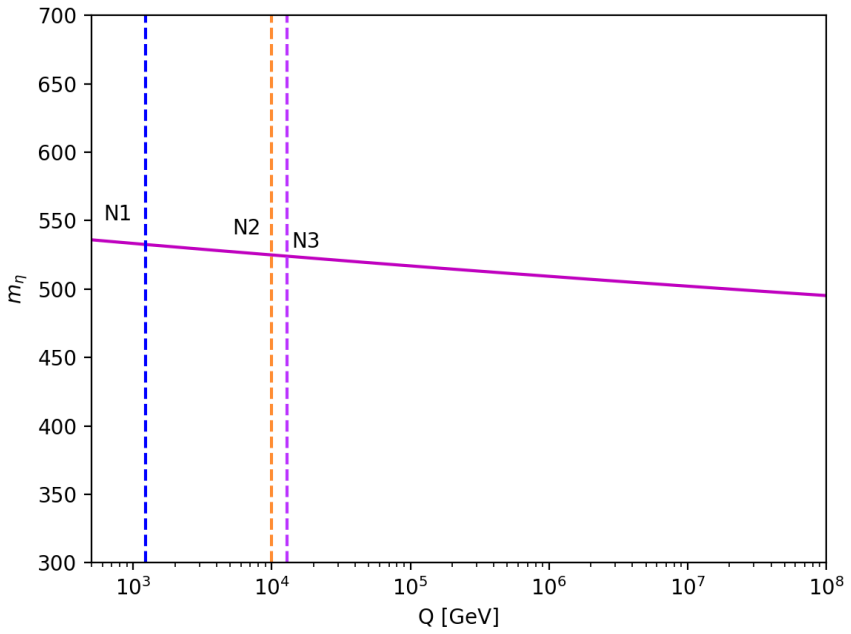

Figure 3.5: Running of the parameter m_η^2 versus the scale of energy Q, represented by the solid magenta line. The dashed lines represent the boundaries for each heavy fermion: N_1 (blue), N_2 (orange) and N_3 (purple) considering the values of the benchmark point given at table 3.2

3.3 Signatures of the Scotogenic model and the Inert Higgs Doublet model at CLIC

In this section we will analyze the signature given by the cross-section $e^+e^- \to \eta^+\eta^-$, which was computed by `Madgraph5` [225] and specializing our code for the CLIC experiment [226]. We will compare that signature in the Inert Higgs Doublet model and the Scotogenic model

The Feynman diagrams displayed below in Figure 3.6 shows the contributions of each model. In the case

of the Scotogenic model the third diagram adds an extra contribution to the final value of the cross section which can be contribute positively or negatively to the final value of the cross section.

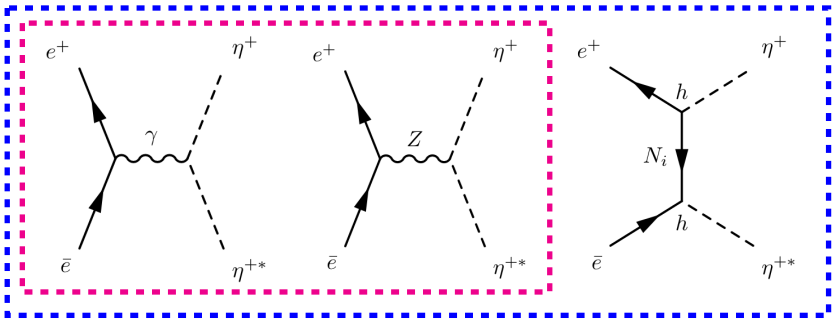

Figure 3.6: Feynman diagrams for Inert Higgs Doublet model (magenta dashed line) and Scotogenic model (blue dashed line).

For the analysis we selected a benchmark point (table (3.2)) that survive all the constrains given in Section 2.4, highlighting the fact to $\mathbb{Z}_2$ symmetry is preserve up to scales close to the 8 TeV. First, we fix the parameters that appear in table (3.2) and we have variate randomly only the values of λ_5 between $10^{-9} - 1$ and the heavy fermion N_1 between $200 - 5000$ GeV. We have studied the contribution of the extra process in the Scotogenic model for the scattering cross section of $e^+e^- \to \eta^+\eta^-$ compared with the cross section value of the same process in the Inert Higgs doublet model.

Figure (3.7) shows the value of the cross section for the signature $e^+e^- \to \eta^+\eta^-$ at luminosity of 2 $[\text{ab}]^{-1}$ at CLIC [227] for the Inert Higgs Doublet model and the Scotogenic model versus the mass of M_{N_1}, considering 2000 points. The blue band represent the cross section value for the Inert Higss Doublet model where we can notice that because of the heavy fermion N_1 is not a particle of the model, its cross section will not depend of it. The colored points represent the different values of the cross section $e^+e^- \to \eta^+\eta^-$ for the simple Scotogenic model. The color bar represent the mass difference between m_{η_R} versus M_{N_1}. We can notice that when the mass difference $M_{N_1} - m_{\eta_R}$ is large, the contribution coming from the extra feynman diagram in Scotogenic model is smaller, and the cross section values of both models are almost the same. The main difference of the cross section value for the model will appear when the mass difference is close to zero. So far, results show that the difference of the value of the cross section can reach less than the 30% considering that the maximum value of center-of-mass energy that CLIC would reach is 3 TeV with a total integrated luminosity of 2 $[ab]^{-1}$ when the mass of N_1 is smaller than m_{η_R}.

The cross section can be calculated analytically in order to study the contribution of the extra Feynman diagram. Using the golden rule given in Appendix C.2, we have

$$\frac{d\sigma}{d\cos\theta} = \frac{|\mathcal{M}|^2}{32\pi(E_e)^2}\frac{|\vec{p}_3|}{|\vec{p}_1|}. \tag{3.2}$$

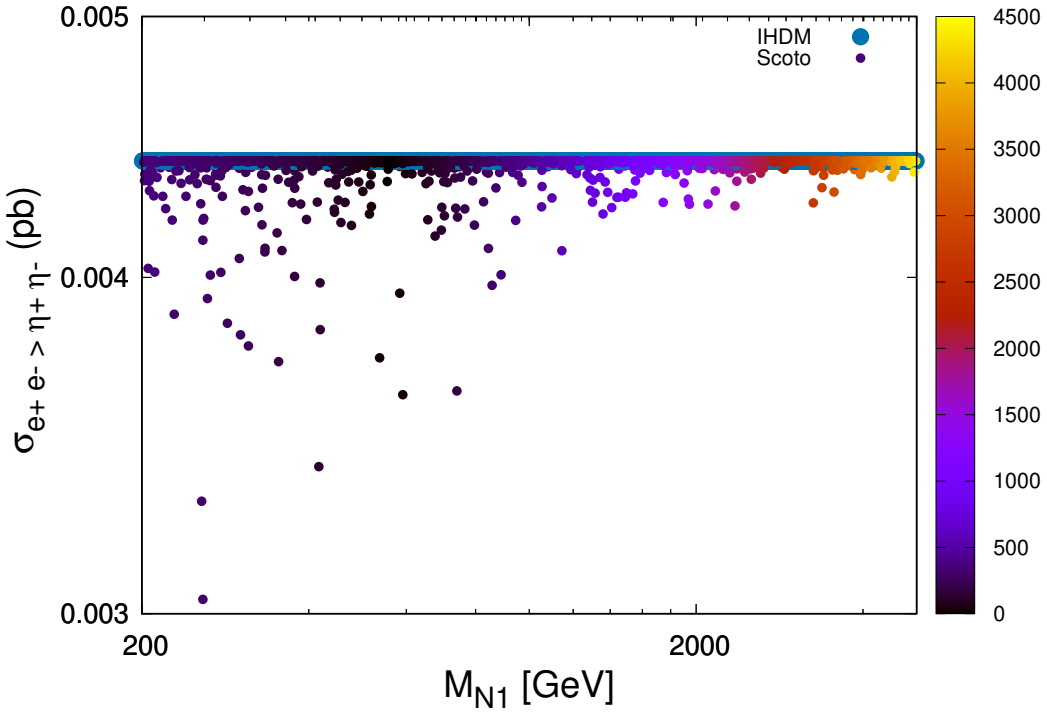

Figure 3.7: Cross section values for the two models: blue points are the results obtained for the IHDM model while blue colored points are the values for the cross section of the Scotogenic model. Color bar represents the mass difference between N_1 and η_R.

where the probability of amplitude for the Scotogenic model is

$$|\mathcal{M}|^2 = \mathcal{M}_{11} + \mathcal{M}_{22} + \mathcal{M}_{33} - \mathcal{M}_{44} + \mathcal{M}_{55}. \tag{3.3}$$

where

$$\mathcal{M}_{11} = \frac{e^2}{4E_e^4}\left[4p_3^2(E_e^2+p_1^2+m_e^2) - 8p_3^2p_1^2\cos^2\theta\right] \tag{3.4}$$

$$\mathcal{M}_{22} = \frac{g^4\cos2\theta_w}{4\cos\theta_w(4E_e^2-m_z^2)^4}\left(4p_3^2(E_e^2+p_1^2+m_e^2) - 8p_3^2p_1^2\cos^2\theta\right)\left[4\left(2\sin\theta_w - \frac{1}{2}\right)^2 + 1\right] \tag{3.5}$$

$$\mathcal{M}_{33} = \frac{2e^2g^2}{E_e}\frac{1}{\cos\theta_w}\frac{1}{4E_e^2-m_z^2}\left[4p_3^2(E_e^2+p_1^2+m_e^2) - 8p_3^2p_1^2\cos^2\theta\right] \tag{3.6}$$

$$\begin{aligned}\mathcal{M}_{44} &= \frac{4Y^{N^2}e^2}{E_e^2((E_{\eta^+}-E_e)^2+p_3^2-4p_3p_1\cos\theta+2p_1^2-M_N^2)}\left[2p_3p_1\cos\theta(2p_3p_1\cos\theta-2p_1^2)\right. \\ &- \left.(E_e^2+p_1^2)(2p_3p_1\cos\theta-2p_3^2)+4m_eM_Np_3p_1\cos\theta\right]\end{aligned} \tag{3.7}$$

$$\begin{aligned}\mathcal{M}_{55} &= \frac{2gY^{N^2}\cos(2\theta_w)(2\sin\theta_w-1/2)}{2\cos\theta_w((E_{\eta^2}-E_e)^2+p_3^2-4p_3p_1\cos\theta+2p_1^2-M_N^2)}\frac{1}{4(E_e^2-m_z^2)} \\ &\times \left[2p_3p_1\cos\theta(2p_1^2-2p_1p_3\cos\theta)-(E_e^2+p_1^2)(2p_3p_1\cos\theta-2p_3^2)+4M_Nm_ep_3p_1\cos\theta\right].\end{aligned} \tag{3.8}$$

We have considered $P_1 = (E_e, 0, 0, p_1)$, $P_2 = (E_e, 0, 0, -p_1)$, $P_3 = (E_{\eta^+}, p_3\sin\theta, 0, \mathrm{p_3}\cos\theta)$ and $P_4 = (E_{\eta^+}, -p_3\sin\theta, 0, -\mathrm{p_3}\cos\theta)$ where $E_e = \sqrt{p_1^2 + m_e^2}$ and $E_{\eta^+} = \sqrt{p_3^2 + {m_{\eta^+}}^2}$. A more detailed calculus is shown in Appendix. C.2.

We can notice that the contribution of the extra particles in equation 3.7 and 3.7 can arise to lower the final value of equation 3.3 in comparison with the value of the total amplitude for the IHDM. This is an explanation of why all the numerical results of the cross section in Scotogenic model are smaller than the results for the IHDM as we see in figure 3.7.

4

Dark matter searches at the STSM

"Do you know, I always thought unicorns were fabulous monsters, too? I never saw one alive before!"
"Well, now that we have seen each other",said the unicorn, "if you'll believe in me, I'll believe in you.

Lewis Carroll

Alice's Adventures in Wonderland and Through the Looking Glass

In this chapter we collect the results of our analysis of dark matter in the Singlet + Triplet Scotogenic Model. As already commented before, this model can harbor either fermionic or bosonic WIMP dark matter. Here we will assume the $\mathbb{Z}_2$-odd scalar η_R to be the dark matter candidate and investigate its phenomenology in the freeze-out scenario. For a fermionic dark matter candidate χ^0 [187], detailed studies of it phenomenology have been presented in Ref. [190, 191]. The case of scalar dark matter has common features with those of the simple scotogenic constructions [185] as well as the Inert Higgs Doublet Model [228, 229, 230] that were explained before. We will continue with the analysis of one interested benchmark point at colliders, confronting the new run of the LHC.

4.1 Numerical analysis

We now confront the model with current (and future) observations associated both with the primordial cosmological abundance of dark matter, as well as various pheomenological constraints, including the experimental prospects for direct and indirect dark matter detection.

4.1.1 Parameter scan

We have developed a numerical code using Python, to perform a scan varying randomly the main free parameters which characterize the model. This code is connected to some public computer tools used in particle physics in order to examine the constraints on the model parameters and also quantify the expected sensitivities of future experiments. In particular, our Singlet + Triplet Scotogenic Model is first implemented in `SARAH 4.9.1` [219, 220], which calculates all vertices, mass matrices, tadpole equations, one-loop corrections for tadpoles and self-energies. The physical particle spectrum and low-energy observables are computed with `SPheno 4.0.3` [216, 217] and `FlavorKit` [218]. In order to perform the dark matter analysis, we use `Micromegas 5.0.2` [221] to compute the thermal component to the dark matter relic abundance as well as the dark matter-nucleon scattering cross sections. For the calculation of the cross sections relevant for the collider analysis, we have used `MadGraph5` [225], importing the UFO files generated with `SARAH 4.9.1`. Our numerical scan was performed with 60000 points, varying the input parameters as given in table 4.1. In particular, in the ranges of variation for the values of m_η^2 and $|\lambda_5|$, the lower limits considered were 100 GeV and 10^{-5} respectively, to ensure good behaviour for the $\mathbb{Z}_2$ symmetry [188].

This model has in principle three potentially viable dark matter candidates: η_R, η_I or χ_0. In the following we will fix $\lambda_5 < 0$ so as to ensure η_R to be the dark matter candidate. This choice is made for definiteness, having in mind that the opposite case with $\lambda_5 > 0$ and η_I as the lightest neutral scalar would also be potentially viable. Notice that the parameters that are not shown in the table are calculated from the ones displayed. For example, m_ϕ^2 and m_Ω^2 are obtained from the tadpole equations 2.31 and $Y^\nu_{\alpha\beta}$ is calculated via Eq. 2.48. Note that the smallness of neutrino masses does not preclude these Yukawas from being sizeable, since the neutrino masses are controlled by λ_5 and they are further suppressed by their radiative origin.

Parameter	Range
M_N	$[5 \cdot 10^3, 10^4]$ (GeV)
M_Σ	$[5 \cdot 10^3, 10^4]$ (GeV)
m_η^2	$[100^2, 5000^2]$ (GeV^2)
$\mu_{1,2}$	$[10^{-8}, 5 \cdot 10^3]$ (GeV)
v_Ω	$[10^{-5}, 5]$ (GeV)
$\lvert\lambda_i\rvert$, $i = 1...4$	$[10^{-8}, 1]$
$\lvert\lambda_5\rvert$	$[10^{-5}, 1]$
$\lvert\lambda_{1,2}^\Omega\rvert$	$[10^{-8}, 1]$
$\lvert\lambda_\eta^\Omega\rvert$	$[10^{-8}, 1]$
$\lvert Y_\Omega\rvert$	$[10^{-8}, 1]$

Table 4.1: Ranges of variation of the input parameters used in the numerical scan.

4.2 Relic density

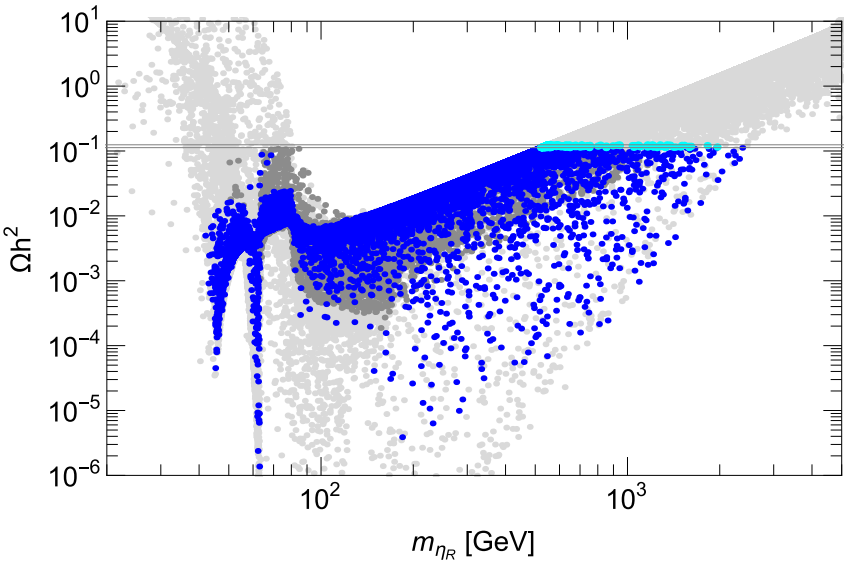

Figure 4.1: Relic abundance $\Omega_{\eta_R} h^2$ as a function of the η_R mass. Blue points denote solutions with viable relic density, although leading to underabundant dark matter. Cyan points fall within the 3σ C.L. cold dark matter measurement by the Planck collaboration [19, 20]. Grey dots are excluded by at least one of the bounds in Sec. 2.4. Dark grey points are in conflict with the current limit on WIMP-nucleon SI elastic scattering cross section set by XENON1T [21].

We show in Fig. 4.1 the expected dark matter relic abundance as a function of the mass of the scalar dark matter candidate η_R. The narrow black band depicts the 3σ range for cold dark matter derived by the Planck satellite data [19, 20]. Only for solutions falling exactly in this band (cyan points) the totality of dark matter can be explained by η_R. Blue points refer to solutions where η_R would be subdominant, and another dark matter candidate would be required. Grey points are instead excluded by any of the

constraints discussed in Sec. 2.4, mainly by the Planck constraint itself. Dark grey points are solutions in conflict with the current limit on WIMP-nucleon SI elastic scattering cross section set by XENON1T [21]. The features appearing in the plot can be explained by looking in detail into the η_R annihilation channels. The first dip on the left depicts the Z-pole, that is where $m_{\eta_R} \sim M_Z/2$ and the annihilation via s-channel Z exchange becomes relevant. Similarly, the second depletion of the relic density around $m_{\eta_R} \sim 60$ GeV corresponds to efficient annihilations via s-channel Higgs exchange. Notice that it is likely for solutions in this dip to be in conflict with current collider limits on BR($h^0 \to$ inv). The latter depletion is more efficient than the Z-mediated one, which is momentum suppressed. For heavier η_R masses, quartic interactions with gauge bosons become effective and, when kinematically allowed, also two-top final states. Annihilations of η_R into W^+W^- via quartic couplings are particular important at $m_{\eta_R} \gtrsim 80$ GeV thus explaining the third drop in the relic abundance. Finally, in the range $m_{\eta_R} \gtrsim 120$ GeV η_R can annihilate also into two Higgs bosons. At even heavier m_{η_R} the annihilation cross section drops as $\sim \frac{1}{m^2_{\eta_R}}$ and the relic density increases proportionally. Eventually, heavy η_R mainly annihilate into W^+W^-, h^0h^0, HH. We collect all the Feynman diagrams contributing to η_R annihilations and co-annihilations in Appendix D.2. We may also notice that the relic abundance constraint does not put any bound on the absolute value of the $|\lambda_5|$ parameter. On the other hand, cohannihilations with η_I and $\eta^\pm$ may occur in all regions of the parameter space with the effect of lowering the relic abundance.

We show in Fig. 4.2 the most relevant branching ratios (at tree level) for the annihilation cross section of η_R into SM final states versus the mass of η_R, from our numerical scan. Different kinematical regimes are visible from this figure: below M_W, η_R annihilates predominantly into $b\bar{b}$, gluons or $\tau^+\tau^-$; when the quartic coupling with W becomes kinematically accessible, η_R annihilates mainly into W^+W^-. Similarly, annihilations into h^0h^0, HH and Z^0Z^0 become relevant as soon as kinematically open.

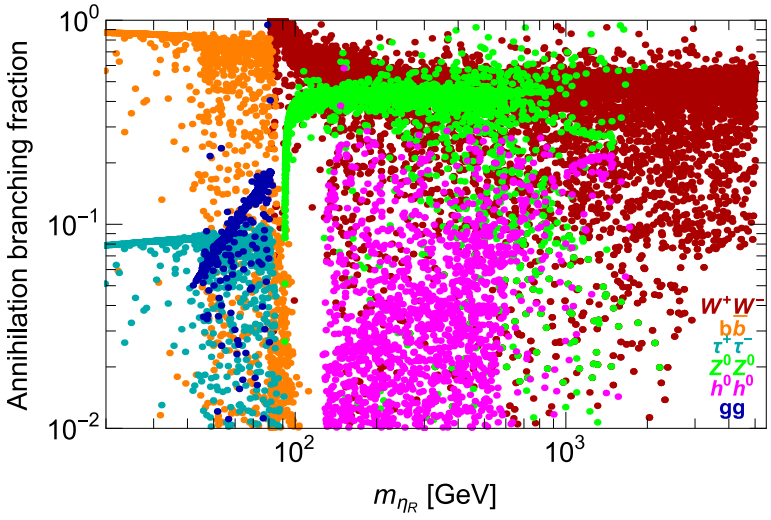

Figure 4.2: Main branching fractions of the annihilation cross section of η_R into SM final states versus the mass of η_R. Orange points refer to annihilation into $b\bar{b}$, dark cyan to $\tau^+\tau^-$, blue to gluons, dark red to W^+W^-, green to Z^0Z^0 and magenta to h^0h^0.

4.3 Direct detection

Let us discuss now the η_R direct detection prospects. The tree-level spin-independent η_R-nucleon interaction cross section is mediated through the Higgs and the Z portals. The relevant Feynman diagrams at tree level for this process are the same than in figure (3.4). Since the η doublet has nonzero hypercharge, the η_R - nucleon interaction through the Z boson would in general exceed the current constraints from direct detection experiments. Nevertheless, in most of the solutions, λ_5 induces a mass splitting between the CP-odd partner η_I and η_R such that the interaction through the Z boson is kinematically forbidden, or leads to inelastic scattering. The η_R-nucleon interaction via the Higgs is therefore dominant in most of the parameter space. As a consequence, the coupling between η_R and the Higgs boson (which depends on the sum $\lambda_3 + \lambda_4 + \lambda_5$ and on v_Ω, μ_2 and λ_η^Ω) turns out to be the relevant quantity controlling both this cross section and the signals at LHC that we will discuss in section 4.5. We show in Fig. 4.3 the spin-independent η_R-nucleon elastic scattering cross section weighted by $\xi = \frac{\Omega_{\eta_R}}{\Omega_{\text{Planck}}}$ versus the η_R mass. The color code of displayed points is the same as in Fig. 4.1. The dark green plain line denotes the most recent upper bound from XENON1T [21]. Although we only show the most stringent up-to-date limit from XENON1T, we note that other leading liquid xenon experiments such as LUX [9] and PandaX-II [85] can also probe the spin-independent dark matter-nucleon elastic scattering cross section for dark matter heavier than ~ 50 GeV. On the other hand, DarkSide-50 [87] and DEAP-3600 [231] are less competitive for medium and high-mass WIMPs, because of their higher thresholds and lower exposures. Finally, we also depict as for comparison the lower limit (dashed orange line) corresponding to the "neutrino floor" from coherent elastic neutrino-nucleus scattering (CEνNS) [15] and the projected sensitivity for LUX-ZEPLIN (LZ, green dot-dashed) [22]. Most of the allowed solutions with a relic abundance within the 3σ C.L. cold dark matter measurement by the Planck collaboration [19, 20] lie in a tight vertical region around $m_{\eta_R} \sim 500 - 600$ GeV. Lighter η_R lead to viable dark matter, although under-abundant, hence it would then require the existence of an additional dark matter candidate.

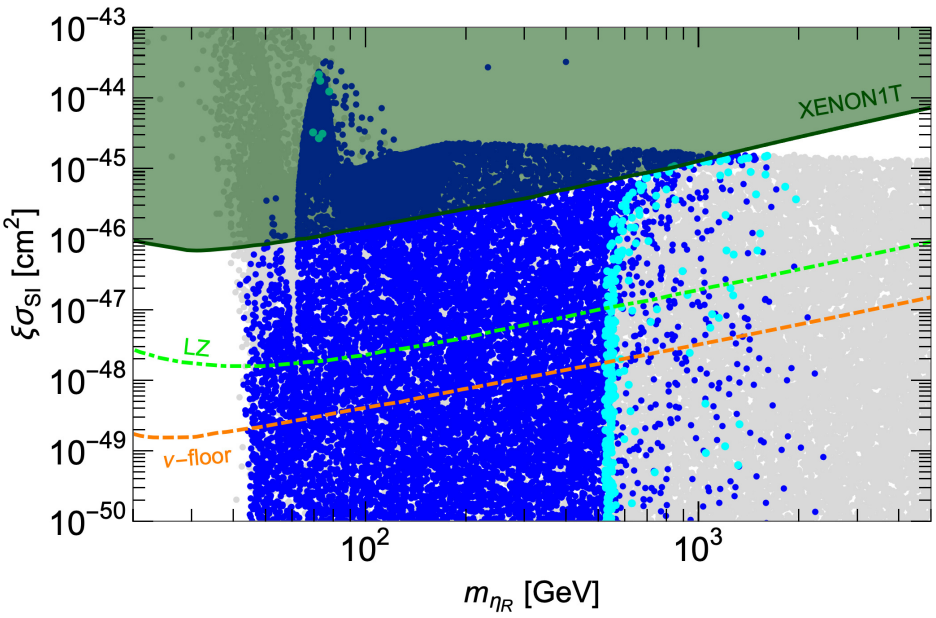

Figure 4.3: Spin-independent η_R-nucleon elastic scattering cross section versus the η_R mass. Colour code as in Fig 4.1. The dark green line denotes the most recent upper bound from XENON1T [21]. The dashed orange line depicts the lower limit corresponding to the "neutrino floor" from coherent elastic neutrino-nucleus scattering (CEνNS) [15], while the green dot-dashed one stands for the projected sensitivity for LZ [22].

4.4 Indirect detection

If η_R annihilates into SM products with a cross section near the thermal relic benchmark value, it may be detected indirectly. Among its annihilation products, gamma-rays are probably the best messengers since they proceed almost unaffected during their propagation, thus carrying both spectral and spatial information. First we consider prospects of detecting gamma-rays from η_R annihilations by considering the continuum spectrum up to the η_R mass which originates from decays of the annihilation products. We consider annihilations into $b\bar{b}$, $\tau^+\tau^-$ and W^+W^- to compare with current limits set by the Fermi Large Area Telescope (LAT) satellite [23] and HESS telescope [24]. We show in Fig. 4.4 the results of our numerical scan of the annihilation cross section (weighted by ξ^2 and by the correspondent branching ratio) versus the η_R mass, for η_R annihilating into $b\bar{b}$ (orange points), $\tau^+\tau^-$ (dark cyan) and W^+W^- (dark red). Grey points are excluded by any of the constraints listed in section 2.4. Points in light red are solutions with relic abundance falling exactly within the 3σ band measured by Planck. In the same figure we also show the 95% C.L. upper limits currently set by the Fermi-LAT with gamma-ray observations of Milky Way dwarf spheroidal satellite galaxies (dSphs) based on 6 years of data processed with the Pass 8 event-level analysis [23] (plain lines assuming annihilation into $b\bar{b}$ (orange), $\tau^+\tau^-$ (dark cyan) and W^+W^- (dark red)). Moreover we show as a red dot-dashed curve the current upper limit obtained by H.E.S.S. using Galactic Center (GC) gamma-ray data accumulated over 10 years [24], assuming a W^+W^- channel and an Einasto dark matter density profile. Finally, we also depict sensitivity projections for Fermi-LAT

from a stacked analysis of 60 dSphs and 15 years of data, in the $b\bar{b}$ channel [25] (dashed orange) and for CTA, for the Milky way galactic halo target, W^+W^- channel and an Einasto dark matter density profile [26]. Although current limits lie a couple of orders of magnitude above the predicted signals in this model, future data from Fermi-LAT and CTA offer promising prospects, eventually allowing one to test part of the parameter space both in the low ($\sim$ 70 GeV) and in the high ($\gtrsim$ 500 GeV) mass regions.
Note that when the η_R is non-relativistic, as is the case of annihilations occurring at the current epoch, its annihilation cross section and hence its indirect detection flux can be affected by a non-perturbative correction, the Sommerfeld enhancement [232, 233, 234, 235, 236]. This occurs when $m_{\eta_R} \gg M_W(M_Z)$ and η_R is almost degenerate in mass with $\eta^{\pm}(\eta_I)$. The multiple exchange of W (Z) bosons would induce a long range attractive force, thus leading to an enhancement of the annihilation cross section at low dark matter velocities, compared to its tree-level value. This process might improve the detection prospects of the η_R annihilation via gamma-rays for some parameter choices.

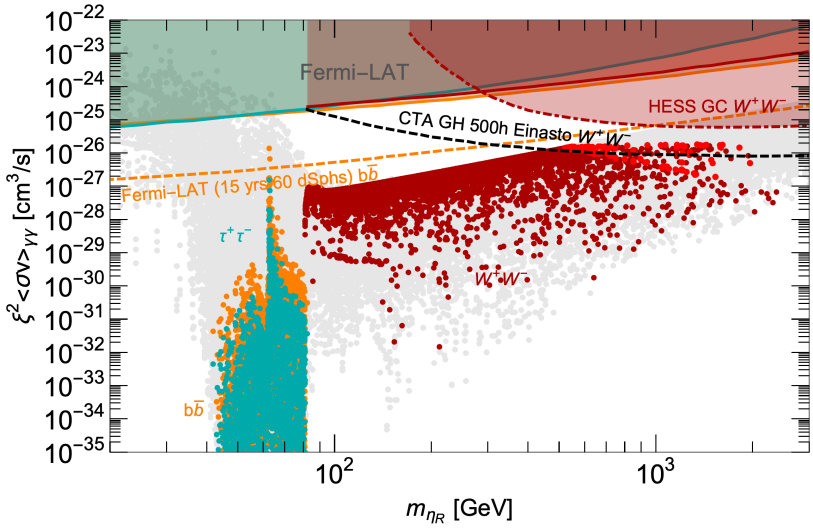

Figure 4.4: Predicted η_R annihilation cross section into gamma-rays – weighted by the relative abundance – for annihilations to $b\bar{b}$ (orange), $\tau^+\tau^-$ (dark cyan) and W^+W^- (dark and light red) final states. The orange, dark cyan and dark red plain lines refer to the corresponding 95% C.L. upper limits currently set by the Fermi-LAT with gamma-ray observations of dSphs [23]. The dark red dot-dashed curve is the current upper limit obtained by H.E.S.S. using GC data [24]. We also compare with sensitivity projections for Fermi-LAT ($b\bar{b}$, 60 dSphs and 15 years of data) [25] and for CTA (GC, W^+W^-) [26]. See text for more details.

Besides gamma-rays, charged cosmic rays can be used to probe η_R as a dark matter candidate. The positron fraction measured by PAMELA [237, 238] and more recently by AMS-02 [239, 240], allows us to place constraints on annihilating WIMPs, which are particularly stringent in the case of annihilations to the first two generations of charged leptons. In our scenario, light η_R annihilate mainly to $\tau^+\tau^-$, as can be seen from Fig. 4.2. As a result bounds from cosmic positrons are less relevant than those from gamma-rays. In addition to cosmic-ray positrons, AMS-02 has also provided a high-precision measurement of the cosmic-ray antiproton spectrum [241]. These can be translated into upper limits on hadronic dark matter annihilation, which can be a factor of few stronger than those from gamma-ray observations of

dSphs [242, 243]. Since these results rely on a careful treatment of systematic uncertainties, namely the antiproton production cross-section, and the modelling of the effect of solar modulation we decided not to include them here and leave it for a dedicated work. Similarly, searches for anti-deuterium or anti-helium events could potentially provide a powerful probe of η_R annihilations [244, 245, 246, 247], although also affected by substantial uncertainties.

4.5 Scalar dark matter signatures at the LHC

In this section we confront our scalar dark matter candidate with the latest data from particle colliders, in particular from the LHC run at $\sqrt{s} = 13$ TeV. As in any model with a dark matter candidate, the generic signature to be searched for is missing energy ($\not{E}_T$), measured from the total transverse momentum recoil of the visible particles in the event (see for instance [248, 249]).

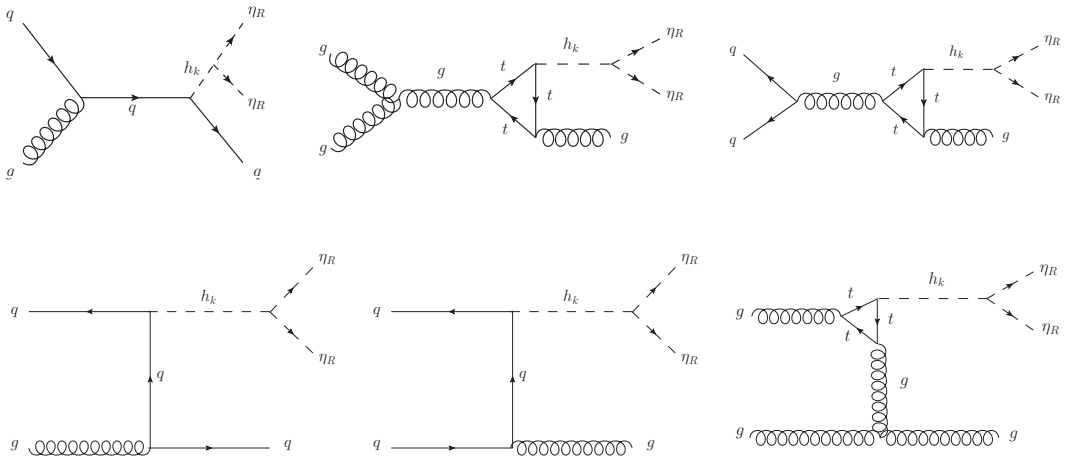

Figure 4.5: Relevant Feynman diagrams for mono-jet production through $\eta_R\eta_R + j$ at the LHC; here $h_k \equiv h^0$ or H.

In the Triplet + Singlet Scotogenic Model typical signatures are $\not{E}_T + X$, where X can be one or two jets [27, 250], two leptons [251] or one photon [252]. Although all of them are in principle interesting, we have checked numerically that in our scenario the most promising one is $\not{E}_T+$ jet (mono-jet). In the following we will focus on mono-jet final states, arising from $pp \to \eta_R\eta_R + g$ and $pp \to \eta_R\eta_R + q$ processes. Here ones looks for events with one high-p_T jet (higher than $100 - 200$ GeV in the central region of the detector, with pseudorapidity $|\eta| < 2.4$) and $\not{E}_T$ above roughly 200 GeV in the 13 TeV analyses for the ATLAS and CMS detectors [27, 253]. At leading order, the relevant Higgs-mediated Feynman diagrams for mono-jet events are shown in Fig. 4.5.

In all cases, the dark matter is produced via the decay of a neutral scalar (h^0 or H), produced from its interaction with quarks, or through its effective coupling to gluons. The latter involves a top quark loop and enters in gluon-gluon fusion (ggF) processes. An important point is that in ggF processes only the SM-like Higgs doublet couples with fermions. Indeed, since H is mainly a triplet, its coupling with quarks is suppressed. The interaction vertex between η_R and h_k is given in Appendix D.3. Note that if

the mass difference between η_I and η_R is small, η_I should also contribute to the invisible final states. In this case, η_I would subsequently decay to η_R plus soft fermions or jets which are not energetic enough to be detected. Besides Higgs mediation, the mono-jet signal can proceed also via Z-mediation. Therefore we also include the contributions shown in Fig. 4.6, which are described as $pp \to \eta_R\eta_I + g$ and $pp \to \eta_R\eta_I + q$ processes. Finally, we must mention that in this same scenario of small mass differences, a pair of η_I can also be produced.

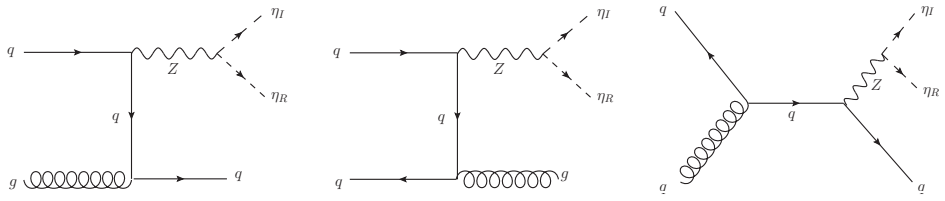

Figure 4.6: Feynman diagrams illustrating Z-mediated production of $\eta_R\eta_I + j$ at the LHC.

4.5.1 Benchmark Points

The constraints previously described in Section 2.4 restrict the parameter space allowed by a vast array of experimental probes, among which are the relic density, direct detection and indirect detection analyses. Motivated by these preliminary studies, we now investigate using the `CheckMATE 2` collaboration tools [254, 255, 256, 257, 258] whether the solutions that satisfy all experimental limits in section 2.4 could lead to detectable dark matter mono-jet signals at LHC 13 TeV. This code allows us to determine whether or not a given parameter configuration of our model is excluded at 95% C.L. Indeed, for each signal region, `CheckMATE 2` computes the expected number of signal events S after cuts, and directly compare it to the 95% C.L. upper limit S^{95}_{exp}, given a signal error ΔS. The most relevant analysis for our study is Ref. [27].

In this way, we identify two interesting benchmark points which survive the entire set of constraints described in Section 2.4 and shown in Table 4.2. Values of the relevant parameters and the corresponding scalar spectrum are summarised. We also show in this table the value of observables obtained in Section 2.4 for each benchmark. The main difference between the two benchmark points is the value of H mass, which is governed by μ_2 and v_Ω. However, because this heavy scalar is mainly triplet, its coupling with quarks in the ggF processes is suppressed, so that a significant change in its mass is not expected to lead to a large variation in the magnitude of the cross sections.

4.5.2 Mono-jet signatures at the LHC $\sqrt{s} = 13$ TeV

We display in Tab. 4.3 the `CheckMATE 2` results for the evaluation in the $\not{E}_T$+jet channel (corresponding to an integrated luminosity of 36.1fb^{-1} in the $\sqrt{s} = 13$ TeV analysis) for the two benchmark points of Tab 4.2. For this study, the cross sections shown in Tab. 4.3 correspond to both contributions to the final state studied: Z boson (Fig. 4.6) and Higgs-mediated processes (Fig. 4.5), respectively.

Parameters	Benchmark 1	Benchmark 2	Units
λ_3	3.64×10^{-5}	-1.64×10^{-5}	-
λ_4	7.02×10^{-7}	-3.29×10^{-7}	-
λ_5	-1.8×10^{-2}	-1.45×10^{-2}	-
λ_η^Ω	-1.32×10^{-5}	-7.11×10^{-6}	
μ_2	-4.57×10^{-8}	-1.59×10^{-1}	[GeV]
v_Ω	2.43×10^{-4}	9.21×10^{-1}	[GeV]
m_η^2	3678.17	2851.39	$[\text{GeV}]^2$
Scalar masses			
m_{η_R}	55.92	49.09	[GeV]
m_{η_I}	65.04	57.38	[GeV]
m_{h^0}	124.68	125.54	[GeV]
m_H	425.9	834.45	[GeV]
Constraints			
Ωh^2	0.0107	0.0129	-
$\text{BR}(h^0 \to inv.)$	0.155489	0.12939	-
$\text{BR}(\mu \to e\gamma)$	7.33×10^{-29}	8.55×10^{-32}	-
$\text{BR}(\mu \to eee)$	3.75×10^{-30}	1.01×10^{-30}	-
$\text{CR}(\mu^-, Au \to e^-, Au)$	3.88×10^{-29}	1.40×10^{-29}	-
$\text{BR}(h^0 \to \gamma\gamma)$	0.00226748	0.00212008	-
Δa_μ	2.18×10^{-14}	2.15×10^{-14}	-
σ_{SI}	5.953×10^{-10}	4.862×10^{-10}	cm^2

Table 4.2: Benchmark points which survive the entire set of constraints described in Section 2.4 and corresponding parameters relevant to the calculation of diagrams in $\not{E}_T$+jet final states.

Quantity	Benchmark 1	Benchmark 2
$\sigma \pm d\sigma$ [fb]	787.791	1074.62
$S \pm dS$	163.241 ± 6.814	421.3 ± 12.784
r	0.220	0.263

Table 4.3: Results obtained with `CheckMATE 2` based on the `atlas_conf_2017_060` [27] analysis by the ATLAS collaboration, for LHC data at $\sqrt{s} = 13$ [TeV].

The main result of Tab. 4.3 is the value of the parameter r

$$r \equiv \frac{S - 1.96\Delta S}{S_{exp}^{95}} \tag{4.1}$$

calculated by `CheckMATE 2`[1], which translates into a significant number of signal events after the cuts, S.

[1] According to algorithm definitions and taking into account experimental errors, a point in parameter space is considered excluded if the ratio $r \geq 1.5$. If $r \leq 0.67$, the point is classified as compatible with the experimental results and is kept. Points with $0.67 < r < 1.5$ are regarded as "potentially excluded" in view of the systematic

These specific cuts are implemented by the ATLAS analysis in order to map out the associated regions of consistent parameter choices, and will be described later.

Our dark matter candidate η_R with mass around $\sim 50-60$ [GeV] and chosen to satisfy all theoretical and experimental constraints of Sec. 2.4 would lead to a signature in the $\not{E}_T$+jet channel in the ATLAS experiment. For that we require, for both benchmark points, that the leading jet has $p_T > 250$ [GeV] and $|\eta| < 2.4$, separation in the azimuthal plane of $\Delta\phi(\text{jet}, p_T^{miss}) > 0.4$ between the missing transverse momentum direction and each selected jet. The difference between our benchmarks are the $\not{E}_T$ thresholds. While for Benchmark 2 a $\not{E}_T$ minimum of 500 [GeV] is required, in the other case we take $\not{E}_T > 600$ [GeV].

For larger η_R masses we investigate the behaviour of the cross sections at $\sqrt{s} = 13$ TeV and the projected signal events at $\sqrt{s} = 14$ TeV. We assume the coupling $|\lambda_{345}|$ to lie in the range $[0.02, 0.9]$ and we fix the other parameters according to Benchmark 1 in Tab. 4.2. We analyse $\eta_R\eta_R + j$ and $\eta_R\eta_I + j$ separately because the rate of these processes depends on different parameters and we want to analyze their contributions to the total cross section separately.

In Fig. 4.7 we present the production cross section for $\not{E}_T$+ jet process at LHC $\sqrt{s} = 13$ (14) TeV. Using `Madgraph5` [225] we simulate events with an initial cut of $p_T^{jet} > 100$ [GeV], according to the latest analyses in mono-jet searches [260, 261]. Since the relevant processes leading to these events are mediated by mainly the SM Higgs (left panel) and Z boson (right panel), one has the characteristic peaks at $m_{\eta_R} \sim m_{h^0}/2$ and at $m_{\eta_R} \sim m_Z/2$ respectively, providing larger cross sections in these mass ranges. Therefore, the Higgs boson mediated processes are dominant up to $m_{\eta_R} \sim 60$ [GeV] and also contribute in the range $\sim [700-1400]$ fb (13 TeV). In addition, Z-mediated processes complements the search for $pp \to \eta_R\eta_R$+ jet process at the LHC. For this mass range, the cross sections are $\sim [190-80]$ fb while, for dark matter masses between $[65-200]$ [GeV], we have $\sim [70-5]$ fb, providing a sizeable contribution to the total mono-jet cross section, which could be within LHC sensitivity. At $\sqrt{s} = 14$ TeV the cross section increases by a few fb. These results agree with expectations of other models, such as the Inert Higgs Doublet Model, whose contributions to this signal are very similar [260]. In summary, one sees that there are good prospects for probing the mono-jet signal at the LHC for dark matter masses up to ~ 60 [GeV].

There are regions of parameters in which η_I and η_R are relatively close in mass, as shown in Figure 4.8. This as required for model consistency, as the mass difference between these particles is intimately connected with the smallness of neutrino mass as generated in the scotogenic picture. This requires the violation of lepton number through the value of λ_5, as seen by Eqs. 2.37 and 2.38. Indeed, if $m_{\eta_R} - m_{\eta_I}$ is small we can obtain neutrino mass square differences, as needed to account for neutrino oscillation data [262]. Moreover, the particles produced from the decay $\eta_I \to \eta_R$+X are not energetic enough to have the trajectories reconstructed by the detector (soft particles), leading to our $\not{E}_T$+ jet final state signal.

As already commented in previous sections, as a result of its small coupling with quarks, the heavy neutral scalar H does not influence significantly our signal. As shown in Ref. [189], the production cross

and theoretical errors. For more details see [259].

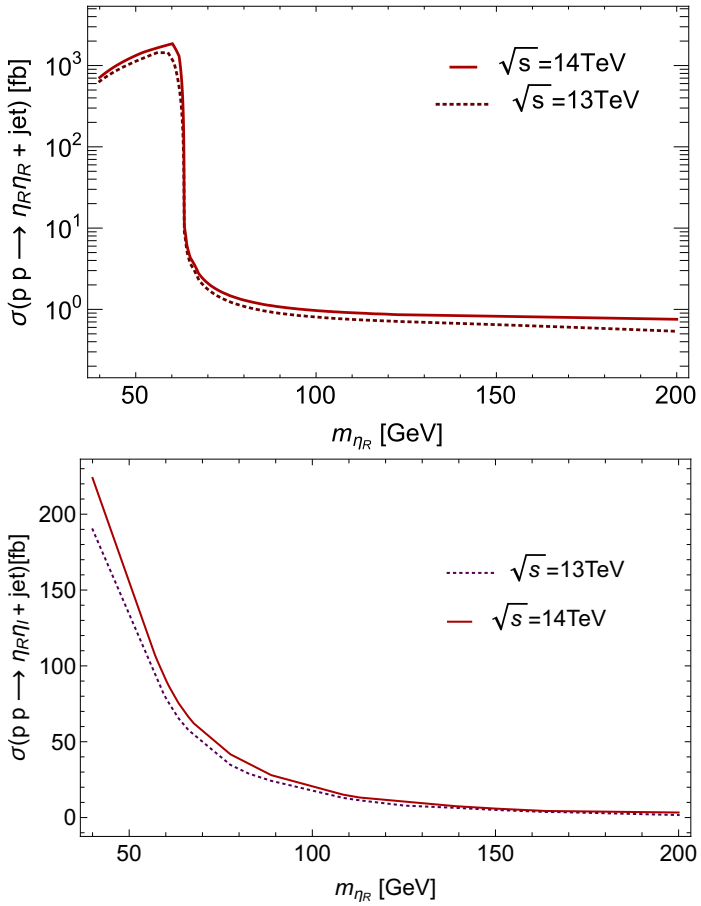

Figure 4.7: Cross sections of mono-jet signals at LHC $\sqrt{s} = 13$ (14) TeV. The left panel shows the Higgs boson mediated events from $pp \to \eta_R\eta_R +$ jet. The maximum value of the cross section is $\sim 1400(1800)$ fb for $\sqrt{s} = 13$ (14) TeV respectively. The right panel is the Z-mediated process, $pp \to \eta_R\eta_I +$ jet, with peak contribution ~ 190 (220) fb.

section of H at the LHC is 3 to 5 orders of magnitude smaller than the production of the SM Higgs boson, independent of the center-of-mass energy. Hence our results for the scalar dark matter jet + missing energy final states within the Singlet + Triplet Scotogenic Model should also hold within the simple Scotogenic scenario of [185].

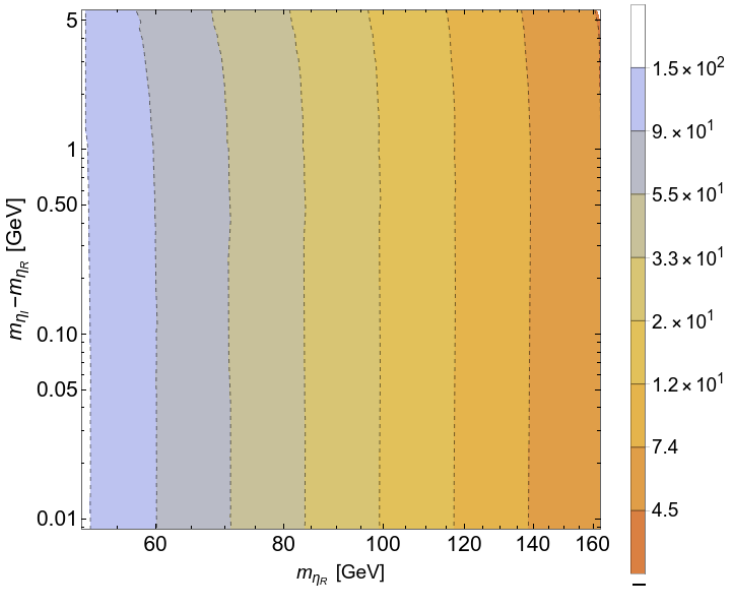

Figure 4.8: Mass difference $m_{\eta_I} - m_{\eta_R}$ as a function of m_{η_R} in mono-jet events mediated by the Z boson, $pp \to \eta_R \eta_I +$ jet. The color shades represent values of the cross section in fb.

5

Summary and conclusions

The Inert Higgs Doublet Model, the simple Scotogenic Model and the Singlet + Triplet Model are extensions of the Standard Model, modifying the Higgs sector and in the case of the last two, the fermionic sector. The models include a $\mathbb{Z}_2$ symmetry which keeps stable the new neutral particles present in the models and brings a particle candidate to dark matter able to form the $\sim 85\%$ of matter of the Universe. Further, both Scotogenic Models introduce a mechanism to explain how neutrinos get a tiny mass consistent with the current experiments. Here, dark matter emerges naturally as the mediator of neutrino mass generation and the $\mathbb{Z}_2$ symmetry is responsible for the radiative origin of neutrino masses.

In the first part of our work we studied the main resemblances and contrasts between the Inert Higgs Doublet Model and the simple Scotogenic Model. We have implemented some constraints on the scalar potential in order to keep both models out from potential destabilization at tree level and at 1 loop. Although in the Scotogenic Model there are two possible dark matter candidates that can be considered, i.e. scalar or fermionic dark matter, we focus in the lightest neutral scalar as the dark matter particle. Even if a single particle of dark matter is not necessary to be in agreement with cosmological constraints, the study of the dark matter phenomenology focus on the possibility that in both models there are parameter regions where the results can explain the total dark matter abundance that exists in the Universe. These results are consistent with all the theoretical and experimental constraints imposed. We investigated the observable given by the cross section for $e^+e^- \to \eta^+\eta^-$ under the light of the Inert Higgs Doublet Model and the Scotogenic Model at CLIC, drawing attention to the stability of the dark matter given by the $\mathbb{Z}_2$ in the benchmark point chosen. We examined that the extra contribution presented in the Feynman diagrams of the Scotogenic Model contribute negatively to the final value of the cross section studied. The

main difference of the cross section in the different models arise in the mass splitting between N_1 and η_R. When the splitting is large enough, the cross section values are practically the same. If the mass splitting is tiny, the extra contribution in the Scotogenic Model gives a numerical value for the cross section in the Scotogenic model and the IHDM such that they can be discriminated. However, in this parameter space, the stability of the $\mathbb{Z}_2$ symmetry is not guaranteed. We find that a mass splitting of ~ 30 [GeV] between η_R and N_1, the value of the cross section in the Scotogenic model decreases around 20% in comparison to the value of the cross section in the IHDM. Because the mass difference is small, a study of the stability of the $\mathbb{Z}_2$ symmetry is necessary. Another interesting result we find is when the mass of N_1 is smaller than the mass of η_R. For a mass splitting close to 350 [GeV] the value of the cross section for the Scotogenic model falls almost a third of the IHDM cross section value. Since we focus on a study of scalar dark matter, a future study is needed.

In the second part of our work we have reexamined the generalized version of the minimal Singlet + Triplet Scotogenic Model. We have assumed dark matter to be a scalar WIMP in a freeze-out scenario and we have presented a full numerical analysis of the signatures expected at dark matter detectors as well as collider experiments. We have identified the regions of parameters where dark matter predictions are in agreement with theoretical and experimental constraints, such as those coming from the stability of the $\mathbb{Z}_2$ symmetry, Lepton Flavor violation data, neutrino oscillation data, Higgs data, dark matter relic abundance and direct detection searches. Further, we have presented expectations for near future direct and indirect detection experiments. In the case of direct searches, we have found that most of the allowed results that explain the total dark matter abundance in the Universe are located only in a vertical region for a mass of η_R between $500 - 600$ [GeV]. It is worth commenting on how the phenomenology of η_R dark matter compares to that of the scalar dark matter in the simple Scotogenic Model [185]. While the two candidates have similar properties, the presence of a scalar triplet in the Singlet + Triplet Scotogenic Model slightly changes the interaction of η_R with the Higgs boson. As a consequence, both its Higgs-mediated annihilation cross section as well as the η_R-nucleon interaction cross section contain a term dependent on μ_2 and on v_Ω (see the relevant vertex in Appendix D.3). This is nonetheless weighted by the (small) mixing between h^0 and H. As a result the η_R dark matter phenomenology turns out to be very similar in both models. The real advantage of the Singlet + Triplet Scotogenic Model comes from the enlarged viable parameter space, especially at low η_R masses, as it avoids the unwanted spontaneous breaking of the $\mathbb{Z}_2$ parity symmetry [188]. In the indirect detection results, we have found some interesting points which could be tested by the future experiments as Fermi-LAT and CTA in two mass region for η_R: ~ 70 [GeV] and ≥ 500. We have examined the collider signatures associated to the mono-jet channel at the LHC. This signal presents an interesting contribution in comparison with the background of the experiments at the LHC for a mass of the dark matter up to ~ 60 [GeV].

6

Future works

We believe that the following future studies related with our work, are interesting

- In the case of the discrimination of the IHDM with the Scotogenic model, it would be interesting study some signals at one loop level. If the value of the parameter λ_5 is small enough to increase the value of the new yukawa couplings Y^N, a considerable contribution over the dark matter-nuclei scattering spin independent cross section in the Scotogenic model would contribute to the differentiation of both model. Also an study of the same signal, $e^+e^- \to \eta^+\eta^-$, considering a fermionic dark matter scenario would present a prominent result.

- For some studies in indirect searches in the Singlet+Triplet Scotogenic model, we know that η_R will annihilate into gamma rays at one loop level, mediated by the Higgs boson (either h^0 or H_2). The contribution can be rather large depending of the coupling of η_R with the Higgs or the effective coupling that will arise from the loop contribution. A detailed work including loop contributions would be interested to be tested with some experiments as for example the search for spectral lines in the Fermi-LAT gamma rays observations of the Milky Way halo. Also, as we mentioned during this thesis, a deep study related to the Sommerfeld enhancement would be important to realize, which we did not considered because it was beyond the scope of this work.

- Our collider study should encourage future studies at the upcoming high-luminosity run of the LHC and a better analysis of the electroweak oblique parameters at one loop for the region of masses of η_R up to 60 GeV.

- In all the models we computed the spin-independent η_R-nuclei elastic scattering cross section only at tree level contributions numerically, using microOMEGAs tool. Some works in literature [263,

264] suggest that one-loop diagrams with gauge bosons may become relevant in some regions of parameters, particularly when the mass splitting between the dark particles in the scalar sector is small and also the value of the quartic couplings. In the case of the last model studied in this thesis, the Singlet + Triplet Scotogenic Model, the situation is a little different in comparison with the Inert Higgs Doublet Model for example, because of the scalar sector also includes a new triplet. In comparison with [263] where the mass splitting is only generated at the loop level, our model includes mass splittings between the dark scalar sector also at tree level. Nevertheless, in the case of both the Scotogenic models, loop contributions where the new particles of the dark sector contributes, would introduce high values to the dark matter-nuclei scattering spin independent cross section, depending of the smallness of the λ_5 parameter, increasing the value of the new Yukawas coupling. An interesting and detailed study where gauge contributions may dominate for some specific parameter combinations in the Singlet + Triplet Scotogenic Model should be done.

A

Notation and conventions

A.1 Spinor conventions

The convention for the Pauli matrices is

$$\sigma_1 = \begin{pmatrix} 0 & 1 \\ 1 & 0 \end{pmatrix} \tag{A.1}$$

$$\sigma_2 = \begin{pmatrix} 0 & -i \\ i & 0 \end{pmatrix} \tag{A.2}$$

$$\sigma_3 = \begin{pmatrix} 1 & 0 \\ 0 & -1 \end{pmatrix} \tag{A.3}$$

The properties of the Pauli matrices are

$$[\sigma_i, \sigma_j] = 2i\epsilon_{ijk}\sigma_k \tag{A.4}$$

$$\{\sigma_i, \sigma_j\} = -2\delta_{ij} \tag{A.5}$$

where $i, j = 1, 2, 3$ and

$$\epsilon_{ijk} = \begin{cases} 0 & \text{if the is a repeated index.} \\ +1 & \text{if the permutation of index } ijk \text{ is even.} \\ -1 & \text{if the permutation of index } ijk \text{ is odd.} \end{cases} \tag{A.6}$$

The gamma matrices are defined as the four matrices γ^μ as

$$\{\gamma^\mu, \gamma^\nu\} = -2g^{\mu\nu}. \tag{A.7}$$

We have used the gamma matrices in the Weyl basis, where they have been defined as

$$\gamma_0 = \begin{pmatrix} 0 & 1_{2\times 2} \\ 1_{2\times 2} & 0 \end{pmatrix} \tag{A.8}$$

$$\gamma_i = \begin{pmatrix} 0 & -\sigma_i \\ \sigma_i & 0 \end{pmatrix} \tag{A.9}$$

$$\gamma_5 = \gamma_0\gamma_1\gamma_2\gamma_3 \begin{pmatrix} -1_{2\times 2} & 0 \\ 0 & 1_{2\times 2} \end{pmatrix} \tag{A.10}$$

A.2 Useful relations and formulas for gamma matrices

A useful relations between the gamma matrices that we used in this thesis for the calculus of the scattering amplitud is

$$(\gamma_u)^\dagger = \gamma_0\gamma_{mu}\gamma_0. \tag{A.11}$$

Also, the relations involving contractions of gamma matrices are that we used are

$$\gamma^\mu\gamma_\mu = 41_{4\times 4}, \tag{A.12}$$

$$\gamma^\mu\gamma^\nu\gamma_\mu = -2\gamma^\nu, \tag{A.13}$$

$$\gamma^\mu\gamma_\mu = 4g^{\nu\sigma}, \tag{A.14}$$

$$\gamma^\mu\gamma^\nu\gamma^\sigma\gamma_\rho\gamma_\mu = -2\gamma^\nu\gamma^\sigma\gamma^\rho. \tag{A.15}$$

$$\tag{A.16}$$

A.3 Redefinition of the fields ϕ and η

We can notice in equation 2.1 that m_ϕ^2, m_η^2 and λ_{1-4} are real because $\phi^\dagger\phi$, $\eta\eta^\dagger$ and $(\phi^\dagger\eta)$ are real. In the case of λ_5 the parameter can be complex. We can add a phase to the doublet fields keeping the scalar potential unchanged, and getting a real value for λ_5.

We can redefine the fields ϕ and η, performing the following transformation

$$\phi \rightarrow \phi' = e^{i\rho_\phi}\phi, \tag{A.17}$$

$$\eta \rightarrow \eta' = e^{i\rho_\eta}\eta. \tag{A.18}$$

We can analyze each term of the scalar potential with the new definitions of the fields where we will have

$$\begin{aligned}
\phi^\dagger\phi &\rightarrow e^{-i\rho_\phi}\phi^\dagger e^{i\rho_\phi}\phi, \\
\eta^\dagger\eta &\rightarrow e^{-i\rho_\eta}\eta^\dagger e^{i\rho_\eta}\eta. \\
\phi^\dagger\eta &\rightarrow e^{-i\rho_\phi}\phi^\dagger e^{i\rho_\eta}\eta = e^{\rho_\eta-\rho_\phi}\phi^\dagger\eta. \\
\eta^\dagger\phi &\rightarrow e^{-i\rho_\eta}\eta^\dagger e^{i\rho_\phi}\phi = e^{\rho_\phi-\rho_\eta}\eta^\dagger\phi.
\end{aligned} \tag{A.19}$$

where we can notice that the parameters λ_{1-4} are not modified because they are real. For λ_5 we have the next situation

$$\begin{aligned}
(\phi^\dagger\eta)^2 &\rightarrow e^{2i(\rho_\eta-\rho_\phi)}(\phi^\dagger\eta)^2, \\
(\eta^\dagger\phi)^2 &\rightarrow e^{2i(\rho_\phi-\rho_\eta)}(\eta^\dagger\phi)^2.
\end{aligned} \tag{A.20}$$

We can notice that $\lambda_5 = \lambda_5 e^{i\theta}$ and

$$\begin{aligned}
\frac{\lambda_5}{2}(\phi^\dagger\eta)^2 + \frac{\lambda_5^*}{2}(\eta^\dagger\phi)^2 &\rightarrow \frac{|\lambda_5|}{2}\left[e^{i\theta}e^{2i(\rho_\eta-\rho_\phi)}(\phi^\dagger\eta)^2 + e^{-i\theta}e^{2i(\rho_\phi-\rho_\eta)}(\eta^\dagger\phi)^2\right] \\
&\rightarrow \frac{|\lambda_5|}{2}\left[e^{i(2\rho_\eta-2\rho_\phi+\theta)}(\phi^\dagger\eta)^2 + e^{-i\theta}e^{i(2\rho_\phi-2\rho_\eta-\theta)}(\eta^\dagger\phi)^2\right].
\end{aligned}$$

In order to keep the Lagrangian invariant, we rewrite λ_5 as

$$\lambda \rightarrow \lambda_5 e^{2i(\rho_\phi-\rho_\eta)}. \tag{A.21}$$

where $\theta = 2(\rho_\phi - \rho_\eta)$ is the global phase that was added. Now all the parameters in the Scalar potential given in equation 2.1 are defined real.

B

Theoretical constraints

Here we will present the renormalization group equations (RGEs) for both, the Scotogenic models that were computed first in [224] and for the Singlet + Triplet Scotogenic model. We have used them for the analysis of the $\mathbb{Z}_2$ symmetry.
For simplicity, we have defined the differential operator $\mathcal{D} \equiv 16\pi^2 \mu \frac{d}{d\mu}$.

B.1 Renormalization group equations for the Scotogenic model

We have used the abbreviations $T \equiv \mathrm{Tr}\left(Y_e^\dagger Y_e + 3Y_u^\dagger Y_u + 3Y_d^\dagger Y_d\right)$, $T_4 \equiv \mathrm{Tr}\left(Y_e^\dagger Y_e Y_e^\dagger Y_e + 3Y_u^\dagger Y_u Y_u^\dagger Y_u + 3Y_d^\dagger Y_d Y_d^\dagger Y_d\right)$, $T_N \equiv \mathrm{Tr}\left(Y^{N\dagger} Y^N\right)$, $T_{4N} \equiv \mathrm{Tr}\left(Y^{N\dagger} Y^N Y^{N\dagger} Y^N\right)$ and $T \equiv \mathrm{Tr}\left(Y^{N\dagger} Y^N Y_e^\dagger Y_e\right)$. The RGEs for the gauge couplings are

$$\mathcal{D} g_i = b_i g_i^3 \tag{B.1}$$

with $b = (7, -3, -7)$. The RGEs for the yukawa couplings in the standard model are

$$\mathcal{D} Y_u = Y_u \left[\frac{3}{2} Y_u^\dagger Y_u - \frac{3}{2} Y_d^\dagger Y_d + T - \frac{17}{12} g_1^2 - \frac{9}{4} g_2^2 - 8 g_3^2\right], \tag{B.2}$$

$$\mathcal{D} Y_d = Y_d \left[\frac{3}{2} Y_d^\dagger Y_d - \frac{3}{2} Y_u^\dagger Y_u + T - \frac{15}{12} g_1^2 - \frac{9}{4} g_2^2 - 8 g_3^2\right], \tag{B.3}$$

$$\mathcal{D} Y_e = Y_e \left[\frac{3}{2} Y_e^\dagger Y_e + \frac{1}{2} Y^{N\dagger} Y^N + T - \frac{15}{4} g_1^2 - \frac{9}{4} g_2^2\right]. \tag{B.4}$$

For the new yukawa couplings and the Majorana mass matrix, we have

$$\mathcal{D}Y^N = Y^N\left[\frac{3}{2}Y^{N\dagger}Y^N + \frac{1}{2}Y_e^\dagger Y_e + T_N - \frac{3}{4}g_1^2 - \frac{9}{4}g_2^2\right], \tag{B.5}$$

$$\mathcal{D}M = \left[\left(Y^N Y^{N\dagger}\right)M + M\left(Y^N Y^{N\dagger}\right)^*\right]. \tag{B.6}$$

For the quartic scalar coupling we have

$$\begin{aligned}
\mathcal{D}\lambda_1 &= 12\lambda_1^2 + 4\lambda_3^2 + 4\lambda_3\lambda_4 + 2\lambda_4^2 + 2\lambda_5^2 + \frac{3}{4}\left(g_1^4 + 2g_1^2g_2^2 + 3g_2^4\right) \\
&- 3\lambda_1(g_1^2 + 3g_2^2) + 4\lambda_1 T - 4T_4, \qquad \text{(B.7)} \\
\mathcal{D}\lambda_2 &= 12\lambda_2^2 + 4\lambda_3^2 + 4\lambda_3\lambda_4 + 2\lambda_4^2 + 2\lambda_5^2 + \frac{3}{4}\left(g_1^4 + 2g_1^2g_2^2 + 3g_2^4\right) \\
&- 3\lambda_2(g_1^2 + 3g_2^2) + 4\lambda_2 T - 4T_{4N}, \qquad \text{(B.8)} \\
\mathcal{D}\lambda_3 &= 2\left(\lambda_1 + \lambda_2\right)\left(3\lambda_3 + \lambda_4\right) + 4\lambda_3^2 + 2\lambda_4^2 + 2\lambda_5^2 + \frac{3}{4}\left(g_1^4 - 2g_1^2g_2^2 + 3g_2^2\right) \\
&- 3\lambda_3\left(g_1^2 + 3g_2^2\right) + 2\lambda_3(T + T_N) - 4T_{Ne}, \qquad \text{(B.9)} \\
\mathcal{D}\lambda_4 &= 2\left(\lambda_1 + \lambda_2\right)\lambda_4 + 8\lambda_3\lambda_4 + 4\lambda_4^2 + 8\lambda_5^2 + 3g_1^2g_2^2 \\
&- 2\lambda_4(g_1^2 + 3g_2^2) + 2\lambda_4(T + T_N) + 4T_{Ne}, \qquad \text{(B.10)} \\
\mathcal{D}\lambda_5 &= \lambda_5\left[2\left(\lambda_1 + \lambda_2\right) + 8\lambda_3 + 12\lambda_4 - 3(g_1^2 + 3g_2^2) + 2(T + T_N)\right]. \qquad \text{(B.11)}
\end{aligned}$$

For the scalar mass parameters the RGEs are

$$\mathcal{D}m_\phi^2 = 6\lambda_1 m_\phi^2 + 2(2\lambda_3 + \lambda_4)m_\eta^2 + m_\phi^2\left[2T - \frac{3}{2}(g_1^2 + 3g_2^2)\right], \tag{B.12}$$

$$\mathcal{D}m_\eta^2 = 6\lambda_2 m_\eta^2 + 2(2\lambda_3 + \lambda_4)m_\phi^2 + m_\eta^2\left[2T - \frac{3}{2}(g_1^2 + 3g_2^2)\right] - 4\sum_{i=1}^{3} M_{N_1}^2\left(Y^N Y^{N\dagger}\right)_{ii}. \tag{B.13}$$

B.2 Renormalization group equations for the Singlet + Triplet Scotogenic model

The RGEs for the gauge couplings are the same than in equation B.1 but for this model $b = (\frac{21}{5}, -\frac{4}{3}, -7)$.

For the Yukawa couplings of the Standard Model, the RGEs are

$$\begin{aligned}
\mathcal{D}Y_u^{\alpha\beta} &= -\frac{3}{2}\Big(-Y_u Y_u^\dagger Y_u + Y_u Y_d^\dagger Y_d\Big)^{\alpha\beta} \\
&+ \left[3\mathrm{Tr}\Big(Y_d Y_d^\dagger\Big) + 3\mathrm{Tr}\Big(Y_u Y_u^\dagger\Big) + \mathrm{Tr}\Big(Y_e Y_e^\dagger\Big) - 8g_3^2 - \frac{17}{20}g_1^2 - \frac{9}{4}g_2^2\right]Y_u^{\alpha\beta} \qquad \text{(B.14)} \\
\mathcal{D}Y_d^{\alpha\beta} &= \frac{3}{2}\Big(-Y_d Y_u^\dagger Y_u + Y_d Y_d^\dagger Y_d\Big)^{\alpha\beta}
\end{aligned}$$

$$+\Big(3\mathrm{Tr}\Big(Y_dY_d^\dagger\Big)+3\mathrm{Tr}\Big(Y_uY_u^\dagger\Big)+\mathrm{Tr}\Big(Y_eY_e^\dagger\Big)-\frac{9}{4}g_2^2-\frac{1}{4}g_1^2-8g_3^2\Big)Y_d^{\alpha\beta} \tag{B.15}$$

$$\mathcal{D}Y_e=\frac{3}{2}Y_eY_e^\dagger Y_e+\frac{1}{2}\Big(Y_eY_F^*\Big)^\alpha Y_F^\beta+\frac{3}{4}\Big(Y_eY_\Sigma^*\Big)^\alpha Y_\Sigma^\beta$$
$$+\Big(3\mathrm{Tr}\Big(Y_dY_d^\dagger\Big)+3\mathrm{Tr}\Big(Y_uY_u^\dagger\Big)+\mathrm{Tr}\Big(Y_eY_e^\dagger\Big)-\frac{9}{4}g_1^2-\frac{9}{4}g_2^2\Big)Y_e^{\alpha\beta} \tag{B.16}$$

$$\mathcal{D}Y_F^\alpha=\Big[\Big(\frac{2}{3}|Y_\Omega|^2+\frac{2}{3}\Big(Y_\Sigma Y_\Sigma^*\Big)+\frac{5}{2}\Big(Y_FY_F^*\Big)-\frac{9}{20}g_1^2-\frac{9}{4}g_2^2\Big)\Big]Y_F^\alpha+\frac{1}{2}\Big(Y_e^TY_e^*Y_F\Big)^\alpha+\frac{3}{4}\Big(Y_FY_\Sigma^*\Big)Y_\Sigma^\alpha \tag{B.17}$$

$$\mathcal{D}Y_\Sigma^\alpha=\Big[\frac{1}{2}|Y_\Omega|^2+\Big(Y_FY_F^*\Big)+\frac{3}{2}\Big(Y_\Sigma Y_\Sigma^*\Big)-\frac{9}{20}g_1^2-\frac{33}{44}g_2^2\Big]Y_\Sigma^\alpha+\frac{1}{2}\Big(Y_e^TY_e^*Y_\Sigma\Big)^\alpha+\frac{3}{4}\Big(Y_\Sigma Y_F^*\Big)Y_F^\alpha \tag{B.18}$$

$$\mathcal{D}Y_\Omega=\frac{1}{2}Y_\Omega\Big(-12g_2^2+12|Y_\Omega|^2+2\Big(Y_FY_F^*\Big)+\Big(Y_\Sigma Y_\Sigma^*\Big)\Big) \tag{B.19}$$

The RGEs for the quartic scalar couplings are

$$\mathcal{D}\lambda_1=+\frac{27}{100}g_1^4+\frac{9}{10}g_1^2g_2^2+\frac{9}{4}g_2^4-\frac{9}{5}g_1^2\lambda_1-9g_2^2\lambda_1+12\lambda_1^2+4\lambda_3^2+4\lambda_3\lambda_4+2\lambda_4^2$$
$$+2\lambda_5^2+3\lambda_1^{\Omega,2}+12\lambda_1\mathrm{Tr}\Big(Y_dY_d^\dagger\Big)+4\lambda_1\mathrm{Tr}\Big(Y_eY_e^\dagger\Big)+12\lambda_1\mathrm{Tr}\Big(Y_uY_u^\dagger\Big)$$
$$-12\mathrm{Tr}\Big(Y_dY_d^\dagger Y_dY_d^\dagger\Big)-4\mathrm{Tr}\Big(Y_eY_e^\dagger Y_eY_e^\dagger\Big)-12\mathrm{Tr}\Big(Y_uY_u^\dagger Y_uY_u^\dagger\Big) \tag{B.20}$$

$$\mathcal{D}\lambda_2=+\frac{27}{100}g_1^4+\frac{9}{10}g_1^2g_2^2+\frac{9}{4}g_2^4-\frac{9}{5}g_1^2\lambda_2-9g_2^2\lambda_2+12\lambda_2^2+4\lambda_3^2+4\lambda_3\lambda_4+2\lambda_4^2$$
$$+2\lambda_5^2+3(\lambda_\eta^\Omega)^2+4\lambda_2\Big(Y_FY_F^*\Big)-4\Big(Y_FY_F^*\Big)^2-4\Big(Y_FY_\Sigma^*\Big)\Big(Y_\Sigma Y_F^*\Big)$$
$$+6\lambda_2\Big(Y_\Sigma Y_\Sigma^*\Big)-5\Big(Y_\Sigma Y_\Sigma^*\Big)^2 \tag{B.21}$$

$$\mathcal{D}\lambda_3=+\frac{27}{100}g_1^4-\frac{9}{10}g_1^2g_2^2+\frac{9}{4}g_2^4-\frac{9}{5}g_1^2\lambda_3-9g_2^2\lambda_3+6\lambda_1\lambda_3+6\lambda_2\lambda_3+4\lambda_3^2+2\lambda_1\lambda_4$$
$$+2\lambda_2\lambda_4+2\lambda_4^2+2\lambda_5^2+3\lambda_1^\Omega\lambda_\eta^\Omega+2\lambda_3\Big(Y_FY_F^*\Big)-4\Big(Y_FY_e^\dagger Y_eY_F^*\Big)+3\lambda_3\Big(Y_\Sigma Y_\Sigma^*\Big)$$
$$-2\Big(Y_\Sigma Y_e^\dagger Y_eY_\Sigma^*\Big)+6\lambda_3\mathrm{Tr}\Big(Y_dY_d^\dagger\Big)+2\lambda_3\mathrm{Tr}\Big(Y_eY_e^\dagger\Big)+6\lambda_3\mathrm{Tr}\Big(Y_uY_u^\dagger\Big) \tag{B.22}$$

$$\mathcal{D}\lambda_4=+\frac{9}{5}g_1^2g_2^2-\frac{9}{5}g_1^2\lambda_4-9g_2^2\lambda_4+2\lambda_1\lambda_4+2\lambda_2\lambda_4+8\lambda_3\lambda_4+4\lambda_4^2+8\lambda_5^2+2\lambda_4\Big(Y_FY_F^*\Big)$$
$$+4\Big(Y_FY_e^\dagger Y_eY_F^*\Big)+3\lambda_4\Big(Y_\Sigma Y_\Sigma^*\Big)-2\Big(Y_\Sigma Y_e^\dagger Y_eY_\Sigma^*\Big)+6\lambda_4\mathrm{Tr}\Big(Y_dY_d^\dagger\Big)+2\lambda_4\mathrm{Tr}\Big(Y_eY_e^\dagger\Big)$$
$$+6\lambda_4\mathrm{Tr}\Big(Y_uY_u^\dagger\Big) \tag{B.23}$$

$$\mathcal{D}\lambda_5=-\frac{9}{5}g_1^2\lambda_5-9g_2^2\lambda_5+2\lambda_1\lambda_5+2\lambda_2\lambda_5+8\lambda_3\lambda_5+12\lambda_4\lambda_5+2\lambda_5\Big(Y_FY_F^*\Big)+3\lambda_5\Big(Y_\Sigma Y_\Sigma^*\Big)$$
$$+6\lambda_5\mathrm{Tr}\Big(Y_dY_d^\dagger\Big)+2\lambda_5\mathrm{Tr}\Big(Y_eY_e^\dagger\Big)+6\lambda_5\mathrm{Tr}\Big(Y_uY_u^\dagger\Big) \tag{B.24}$$

$$\mathcal{D}\lambda_1^\Omega=+3g_2^4-\frac{9}{10}g_1^2\lambda_1^\Omega-\frac{33}{2}g_2^2\lambda_1^\Omega+6\lambda_1\lambda_1^\Omega+4(\lambda_1^\Omega)^2+10\lambda_1^\Omega\lambda_2^\Omega+4\lambda_3\lambda^\eta+2\lambda_4\lambda^\eta+4\lambda_1^\Omega|Y_\Omega|^2$$
$$+6\lambda_1^\Omega\mathrm{Tr}\Big(Y_dY_d^\dagger\Big)+2\lambda_1^\Omega\mathrm{Tr}\Big(Y_eY_e^\dagger\Big)+6\lambda_1^\Omega\mathrm{Tr}\Big(Y_uY_u^\dagger\Big) \tag{B.25}$$

$$\mathcal{D}\lambda_2^\Omega=2\Big(11(\lambda_2^\Omega)^2-12g_2^2\lambda_2^\Omega+3g_2^4+4\lambda_2^\Omega|Y_\Omega|^2-4|Y_\Omega|^2+(\lambda_1^\Omega)^2+(\lambda_\eta^\Omega)^2\Big) \tag{B.26}$$

$$\mathcal{D}\lambda_\eta^\Omega = +3g_2^4 + 4\lambda_3\lambda_1^\Omega + 2\lambda_4\lambda_1^\Omega - \frac{9}{10}g_1^2\lambda_\eta^\Omega - \frac{33}{2}g_2^2\lambda_\eta^\Omega + 6\lambda_2\lambda_\eta^\Omega + 10\lambda_2^\Omega\lambda_\eta^\Omega + 4(\lambda_\eta^\Omega)^2 + 2\lambda_\eta^\Omega\Big(Y_F Y_F^*\Big) + 4|Y_\Omega|^2\Big(-2\Big(Y_F Y_F^*\Big) - \Big(Y_\Sigma Y_\Sigma^*\Big) + \lambda_\eta^\Omega\Big) + 3\lambda_\eta^\Omega\Big(Y_\Sigma Y_\Sigma^*\Big) \tag{B.27}$$

The respective RGEs for the trilinear scalar couplings are

$$\mathcal{D}\mu_1 = -\frac{9}{10}g_1^2\mu_1 - \frac{21}{2}g_2^2\mu_1 + 2\lambda_1\mu_1 + 4\lambda_1^\Omega\mu_1 + 2\lambda_4\mu_2 + 2\mu_1|Y_\Omega|^2 + 6\mu_1\mathrm{Tr}\Big(Y_d Y_d^\dagger\Big) + 2\mu_1\mathrm{Tr}\Big(Y_e Y_e^\dagger\Big) + 6\mu_1\mathrm{Tr}\Big(Y_u Y_u^\dagger\Big) \tag{B.28}$$

$$\mathcal{D}\mu_2 = +2\lambda_4\mu_1 - \frac{9}{10}g_1^2\mu_2 - \frac{21}{2}g_2^2\mu_2 + 2\lambda_2\mu_2 + 4\lambda_\eta^\Omega\mu_2 + 2\mu_2\Big(Y_F Y_F^*\Big) + 4Y_\Omega M_F^*\Big(Y_F Y_\Sigma^*\Big) + 4Y_\Omega M_\Sigma^*\Big(Y_\Sigma Y_F^*\Big) + 2Y_\Omega^*\Big(2M_F\Big(Y_\Sigma Y_F^*\Big) + 2M_\Sigma\Big(Y_F Y_\Sigma^*\Big) + \mu_2 Y_\Omega\Big) + 3\mu_2\Big(Y_\Sigma Y_\Sigma^*\Big) \tag{B.29}$$

For the new fermion mass terms the RGEs are

$$\mathcal{D}M_F = 2M_N\Big(Y_F Y_F^*\Big) + 6Y_\Omega^2 M_\Sigma^* + 3M_N|Y_\Omega|^2 \tag{B.30}$$

$$\mathcal{D}M_\Sigma = 2Y_\Omega^2 M_F^* + M_\Sigma\Big(-12g_2^2 + |Y_\Omega|^2 + \Big(Y_\Sigma Y_\Sigma^*\Big)\Big) \tag{B.31}$$

Finally, the RGEs for the scalar mass terms are

$$\mathcal{D}m_\phi^2 = -4\lambda_3 m_\eta^2 - 2\lambda_4 m_\eta^2 - \frac{9}{10}g_1^2 m_\phi^2 - \frac{9}{2}g_2^2 m_\phi^2 + 6\lambda_1 m_\phi^2 + 3\lambda_1^\Omega m_\Omega^2 - 3\mu_1^2 + 6m_\phi^2\mathrm{Tr}\Big(Y_d Y_d^\dagger\Big) + 2m_\phi^2\mathrm{Tr}\Big(Y_e Y_e^\dagger\Big) + 6m_\phi^2\mathrm{Tr}\Big(Y_u Y_u^\dagger\Big) \tag{B.32}$$

$$\mathcal{D}m_\eta^2 = -\frac{9}{10}g_1^2 m_\eta^2 - \frac{9}{2}g_2^2 m_\eta^2 + 6\lambda_2 m_\eta^2 - 4\lambda_3 m_\phi^2 - 2\lambda_4 m_\phi^2 - 3\lambda_\eta^\Omega m_\Omega^2 + 3\mu_2^2 + 2\Big(m_\eta^2 - 2|M_F|^2\Big)\Big(Y_F Y_F^*\Big) + 3\Big(m_\eta^2 - 2|M_\Sigma|^2\Big)\Big(Y_\Sigma Y_\Sigma^*\Big) \tag{B.33}$$

$$\mathcal{D}m_\Omega^2 = -2\Big(2\lambda_\eta^\Omega m_\eta^2 - 2\lambda_1^\Omega m_\phi^2 + 6g_2^2 m_\Omega^2 - 5\lambda_2^\Omega m_\Omega^2 + \mu_1^2 + \mu_2^2 - 2|Y_\Omega|^2\Big(2M_\Sigma M_\Sigma^* + m_\Omega^2\Big) - 2M_F M_\Sigma Y_\Omega^{*2} - 2Y_\Omega M_F^*\Big(2M_F Y_\Omega^* + Y_\Omega M_\Sigma^*\Big)\Big) \tag{B.34}$$

C

Computation of the cross section and decay rate

C.1 Decay rate and cross section

There are particles, like the muons that will decay due to they are not stable. The decay rate Γ is the probability that the muon decay per time [265]. We can define

$$\begin{aligned} dN &= -\Gamma N dt \\ N(t) &= N(0) \exp -\Gamma t. \end{aligned} \tag{C.1}$$

as number of muons at a given time t, where $N\Gamma dt$ of them will decay at t. The life media is defined as

$$\tau = \frac{1}{\Gamma}. \tag{C.2}$$

Branching ratios, that are the fraction of all particles of the given type that decay depending of each mode, are defined as

$$B(A \to B\bar{B}) = \frac{\Gamma_{B\bar{B}}}{\Gamma_{\text{total}}}, \tag{C.3}$$

that is the probability that the particle A decay in the particle B. All the sum of the branching ratios will be equal to 1.

When a particle suffer a scattering, the trajectory of it will change. Considering a beam of incoming particles whit luminosity $\mathcal{L}u$, the number of particles per unit of time scattered into a solid angle will be

$$\begin{aligned} dN &= \mathcal{L}ud\sigma = \mathcal{L}ud\sigma d\Omega \\ \frac{d\sigma}{d\Omega} &= \frac{1}{\mathcal{L}u}\frac{dN}{d\Omega}. \end{aligned} \tag{C.4}$$

Than means that the cross section per luminosity is interpreted as the event rate.

Considering two particles involve in a scattering process, where A and B are the incoming particles and C and D the outcoming, the transition amplitude is

$$\mathcal{T} = -iN_A N_B N_C N_D (2\pi)^4 \delta^{(4)}(p_D + p_C - p_A - p_B)|\mathcal{M}a|^2. \tag{C.5}$$

where N_X with (X=A,B,C,D) is $N = \sqrt{V}^{-1}$ with V the volume where the process happens. Considering the last definitions, the transition rate per volume unit is defined as

$$W = \frac{(2\pi)^4}{V^4}\delta^{(4)}(\rho_D + \rho_C - \rho_A - \rho_B)|\mathcal{M}a|^2. \tag{C.6}$$

where in order to get the event rate we have to multiply the last equation by the number of final states. In the case of the differential cross section $d\sigma$ considering equations C.1 and C.6, we have

$$d\sigma| = \frac{W}{\mathcal{L}u} \times \rho_{\text{final}} \tag{C.7}$$

where ρ_{final} is the density number of the final states. Because $\frac{Vd^3\rho}{(2\pi)^3}$ is the number of states per particle in a volume V where E is the energy of the particle, we have that the differential cross section is redefine as

$$\mathcal{L}ud\sigma = \frac{(2\pi)^4}{V^4}\delta^4(\rho_C + \rho_D - \rho_A - \rho_B)|\mathcal{M}a|^2 \frac{Vd^3\rho_C}{((2\pi)^3 2E_C)}\frac{Vd^3\rho_D}{((2\pi)^3 2E_D)}. \tag{C.8}$$

For the calculus of the differential cross section we do some considerations

- the number outcoming particles is two.
- the number of incoming particles that are traveling is $|\mathbf{v}_A|2E_A/V$ while the number of target particles is $2E_B/V$,
- the incoming flux is given by
$$\mathcal{F} = |\mathbf{v}_A|\frac{2E_A}{V}\frac{2E_B}{V}$$
,

and we have

$$d\sigma = \frac{|\mathcal{M}a|^2}{4E_A E_B|\mathbf{v}_A|^2}(2\pi)^4\delta^{(4)}(\rho_C + \rho_D - \rho_A - \rho_B)\frac{d^3\rho_C}{(2\pi)^3 2E_C}\frac{d^3\rho_D}{(2\pi)^3 2E_D} \tag{C.9}$$

that is the golden rule for scattering where $\mathcal{M}a$ is the scattering amplitude that must be calculated [265].

In the case of the decay rate of one particle going to others, we have the golden rule for decays

$$d\Gamma = \frac{|\mathcal{M}a|^2}{2_{m_A}}(2\pi)^4\delta^{(4)}(\rho_A - \rho_B - \rho_C - ... - \rho_n)\frac{d^3\rho_B}{(2\pi)^3 2E_B}\frac{d^3\rho_C}{(2\pi)^3 2E_C}...\frac{d^3\rho_n}{(2\pi)^3 2E_n}. \tag{C.10}$$

C.2 Scattering amplitude for the Scotogenic model

Here we will calculate scattering amplitude for the signature $e^+e^- \to \eta^+\eta^-$ for the Inert Higgs Doublet Model and the Scotogenic model. For the process in both models, the Feynman diagrams involve are display in figure (3.6). For simplicity, we have excluded higgs contributions due to it will be smaller than others contributions and we only considered the extra contribution of N_1.
Considering the center of mass frame, the respective momentum of each particle will be

$$P_1 = (E_1, 0, 0, p1) \tag{C.11}$$
$$P_2 = (E_2, 0, 0, -p1) \tag{C.12}$$
$$P_3 = (E_3, p_3\mathrm{sin}\theta, 0, \mathrm{p_3cos}\theta) \tag{C.13}$$
$$P_4 = (E_4, -p_3\mathrm{sin}\theta, 0, -\mathrm{p_3cos}\theta) \tag{C.14}$$
$$\tag{C.15}$$

Due to linear momentum conservation the energy for each particle involve in the process is

$$E_1 = \sqrt{p_1^2 + m_e^2} \tag{C.16}$$
$$E_2 = \sqrt{p_1^2 + m_e^2} \tag{C.17}$$
$$E_3 = \sqrt{p_3^2 + m_\eta^2} \tag{C.18}$$
$$E_4 = \sqrt{p_3^2 + m_e^2} \tag{C.19}$$

For $\sqrt{s} = E_1 + E_2 = E_3 + E_4$, we can find that $p_1 = \sqrt{\frac{s}{4} - m_e^2}$ and $p_3 = \sqrt{\frac{s}{4} - m_{\eta^+}^2}$
The contributions involved in the scattering amplitude when we consider $q = p_3 - p_1$ are

$$(P_4 - P_3) \cdot P_1 = E_4E_1 - E_3E_1 + 2p_3p_1\cos\theta, \tag{C.20}$$

$$(P_4 - P_3) \cdot P_2 = E_4E_2 - E_3E_2 + 2p_3p_1\cos\theta, \tag{C.21}$$

$$P_1 \cdot P_2 = E_2E_1 + p_1^2, \tag{C.22}$$

$$(P_4 - P_3) \cdot (P_4 - P_3) = (E_4 - E_3)^2 - 4p_3^2 \tag{C.23}$$

$$q \cdot P_2 = (P_3 - P_1) \cdot P_2 = E_3E_2 - E_1E_2 - p_3p_1\cos\theta + \mathrm{p}_1^2, \tag{C.24}$$

$$q \cdot P_1 = (P_3 - P_1) \cdot P_2 = E_3E_1 - E_1E_1 + p_3p_1\cos\theta - \mathrm{p}_1^2, \tag{C.25}$$

$$(P_4 - P_3) \cdot q = (E_4 - E_3)(E_3 - E_1) - 2p_3^2 + 2p_3p_1\cos\theta. \tag{C.26}$$

For $E_1 = E_2 = E_e$ and $E_3 = E_4 = E_{\eta^+}$ we can rewrite the equations above as

$$(P_4 - P_3) \cdot P_1 = 2p_3p_1\cos\theta, \tag{C.27}$$

$$(P_4 - P_3) \cdot P_2 = 2p_3p_1\cos\theta, \tag{C.28}$$

$$P_1 \cdot P_2 = E_e^2 + p_1^2, \tag{C.29}$$

$$(P_4 - P_3) \cdot (P_4 - P_3) = -4p_3^2 \tag{C.30}$$

$$q \cdot P_2 = (P_3 - P_1) \cdot P_2 = E_{\eta^+}E_e - E_e^2 - p_3p_1\cos\theta + \mathrm{p}_1^2, \tag{C.31}$$

$$q \cdot P_1 = (P_3 - P_1) \cdot P_1 = E_{\eta^+}E_e - E_e^2 + p_3p_1\cos\theta - \mathrm{p}_1^2, \tag{C.32}$$

$$(P_4 - P_3) \cdot q = -2p_3^2 + 2p_3p_1\cos\theta. \tag{C.33}$$

With all the last assumptions the scattering amplitude is

$$\begin{aligned}
|\mathcal{M}_{total}|^2 &= \frac{e^2}{4E_e^4}\left[4p_3^2(E_e^2 + p_1^2 + m_e^2) - 8p_3^2p_1^2\cos^2\theta\right] \\
&+ \frac{g^4\cos(2\theta_\mathrm{w})}{4\cos\theta_\mathrm{w}(4\mathrm{E_e^2} - \mathrm{m_z^2})^4}\left[4p_3^2(E_e^2 + p_1^2 + m_e^2)\left(4\left(2\sin\theta_\mathrm{w} - \frac{1}{2}\right)^2 + 1\right)\right] \\
&+ \frac{g^4\cos(2\theta_\mathrm{w})}{4\cos\theta_\mathrm{w}(4\mathrm{E_e^2} - \mathrm{m_z^2})^4}\left[-8p_3^2p_1^2\cos^2\theta\left(4\left(2\sin\theta_\mathrm{w} - \frac{1}{2}\right)^2 + 1\right)\right] \\
&+ \frac{4e^2g^2}{E_e}\frac{\cos(2\theta_\mathrm{w})}{\cos\theta_\mathrm{w}}\frac{1}{4E_e^2 - m_z^2}\left[4p_3^2(E_e^2 + p_1^2 + m_e^2) - 8p_3^2p_1^2\cos^2\theta\right] \\
&- \frac{4Y_N^2e^2}{E_2^2((E_{\eta^{+2}} - E_e)^2 + p_3^2 - 4p_3p_1\cos\theta + 2\mathrm{p}_1^2 - \mathrm{M_N^2})}[2p_3p_1\cos\theta(2\mathrm{p_3p_1}\cos\theta - 2\mathrm{p}_1^2) \\
&- (E_3^2 + p_1^2)(2p_3p_1\cos\theta - 2\mathrm{p}_3^2) + \mathrm{m_eM_N}4\mathrm{p_3p_1}\cos\theta] \\
&+ \frac{4Y_Ng^2\cos(2\theta_\mathrm{w})(2\sin\theta_\mathrm{w} - 1/2)}{2\cos\theta_\mathrm{w}((\mathrm{E}_{\eta^{+2}} - \mathrm{E_e})^2 + \mathrm{p}_3^2 - 4\mathrm{p_3p_1}\cos\theta + 2\mathrm{p}_1^2 - \mathrm{M_N^2})}\frac{1}{4E_e^2 - m_z^2}[2p_3p_1\cos\theta(2\mathrm{p}_1^2 - 2\mathrm{p_1p_3}\cos\theta) \\
&- (E_e^2 + p_1^2)(2p_3p_1\cos\theta) + \mathrm{M_Nm_e}4\mathrm{p_3p_1}\cos\theta],
\end{aligned} \tag{C.34}$$

where using the golden rule we will have

$$\frac{d\sigma}{d\cos\theta} = \frac{|\mathcal{M}_{total}|^2}{32\pi(E_e)^2}\frac{|\vec{p}_3|}{|\vec{p}_1|}. \tag{C.35}$$

Considering $p_1 = \sqrt{\frac{s}{4} - m_e^2}$ and $p_3 = \sqrt{\frac{s}{4} - m_{\eta^+}^2}$ the final expression will be

$$\frac{d\sigma}{d\cos\theta} = \frac{|\mathcal{M}_{total}|^2}{32\pi(E_e)^2}\frac{\sqrt{\frac{s}{4} - m_{\eta^+}^2}}{\sqrt{\frac{s}{4} - m_e^2}}. \tag{C.36}$$

Taking into account that the mass of the electron is much smaller than the mass of the other particles, we can consider that $m_e \to 0$. The final expression will be

$$\frac{d\sigma}{d\cos\theta} = \frac{|\mathcal{M}_{total}|^2}{32\pi(E_e)^2}\frac{\sqrt{\frac{s}{4} - m_{\eta^+}^2}}{\sqrt{\frac{s}{4}}}. \tag{C.37}$$

where for the scattering amplitude we have

$$\begin{aligned}
|\mathcal{M}_{total}|^2 &= \frac{e^2}{4E_e^4}\left[4p_3^2(E_e^2+p_1^2) - 8p_3^2p_1^2\cos^2\theta\right] \\
&+ \frac{g^4\cos(2\theta_{\rm w})}{\cos\theta_{\rm w}{}^2(4{\rm E}_{\rm e}^2 - {\rm m}_{\rm z}^2)^2}\left[4p_3^2(E_e^2+p_1^2 - 8p_3^2p_1^2\cos^2\theta)\left(2\sin\theta_{\rm w} - \frac{1}{2}\right)^2\right] \\
&+ \frac{g^4\cos(2\theta_{\rm w})}{\cos\theta_{\rm w}{}^2(4{\rm E}_{\rm e}^2 - {\rm m}_{\rm z}^2)^2}\left[p_3^2(E_e^2+p_1^2) - 8p_3^2p_1^2\cos^2\theta\right] \\
&+ \frac{4e^2g^2}{E_e}\frac{cos(2\theta_w)}{\cos\theta_{\rm w}}\frac{1}{4E_e^2 - m_z^2}\left[4p_3^2(E_e^2+p_1^2) - 8p_3^2p_1^2\cos^2\theta\right] \\
&- \frac{2Y_N^2e^2}{(q_N^2 - M_N^2)E_e^2}[(p_3p_1\cos\theta - {\rm p}_1^2)(-2{\rm p}_3{\rm p}_1\cos\theta) \\
&- (E_e^2 + p_1^2 - m_eM_N) + 2p_3^2(E_e^2+p_1^2)] \\
&+ \frac{4Y_Ng^2\cos(2\theta_{\rm w})(2\sin\theta_{\rm w} - 1/2)}{\cos\theta_{\rm w}({\rm q}_{\rm N}^2 - {\rm M}_{\rm N}^2)}\frac{1}{4E_e^2 - m_z^2}[2p_3p_1\cos(\theta)({\rm p}_1^2 - {\rm p}_1{\rm p}_3\cos\theta) \\
&- (E_e^2 + p_1^2 - 2m_eM_N)(2p_3p_1\cos\theta) + 2{\rm p}_3({\rm E}_{\rm e}^2 + {\rm p}_1)],
\end{aligned} \tag{C.38}$$

where $q_N^2 = E_{\eta^+}^2 + E_e^2 - 2E_{\eta^+}E_e + p_3^2 + p_1^2 - 2p_3p_1\cos(\theta)$.

D

Feynman Rules

Here we will present the main Feynman diagrams presented in both models wich will contribute to the correct cosmological relic density.

D.1 Feynman diagrams for relic density in the Scotogenic model

Assuming that η_R is the dark matter of the Scotogenic model, we present the Feynman diagrams to determine the relic density. The figure D.1 show the dark matter annihilation and coannihilation channels.

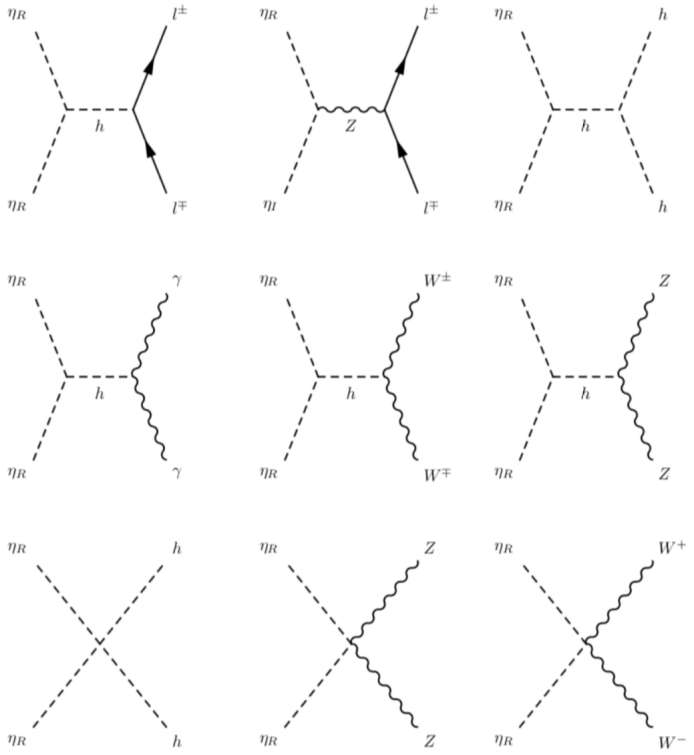
η_R
$l^{\pm}$
h
η_R
$l^{\mp}$
η_R
$l^{\pm}$
Z
η_I
$l^{\mp}$
η_R
h
h
η_R
h
η_R
γ
h
η_R
γ
η_R
$W^{\pm}$
h
η_R
$W^{\mp}$
η_R
Z
h
η_R
Z
η_R
h
η_R
h
η_R
Z
η_R
Z
η_R
W^+
η_R
W^-

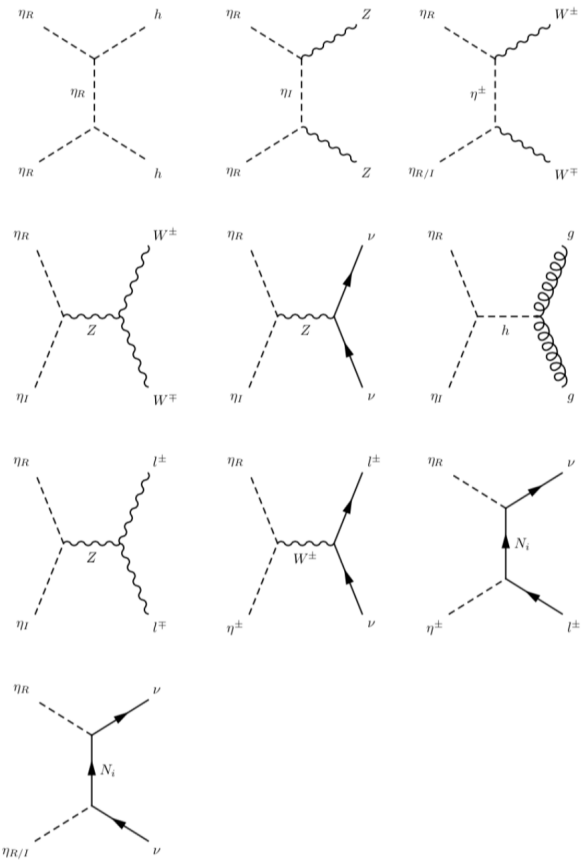

Figure D.1: Annihilation and coannihilation diagrams contributing to the relic abundance of η_R.

D.2 Feynman diagrams for relic density in the Singlet + Triplet model

Here we present some of the main Feynman diagrams of the Singlet+Triplet Scotogenic model, relevant to determine the cosmological relic density, assuming that η_R is the dark matter. Fig. D.2 shows the main dark matter annihilation and coannihilation channels. Besides the standard s-wave annihilation into quarks and gauge bosons, mediated by the SM-like Higgs boson, coannihilations with both η_R and $\eta^\pm$ are possible. These can be mediated either by the Z^0 boson, or also by the new fermions χ_σ. These channels can lead to both charged or neutral leptons in the final state, and involve the contribution of the new Yukawas described in Section 2.3. Notice that these processes are not present in the simple scotogenic constructions [185] nor in the case of the Inert Higgs Doublet Model [189]. Diagrams with quartic interactions will appear when kinematically allowed, starting at $m_{\eta_R} \gtrsim 80$ [GeV].

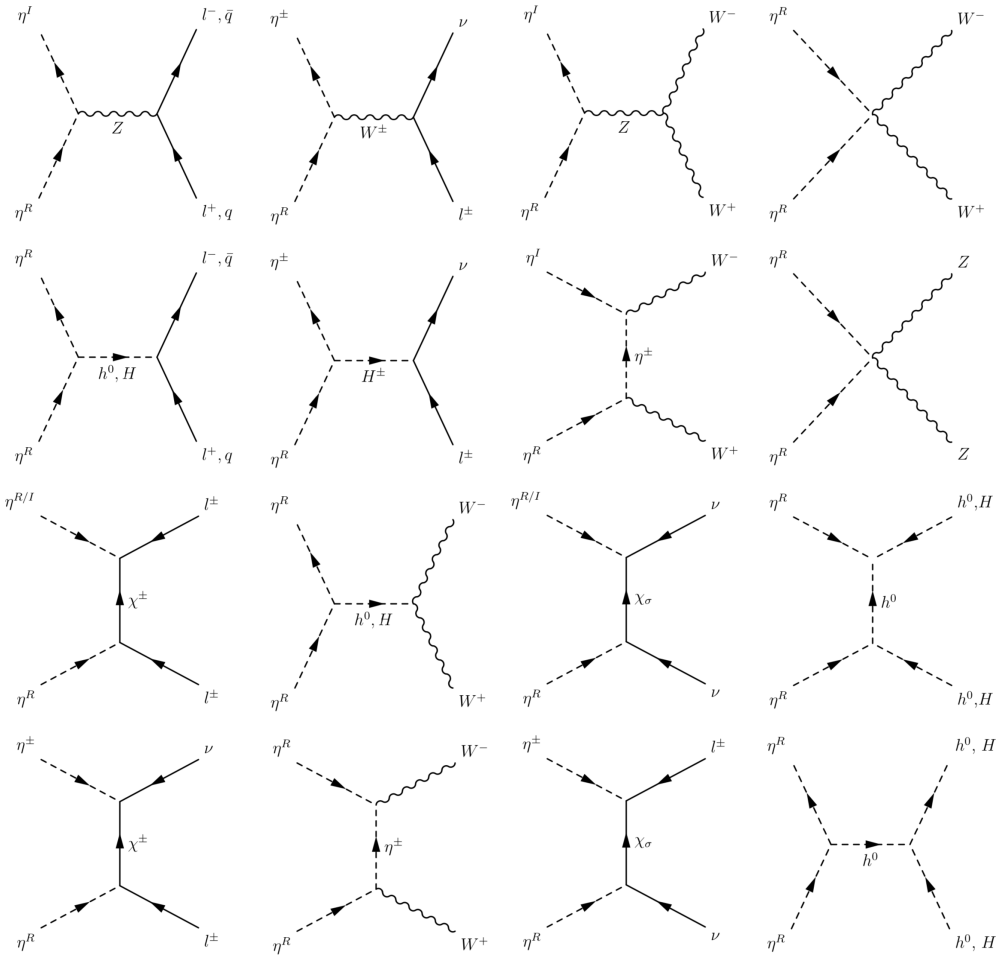

Figure D.2: Relevant annihilation and coannihilation diagrams contributing to the relic abundance of η_R.

D.3 Relevant Feynman rules in direct searches of dark matter

Figure D.3 shows the most important Feynman rules for the relevant scalar dark-matter-physics interactions in the Scotogenic model and the Singlet + Triplet Scotogenic Model. These are important for all the signatures studied in Chapter 4, like the η_R-nucleon spin-independent elastic scattering and for the searches in the $\not{E}_T$+jet channel at the LHC.

In contrast to the simple Scotogenic Model, the interaction vertex with the Higgs is not fully determined by λ_{345}, as it contains an extra contribution dependent on λ_η^Ω and μ_2, involving the heavy neutral scalar H, although weighted by its mixing with h^0. Instead, the interaction vertex with the Z^0 boson depends on the quadrimomenta $p_\mu^{\eta_R}$, $p_\mu^{\eta_I}$ and on the electroweak couplings g_1 and g_2.

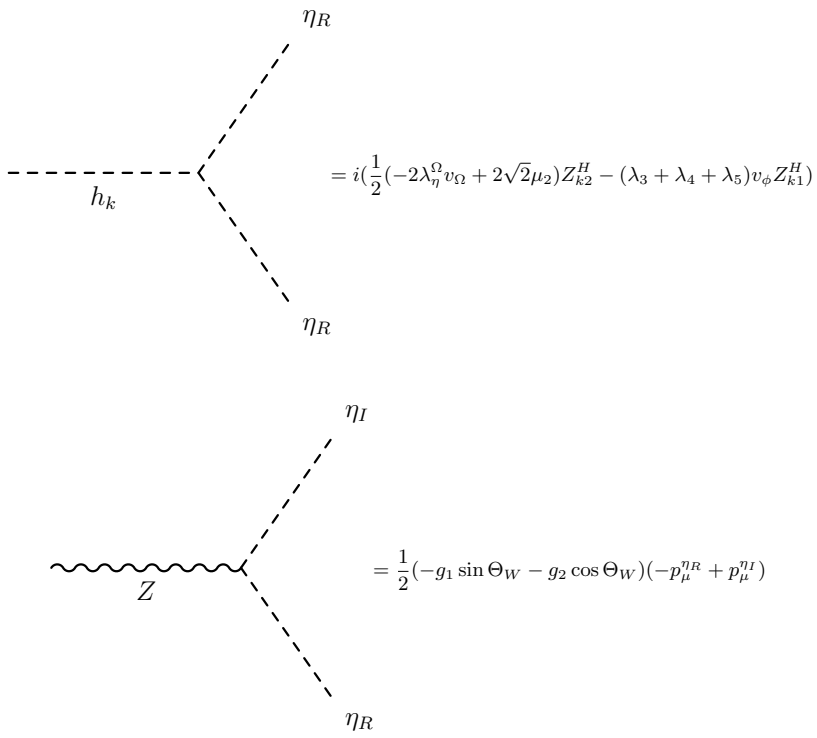

Figure D.3: Relevant η_R interaction vertices. All particle momenta are considered as incoming. In the interaction with neutral scalars, Z_{k1}^H and Z_{k2}^H are entries of the mixing matrix that diagonalizes the mass matrix in Eq. 2.32 ($k = 1$ refers to the Standard Model Higgs h^0 and $k = 2$ to the heavy scalar H). We can notice that in the simple Scotogenic model the contribution with the Higgs only depends of the parameters λ_{345}. In the interaction with the Z^0 boson, g_1 and g_2 are the electroweak coupling constants associated to the SM groups $U(1)_Y$ and $SU(2)_L$, respectively.

D.4 Relevant Feynman rules in the Inert Higgs Doublet Model and the Scotogenic Model

D.4.1 Goldstone-Gauge and new fermions N_i interactions

Here we present the relevant Feynman rules that we used to calculate the scattering cross section in the Inert Higgs Doublet Model and the Scotogenic Model. We are considering $g_v^f = \frac{1}{2}T_f^3 - Q_f \sin^2\theta_{\rm w}$ and $g_A^f = \frac{1}{2}T_f^3$, where the values of T_f^3 and Q_f are listed in table D.1 for each fermion

D.4.2 Propagators in Electroweak Theory

Field	l_L	l_R	ν_L	u_L	d_L	u_R	d_R	ϕ^+	ϕ^0
T_3	$-\frac{1}{2}$	0	$\frac{1}{2}$	$\frac{1}{2}$	$-\frac{1}{2}$	0	0	$\frac{1}{2}$	$-\frac{1}{2}$
Y	$-\frac{1}{2}$	-1	$-\frac{1}{2}$	$\frac{1}{6}$	$\frac{1}{6}$	$\frac{2}{3}$	$-\frac{1}{3}$	$\frac{1}{2}$	$\frac{1}{2}$
Q	-1	-1	0	$\frac{2}{3}$	$-\frac{1}{3}$	$\frac{2}{3}$	$-\frac{1}{3}$	1	0

Table D.1: Particle content and quantum numbers of the Singlet + Triplet Scotogenic Model. The charge assignments of the fields under the global Lepton Number symmetry (L) are also shown.

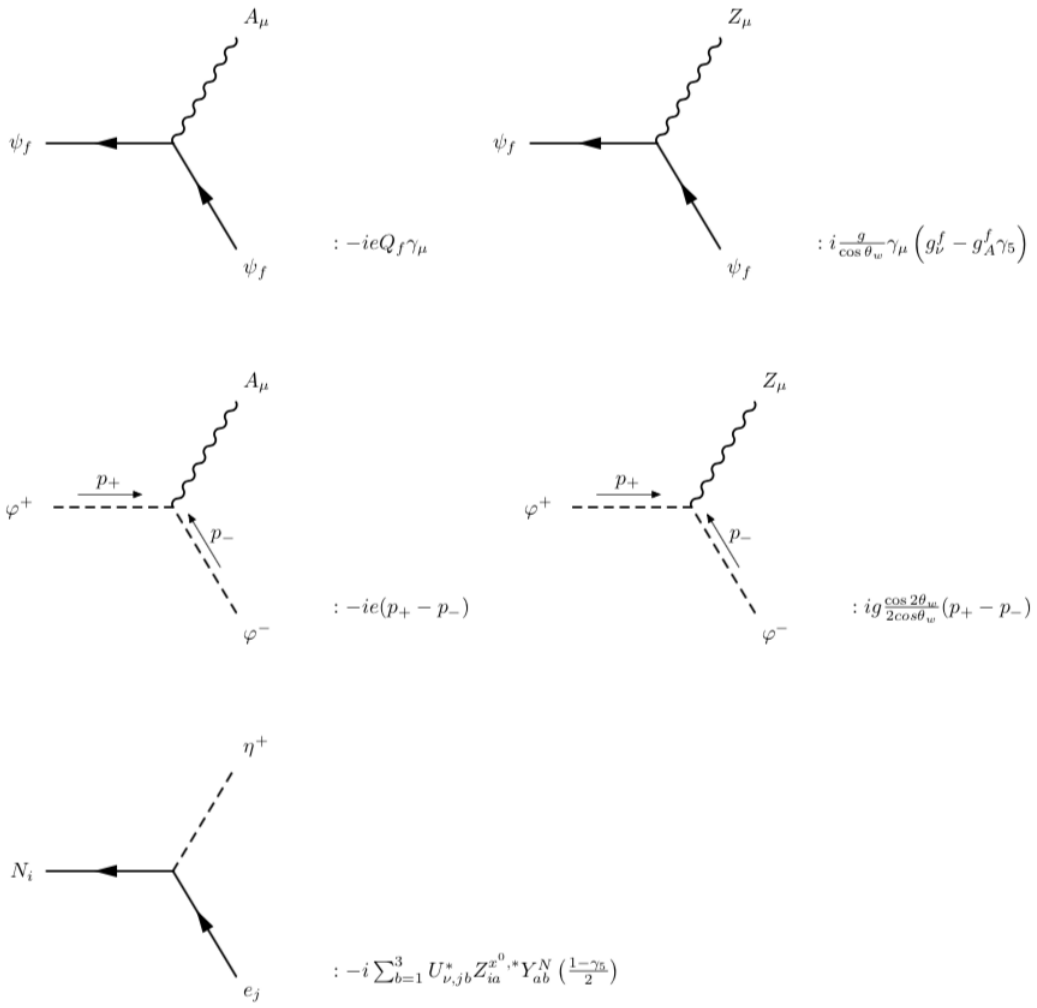
A_μ
ψ_f
ψ_f
$: -ieQ_f\gamma_\mu$
Z_μ
ψ_f
ψ_f
$: i\frac{g}{\cos\theta_w}\gamma_\mu\left(g_\nu^f - g_A^f\gamma_5\right)$
A_μ
φ^+
p_+
p_-
φ^-
$: -ie(p_+ - p_-)$
Z_μ
φ^+
p_+
p_-
φ^-
$: ig\frac{\cos 2\theta_w}{2cos\theta_w}(p_+ - p_-)$
η^+
N_i
e_j
$: -i\sum_{b=1}^{3} U^*_{\nu,jb} Z^{x^0,*}_{ia} Y^N_{ab}\left(\frac{1-\gamma_5}{2}\right)$

Figure D.4

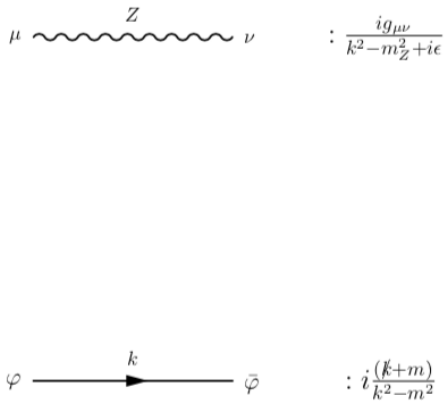
μ
Z
ν
$: \frac{ig_{\mu\nu}}{k^2-m_Z^2+i\epsilon}$
φ
k
$\bar{\varphi}$
$: i\frac{(\not{k}+m)}{k^2-m^2}$

Figure D.5

Bibliography

[1] V. Rubin, N. Thonnard, and J. Ford, W.K., "Rotational properties of 21 SC galaxies with a large range of luminosities and radii, from NGC 4605 /R = 4kpc/ to UGC 2885 /R = 122 kpc/," *Astrophys.J.* **238** (1980) 471.

[2] D. Clowe *et al.*, "A direct empirical proof of the existence of dark matter," *Astrophys.J.* **648** (2006) L109–L113.

[3] J. P. Dietrich *et al.*, "A filament of dark matter between two clusters of galaxies," *Nature* (2012) , arXiv:1207.0809 [astro-ph.CO].

[4] P. Nath *et al.*, "The Hunt for New Physics at the Large Hadron Collider," vol. 200-202, pp. 185–417. 2010. arXiv:1001.2693 [hep-ph].

[5] E. W. Kolb and M. S. Turner, *The Early Universe*, vol. 69. 1990.

[6] S. K. Lee, M. Lisanti, A. H. G. Peter, and B. R. Safdi, "Effect of Gravitational Focusing on Annual Modulation in Dark-Matter Direct-Detection Experiments," *Phys.Rev.Lett.* **112** (2014) 011301, arXiv:1308.1953 [astro-ph.CO].

[7] T. Marrodán Undagoitia and L. Rauch, "Dark matter direct-detection experiments," *J.Phys.* **G43** (2016) 013001, arXiv:1509.08767 [physics.ins-det].

[8] **PandaX-II** Collaboration, A. Tan *et al.*, "Dark Matter Results from First 98.7 Days of Data from the PandaX-II Experiment," *Phys.Rev.Lett.* **117** (2016) 121303, arXiv:1607.07400 [hep-ex].

[9] **LUX** Collaboration, D. Akerib *et al.*, "Results from a search for dark matter in the complete LUX exposure," *Phys.Rev.Lett.* **118** (2017) 021303, arXiv:1608.07648 [astro-ph.CO].

[10] **SuperCDMS** Collaboration, R. Agnese *et al.*, "New Results from the Search for Low-Mass Weakly Interacting Massive Particles with the CDMS Low Ionization Threshold Experiment," *Phys.Rev.Lett.* **116** (2016) 071301, arXiv:1509.02448 [astro-ph.CO].

[11] **CRESST** Collaboration, G. Angloher *et al.*, "Results on light dark matter particles with a low-threshold CRESST-II detector," *Eur.Phys.J.* **C76** (2016) 25, arXiv:1509.01515 [astro-ph.CO].

[12] **XENON** Collaboration, E. Aprile *et al.*, "Physics reach of the XENON1T dark matter experiment," *JCAP* **1604** (2016) 027, arXiv:1512.07501 [physics.ins-det].

[13] **LZ** Collaboration, D. Akerib *et al.*, "LUX-ZEPLIN (LZ) Conceptual Design Report," arXiv:1509.02910 [physics.ins-det].

[14] **DARWIN** Collaboration, J. Aalbers *et al.*, "DARWIN: towards the ultimate dark matter detector," *JCAP* **1611** (2016) 017, arXiv:1606.07001 [astro-ph.IM].

[15] J. Billard, L. Strigari, and E. Figueroa-Feliciano, "Implication of neutrino backgrounds on the reach of next generation dark matter direct detection experiments," *Phys.Rev.* **D89** (2014) 023524, arXiv:1307.5458 [hep-ph].

[16] J. Liu, X. Chen, and X. Ji, "Current status of direct dark matter detection experiments," *Nature Phys.* **13** (2017) 212–216, arXiv:1709.00688 [astro-ph.CO].

[17] **Fermi-LAT** Collaboration, V. Vitale and A. Morselli, "Indirect Search for Dark Matter from the center of the Milky Way with the Fermi-Large Area Telescope," 2009. arXiv:0912.3828 [astro-ph.HE].

[18] M. Lisanti, "Lectures on Dark Matter Physics," pp. 399–446. 2017. arXiv:1603.03797 [hep-ph].

[19] **Planck** Collaboration, P. Ade *et al.*, "Planck 2015 results. XIII. Cosmological parameters," *Astron.Astrophys.* **594** (2016) A13, arXiv:1502.01589 [astro-ph.CO].

[20] **Planck** Collaboration, N. Aghanim *et al.*, "Planck 2018 results. VI. Cosmological parameters," arXiv:1807.06209 [astro-ph.CO].

[21] **XENON** Collaboration, E. Aprile *et al.*, "Dark Matter Search Results from a One Ton-Year Exposure of XENON1T," *Phys.Rev.Lett.* **121** (2018) 111302, arXiv:1805.12562 [astro-ph.CO].

[22] **LUX-ZEPLIN** Collaboration, D. S. Akerib *et al.*, "Projected WIMP Sensitivity of the LUX-ZEPLIN (LZ) Dark Matter Experiment," arXiv:1802.06039 [astro-ph.IM].

[23] **Fermi-LAT** Collaboration, M. Ackermann *et al.*, "Searching for Dark Matter Annihilation from Milky Way Dwarf Spheroidal Galaxies with Six Years of Fermi Large Area Telescope Data," *Phys.Rev.Lett.* **115** (2015) 231301, arXiv:1503.02641 [astro-ph.HE].

[24] **H.E.S.S.** Collaboration, H. Abdallah *et al.*, "Search for dark matter annihilations towards the inner Galactic halo from 10 years of observations with H.E.S.S," *Phys.Rev.Lett.* **117** (2016) 111301, arXiv:1607.08142 [astro-ph.HE].

[25] **Fermi-LAT** Collaboration, E. Charles *et al.*, "Sensitivity Projections for Dark Matter Searches with the Fermi Large Area Telescope," *Phys.Rept.* **636** (2016) 1–46, arXiv:1605.02016 [astro-ph.HE].

[26] **CTA Consortium** Collaboration, B. Acharya *et al.*, *Science with the Cherenkov Telescope Array*. 2017. arXiv:1709.07997 [astro-ph.IM].

[27] **ATLAS** Collaboration, M. Aaboud *et al.*, "Search for new phenomena in final states with an energetic jet and large missing transverse momentum in pp collisions at $\sqrt{s} = 13$ TeV using the ATLAS detector," *Phys.Rev.* **D94** (2016) 032005, arXiv:1604.07773 [hep-ex].

[28] M. Bauer and T. Plehn, "Yet Another Introduction to Dark Matter," *Lect.Notes Phys.* **959** (2019) pp.–, arXiv:1705.01987 [hep-ph].

[29] R. Pathria, *Statistical Mechanics*.

[30] H. Mo, F. C. van den Bosch, and S. White, *Galaxy Formation and Evolution*. 2010.

[31] P. Gondolo and G. Gelmini, "Cosmic abundances of stable particles: Improved analysis," *Nucl.Phys.* **B360** (1991) 145–179.

[32] F. Reines and C. L. Cowan, "The neutrino," *Nature* **178** (1956) 446–449.

[33] Z. Maki, M. Nakagawa, Y. Ohnuki, and S. Sakata, "A unified model for elementary particles," *Prog.Theor.Phys.* **23** (1960) 1174–1180.

[34] Z. Maki, M. Nakagawa, and S. Sakata, "Remarks on the unified model of elementary particles," *Prog.Theor.Phys.* **28** (1962) 870–880.

[35] J. Valle, "Neutrino physics overview," vol. 53, pp. 473–505. 2006.

[36] J. Valle, "Neutrino masses: evidences and implications," vol. 485, p. 012005. 2014.

[37] R. Mohapatra *et al.*, "Theory of neutrinos: A White paper," *Rept.Prog.Phys.* **70** (2007) 1757–1867.

[38] E. Majorana, "Teoria simmetrica dell'elettrone e del positrone," *Nuovo Cim.* **14** (1937) 171–184.

[39] J. Schechter and J. Valle, "Neutrino Masses in SU(2) x U(1) Theories," *Phys.Rev.* **D22** (1980) 2227.

[40] J. Schechter and J. Valle, "Neutrinoless Double beta Decay in SU(2) x U(1) Theories," *Phys.Rev.* **D25** (1982) 2951.

[41] W. Konetschny and W. Kummer, "Nonconservation of Total Lepton Number with Scalar Bosons," *Phys.Lett.* **B70** (1977) 433–435.

[42] T. Cheng and L.-F. Li, "Neutrino Masses, Mixings and Oscillations in SU(2) x U(1) Models of Electroweak Interactions," *Phys.Rev.* **D22** (1980) 2860.

[43] R. N. Mohapatra and G. Senjanovic, "Neutrino Mass and Spontaneous Parity Nonconservation," *Phys.Rev.Lett.* **44** (1980) 912.

[44] R. N. Mohapatra and G. Senjanovic, "Neutrino Masses and Mixings in Gauge Models with Spontaneous Parity Violation," *Phys.Rev.* **D23** (1981) 165.

[45] S. Weinberg, "Baryon and Lepton Nonconserving Processes," *Phys.Rev.Lett.* **43** (1979) 1566–1570.

[46] M. Gell-Mann, P. Ramond, and R. Slansky, "Complex Spinors and Unified Theories," vol. C790927, pp. 315–321. 1979. arXiv:1306.4669 [hep-th].

[47] G. Lazarides, Q. Shafi, and C. Wetterich, "Proton Lifetime and Fermion Masses in an SO(10) Model," *Nucl.Phys.* **B181** (1981) 287–300.

[48] R. Foot, H. Lew, X. He, and G. C. Joshi, "Seesaw Neutrino Masses Induced by a Triplet of Leptons," *Z.Phys.* **C44** (1989) 441.

[49] V. C. Rubin and J. Ford, W.Kent, "Rotation of the Andromeda Nebula from a Spectroscopic Survey of Emission Regions," *Astrophys.J.* **159** (1970) 379–403.

[50] A. Bosma, "21-cm line studies of spiral galaxies. 2. The distribution and kinematics of neutral hydrogen in spiral galaxies of various morphological types.," *Astron.J.* **86** (1981) 1825.

[51] T. van Albada, J. N. Bahcall, K. Begeman, and R. Sancisi, "The Distribution of Dark Matter in the Spiral Galaxy NGC-3198," *Astrophys.J.* **295** (1985) 305–313.

[52] F. Zwicky, "Die Rotverschiebung von extragalaktischen Nebeln," *Helv.Phys.Acta* **6** (1933) 110–127.

[53] F. Zwicky, "On the Masses of Nebulae and of Clusters of Nebulae," *Astrophys.J.* **86** (1937) 217–246.

[54] **WMAP** Collaboration, G. Hinshaw *et al.*, "Nine-Year Wilkinson Microwave Anisotropy Probe (WMAP) Observations: Cosmological Parameter Results," *Astrophys.J.Suppl.* **208** (2013) 19, arXiv:1212.5226 [astro-ph.CO].

[55] J. Dunkley *et al.*, "The Atacama Cosmology Telescope: Cosmological Parameters from the 2008 Power Spectra," *Astrophys.J.* **739** (2011) 52, arXiv:1009.0866 [astro-ph.CO].

[56] D. Fixsen, E. Cheng, J. Gales, J. C. Mather, R. Shafer, and E. Wright, "The Cosmic Microwave Background spectrum from the full COBE FIRAS data set," *Astrophys.J.* **473** (1996) 576.

[57] K. Bondarenko, A. Boyarsky, T. Bringmann, and A. Sokolenko, "Constraining self-interacting dark matter with scaling laws of observed halo surface densities," *JCAP* **1804** (2018) 049, arXiv:1712.06602 [astro-ph.CO].

[58] M. R. Buckley and P. J. Fox, "Dark Matter Self-Interactions and Light Force Carriers," *Phys.Rev.* **D81** (2010) 083522, arXiv:0911.3898 [hep-ph].

[59] P. de Salas, D. Forero, C. Ternes, M. Tortola, and J. Valle, "Status of neutrino oscillations 2018: 3σ hint for normal mass ordering and improved CP sensitivity," *Phys.Lett.* **B782** (2018) 633–640, arXiv:1708.01186 [hep-ph].

[60] G. Bertone and M. Tait, Tim, "A new era in the search for dark matter," *Nature* **562** (2018) 51–56, arXiv:1810.01668 [astro-ph.CO].

[61] V. Rubakov, "Cosmology and Dark Matter," 2019. arXiv:1912.04727 [hep-ph].

[62] F. D. Steffen, *Gravitino dark matter and cosmological constraints*. PhD thesis, 2006.

[63] A. Ringwald, "Exploring the Role of Axions and Other WISPs in the Dark Universe," *Phys.Dark Univ.* **1** (2012) 116–135, arXiv:1210.5081 [hep-ph].

[64] E. W. Kolb, D. J. Chung, and A. Riotto, "WIMPzillas!," vol. 484, pp. 91–105. 1999.

[65] Q. Zhu, E. Vasiliev, Y. Li, and Y. Jing, "Primordial Black Holes as Dark Matter: Constraints From Compact Ultra-Faint Dwarfs," *Mon.Not.Roy.Astron.Soc.* **476** (2018) 2–11, arXiv:1710.05032 [astro-ph.CO].

[66] G. Bertone, D. Hooper, and J. Silk, "Particle dark matter: Evidence, candidates and constraints," *Phys.Rept.* **405** (2005) 279–390.

[67] J. L. Feng, "Dark Matter Candidates from Particle Physics and Methods of Detection," *Ann.Rev.Astron.Astrophys.* **48** (2010) 495–545, arXiv:1003.0904 [astro-ph.CO].

[68] D. G. Cerdeno and A. M. Green, "Direct detection of WIMPs," arXiv:1002.1912 [astro-ph.CO].

[69] **CRESST** Collaboration, F. Petricca *et al.*, "First results on low-mass dark matter from the CRESST-III experiment," 2017. arXiv:1711.07692 [astro-ph.CO].

[70] G. Angloher *et al.*, "Results from 730 kg days of the CRESST-II Dark Matter Search," *Eur.Phys.J.* **C72** (2012) 1971, arXiv:1109.0702 [astro-ph.CO].

[71] **CDMS** Collaboration, Z. Ahmed *et al.*, "Search for Weakly Interacting Massive Particles with the First Five-Tower Data from the Cryogenic Dark Matter Search at the Soudan Underground Laboratory," *Phys.Rev.Lett.* **102** (2009) 011301, arXiv:0802.3530 [astro-ph].

[72] **CDMS-II** Collaboration, Z. Ahmed *et al.*, "Dark Matter Search Results from the CDMS II Experiment," *Science* **327** (2010) 1619–1621, arXiv:0912.3592 [astro-ph.CO].

[73] **CDMS-II** Collaboration, Z. Ahmed *et al.*, "Results from a Low-Energy Analysis of the CDMS II Germanium Data," *Phys.Rev.Lett.* **106** (2011) 131302, arXiv:1011.2482 [astro-ph.CO].

[74] **CDMS** Collaboration, R. Agnese *et al.*, "Silicon Detector Dark Matter Results from the Final Exposure of CDMS II," *Phys.Rev.Lett.* **111** (2013) 251301, arXiv:1304.4279 [hep-ex].

[75] **SuperCDMS** Collaboration, R. Agnese *et al.*, "Search for Low-Mass Dark Matter with CDMSlite Using a Profile Likelihood Fit," *Phys.Rev.* **D99** (2019) 062001, arXiv:1808.09098 [astro-ph.CO].

[76] **SuperCDMS** Collaboration, R. Agnese *et al.*, "First Dark Matter Constraints from a SuperCDMS Single-Charge Sensitive Detector," *Phys.Rev.Lett.* **121** (2018) 051301, arXiv:1804.10697 [hep-ex].

[77] **SuperCDMS** Collaboration, R. Agnese *et al.*, "Projected Sensitivity of the SuperCDMS SNOLAB experiment," *Phys.Rev.* **D95** (2017) 082002, arXiv:1610.00006 [physics.ins-det].

[78] **LUX** Collaboration, D. Akerib *et al.*, "The Large Underground Xenon (LUX) Experiment," *Nucl.Instrum.Meth.* **A704** (2013) 111–126, arXiv:1211.3788 [physics.ins-det].

[79] **XENON** Collaboration, E. Aprile *et al.*, "Light Dark Matter Search with Ionization Signals in XENON1T," *Phys.Rev.Lett.* **123** (2019) 251801, arXiv:1907.11485 [hep-ex].

[80] **XENON** Collaboration, E. Aprile *et al.*, "The XENON1T Data Acquisition System," *JINST* **14** (2019) P07016, arXiv:1906.00819 [physics.ins-det].

[81] **XENON** Collaboration, J. Angle *et al.*, "First Results from the XENON10 Dark Matter Experiment at the Gran Sasso National Laboratory," *Phys.Rev.Lett.* **100** (2008) 021303, arXiv:0706.0039 [astro-ph].

[82] **XENON100** Collaboration, E. Aprile *et al.*, "Dark Matter Results from 100 Live Days of XENON100 Data," *Phys.Rev.Lett.* **107** (2011) 131302, arXiv:1104.2549 [astro-ph.CO].

[83] **XENON100** Collaboration, E. Aprile *et al.*, "Dark Matter Results from 225 Live Days of XENON100 Data," *Phys.Rev.Lett.* **109** (2012) 181301, arXiv:1207.5988 [astro-ph.CO].

[84] **PandaX-II** Collaboration, J. Xia *et al.*, "PandaX-II Constraints on Spin-Dependent WIMP-Nucleon Effective Interactions," *Phys.Lett.* **B792** (2019) 193–198, arXiv:1807.01936 [hep-ex].

[85] **PandaX-II** Collaboration, X. Cui *et al.*, "Dark Matter Results From 54-Ton-Day Exposure of PandaX-II Experiment," *Phys.Rev.Lett.* **119** (2017) 181302, arXiv:1708.06917 [astro-ph.CO].

[86] D. Akimov *et al.*, "The ZEPLIN-III dark matter detector: instrument design, manufacture and commissioning," *Astropart.Phys.* **27** (2007) 46–60.

[87] **DarkSide** Collaboration, P. Agnes *et al.*, "Low-Mass Dark Matter Search with the DarkSide-50 Experiment," *Phys.Rev.Lett.* **121** (2018) 081307, arXiv:1802.06994 [astro-ph.HE].

[88] C. Aalseth *et al.*, "DarkSide-20k: A 20 tonne two-phase LAr TPC for direct dark matter detection at LNGS," *Eur.Phys.J.Plus* **133** (2018) 131, arXiv:1707.08145 [physics.ins-det].

[89] **DarkSide** Collaboration, P. Agnes *et al.*, "First Results from the DarkSide-50 Dark Matter Experiment at Laboratori Nazionali del Gran Sasso," *Phys.Lett.* **B743** (2015) 456–466, arXiv:1410.0653 [astro-ph.CO].

[90] A. Badertscher *et al.*, "ArDM: first results from underground commissioning," *JINST* **8** (2013) C09005, arXiv:1309.3992 [physics.ins-det].

[91] A. Rubbia, "ArDM: A Ton-scale liquid Argon experiment for direct detection of dark matter in the universe," vol. 39, pp. 129–132. 2006.

[92] **WARP** Collaboration, R. Brunetti *et al.*, "Warp liquid argon detector for dark matter survey," vol. 49, pp. 265–269. 2005.

[93] **PICO** Collaboration, C. Amole *et al.*, "Dark Matter Search Results from the Complete Exposure of the PICO-60 C_3F_8 Bubble Chamber," *Phys.Rev.* **D100** (2019) 022001, arXiv:1902.04031 [astro-ph.CO].

[94] **PICO** Collaboration, C. Amole *et al.*, "Dark matter search results from the PICO-60 CF_3I bubble chamber," *Phys.Rev.* **D93** (2016) 052014, arXiv:1510.07754 [hep-ex].

[95] **PICO** Collaboration, C. Amole *et al.*, "Dark Matter Search Results from the PICO-2L C_3F_8 Bubble Chamber," *Phys.Rev.Lett.* **114** (2015) 231302, arXiv:1503.00008 [astro-ph.CO].

[96] R. Bernabei *et al.*, "First Model Independent Results from DAMA/LIBRA–Phase2," vol. 4, p. 116. 2018. arXiv:1805.10486 [hep-ex].

[97] R. Cerulli *et al.*, "DAMA annual modulation and mirror Dark Matter," *Eur.Phys.J.* **C77** (2017) 83, arXiv:1701.08590 [hep-ex].

[98] R. Bernabei, "The DAMA project," *Int.J.Mod.Phys.* **A31** (2016) 1642001.

[99] **DAMA** Collaboration, R. Bernabei *et al.*, "First results from DAMA/LIBRA and the combined results with DAMA/NaI," *Eur.Phys.J.* **C56** (2008) 333–355, arXiv:0804.2741 [astro-ph].

[100] **CoGeNT** Collaboration, C. Aalseth *et al.*, "Results from a Search for Light-Mass Dark Matter with a P-type Point Contact Germanium Detector," *Phys.Rev.Lett.* **106** (2011) 131301, arXiv:1002.4703 [astro-ph.CO].

[101] C. Aalseth *et al.*, "Search for an Annual Modulation in a P-type Point Contact Germanium Dark Matter Detector," *Phys.Rev.Lett.* **107** (2011) 141301, arXiv:1106.0650 [astro-ph.CO].

[102] **XENON** Collaboration, E. Aprile *et al.*, "XENON1T dark matter data analysis: Signal and background models and statistical inference," *Phys.Rev.* **D99** (2019) 112009, arXiv:1902.11297 [physics.ins-det].

[103] **XENON1T** Collaboration, E. Aprile, "The XENON1T Dark Matter Search Experiment," vol. 148, pp. 93–96. 2013. arXiv:1206.6288 [astro-ph.IM].

[104] **LUX-ZEPLIN** Collaboration, D. S. Akerib *et al.*, "Projected WIMP Sensitivity of the LUX-ZEPLIN (LZ) Dark Matter Experiment," arXiv:1802.06039 [astro-ph.IM].

[105] R. Bernabei *et al.*, "Dama/libra Results and Perspectives," pp. 318–327. 2019.

[106] R. Bernabei *et al.*, "Dark Matter investigation by DAMA at Gran Sasso," *Int.J.Mod.Phys.* **A28** (2013) 1330022, arXiv:1306.1411 [astro-ph.GA].

[107] R. Bernabei *et al.*, "New limits on WIMP search with large-mass low-radioactivity NaI(Tl) set-up at Gran Sasso," *Phys.Lett.* **B389** (1996) 757–766.

[108] R. Bernabei *et al.*, "Dark matter particles in the Galactic halo: Results and implications from DAMA/NaI," *Int.J.Mod.Phys.* **D13** (2004) 2127–2160.

[109] **DAMA** Collaboration, R. Bernabei *et al.*, "New results from DAMA/LIBRA," *Eur.Phys.J.* **C67** (2010) 39–49, arXiv:1002.1028 [astro-ph.GA].

[110] R. Bernabei *et al.*, "Final model independent result of DAMA/LIBRA-phase1," *Eur.Phys.J.* **C73** (2013) 2648, arXiv:1308.5109 [astro-ph.GA].

[111] R. Bernabei *et al.*, "Searching for WIMPs by the annual modulation signature," *Phys.Lett.* **B424** (1998) 195–201.

[112] **DAMA** Collaboration, R. Bernabei *et al.*, "On a further search for a yearly modulation of the rate in particle dark matter direct search," *Phys.Lett.* **B450** (1999) 448–455.

[113] **DAMA** Collaboration, R. Bernabei *et al.*, "Search for WIMP annual modulation signature: Results from DAMA / NaI-3 and DAMA / NaI-4 and the global combined analysis," *Phys.Lett.* **B480** (2000) 23–31.

[114] M. Farina, D. Pappadopulo, A. Strumia, and T. Volansky, "Can CoGeNT and DAMA Modulations Be Due to Dark Matter?," *JCAP* **1111** (2011) 010, arXiv:1107.0715 [hep-ph].

[115] M. T. Frandsen, F. Kahlhoefer, C. McCabe, S. Sarkar, and K. Schmidt-Hoberg, "Resolving astrophysical uncertainties in dark matter direct detection," *JCAP* **1201** (2012) 024, arXiv:1111.0292 [hep-ph].

[116] J. Herrero-Garcia, T. Schwetz, and J. Zupan, "Astrophysics independent bounds on the annual modulation of dark matter signals," *Phys.Rev.Lett.* **109** (2012) 141301, arXiv:1205.0134 [hep-ph].

[117] J. Amare *et al.*, "Assessment of backgrounds of the ANAIS experiment for dark matter direct detection," *Eur.Phys.J.* **C76** (2016) 429, arXiv:1604.05587 [astro-ph.IM].

[118] J. Amaré *et al.*, "Performance of ANAIS-112 experiment after the first year of data taking," *Eur.Phys.J.* **C79** (2019) 228, arXiv:1812.01472 [astro-ph.IM].

[119] J. Amaré *et al.*, "First Results on Dark Matter Annual Modulation from the ANAIS-112 Experiment," *Phys.Rev.Lett.* **123** (2019) 031301, arXiv:1903.03973 [astro-ph.IM].

[120] **COSINE-100** Collaboration, G. Adhikari *et al.*, "Search for a Dark Matter-Induced Annual Modulation Signal in NaI(Tl) with the COSINE-100 Experiment," *Phys.Rev.Lett.* **123** (2019) 031302, arXiv:1903.10098 [astro-ph.IM].

[121] **COSINE-100** Collaboration, G. Adhikari *et al.*, "COSINE-100 and DAMA/LIBRA-phase2 in WIMP effective models," *JCAP* **1906** (2019) 048, arXiv:1904.00128 [hep-ph].

[122] G. Tomar, S. Kang, S. Scopel, and J.-H. Yoon, "Is a WIMP explanation of the DAMA modulation effect still viable?," 2019. arXiv:1911.12601 [hep-ph].

[123] **COSINE-100** Collaboration, W. Thompson, "Current status and projected sensitivity of COSINE-100," vol. 1342, p. 012134. 2020. arXiv:1711.01488 [physics.ins-det].

[124] **DM-Ice** Collaboration, E. Barbosa de Souza *et al.*, "First search for a dark matter annual modulation signal with NaI(Tl) in the Southern Hemisphere by DM-Ice17," *Phys.Rev.* **D95** (2017) 032006, arXiv:1602.05939 [physics.ins-det].

[125] **KIMS** Collaboration, K. Kim *et al.*, "Limits on Interactions between Weakly Interacting Massive Particles and Nucleons Obtained with NaI(Tl) crystal Detectors," *JHEP* **1903** (2019) 194, arXiv:1806.06499 [hep-ex].

[126] E. Majorana, "Teoria simmetrica dell'elettrone e del positrone," *Nuovo Cim.* **14** (1937) 171–184.

[127] J. Cembranos, A. de la Cruz-Dombriz, A. Dobado, R. Lineros, and A. Maroto, "Photon spectra from WIMP annihilation," *Phys.Rev.* **D83** (2011) 083507, arXiv:1009.4936 [hep-ph].

[128] T. Bringmann, L. Bergstrom, and J. Edsjo, "New Gamma-Ray Contributions to Supersymmetric Dark Matter Annihilation," *JHEP* **0801** (2008) 049, arXiv:0710.3169 [hep-ph].

[129] F. Giacchino, L. Lopez-Honorez, and M. H. Tytgat, "Scalar Dark Matter Models with Significant Internal Bremsstrahlung," *JCAP* **1310** (2013) 025, arXiv:1307.6480 [hep-ph].

[130] Bošnjak, Ž. and Daigne, F. and Dubus, G., "Prompt high-energy emission from gamma-ray bursts in the internal shock model," *aap* **498** no. 3, (May, 2009) 677–703, arXiv:0811.2956 [astro-ph].

[131] M. Cirelli, P. D. Serpico, and G. Zaharijas, "Bremsstrahlung gamma rays from light Dark Matter," *JCAP* **1311** (2013) 035, arXiv:1307.7152 [astro-ph.HE].

[132] R. Catena and P. Ullio, "A novel determination of the local dark matter density," *JCAP* **1008** (2010) 004, arXiv:0907.0018 [astro-ph.CO].

[133] J. Read, "The Local Dark Matter Density," *J.Phys.* **G41** (2014) 063101, arXiv:1404.1938 [astro-ph.GA].

[134] **H.E.S.S.** Collaboration, F. Aharonian *et al.*, "H.E.S.S. observations of the Galactic Center region and their possible dark matter interpretation," *Phys.Rev.Lett.* **97** (2006) 221102.

[135] K. N. Abazajian and J. Harding, "Constraints on WIMP and Sommerfeld-Enhanced Dark Matter Annihilation from HESS Observations of the Galactic Center," *JCAP* **1201** (2012) 041, arXiv:1110.6151 [hep-ph].

[136] **Fermi-LAT** Collaboration, M. Ackermann *et al.*, "Anisotropies in the diffuse gamma-ray background measured by the Fermi LAT," *Phys.Rev.* **D85** (2012) 083007, arXiv:1202.2856 [astro-ph.HE].

[137] A. Cuoco, J.-Q. Xia, M. Regis, E. Branchini, N. Fornengo, and M. Viel, "Dark Matter Searches in the Gamma-ray Extragalactic Background via Cross-correlations With Galaxy Catalogs," *Astrophys.J.Suppl.* **221** (2015) 29, arXiv:1506.01030 [astro-ph.HE].

[138] **H.E.S.S.** Collaboration, F. Aharonian, "Observations of the Sagittarius Dwarf galaxy by the H.E.S.S. experiment and search for a Dark Matter signal," *Astropart.Phys.* **29** (2008) 55–62, arXiv:0711.2369 [astro-ph].

[139] **H.E.S.S.** Collaboration, A. Abramowski *et al.*, "H.E.S.S. constraints on Dark Matter annihilations towards the Sculptor and Carina Dwarf Galaxies," *Astropart.Phys.* **34** (2011) 608–616, arXiv:1012.5602 [astro-ph.HE].

[140] **VERITAS** Collaboration, K. Kosack *et al.*, "TeV gamma-ray observations of the galactic center," *Astrophys.J.* **608** (2004) L97–L100.

[141] **VERITAS** Collaboration, J. Perkins, "VERITAS Observations of the Coma Cluster of Galaxies," vol. 1085, pp. 569–572. 2009. arXiv:0810.0302 [astro-ph].

[142] **VERITAS** Collaboration, V. Acciari *et al.*, "VERITAS Search for VHE Gamma-ray Emission from Dwarf Spheroidal Galaxies," *Astrophys.J.* **720** (2010) 1174–1180, arXiv:1006.5955 [astro-ph.CO].

[143] **VERITAS** Collaboration, E. Aliu *et al.*, "VERITAS Deep Observations of the Dwarf Spheroidal Galaxy Segue 1," *Phys.Rev.* **D85** (2012) 062001, arXiv:1202.2144 [astro-ph.HE].

[144] **Fermi-LAT** Collaboration, M. Ackermann *et al.*, "Constraining Dark Matter Models from a Combined Analysis of Milky Way Satellites with the Fermi Large Area Telescope," *Phys.Rev.Lett.* **107** (2011) 241302, arXiv:1108.3546 [astro-ph.HE].

[145] **Fermi-LAT** Collaboration, A. Abdo *et al.*, "Observations of Milky Way Dwarf Spheroidal galaxies with the Fermi-LAT detector and constraints on Dark Matter models," *Astrophys.J.* **712** (2010) 147–158, arXiv:1001.4531 [astro-ph.CO].

[146] **Fermi-LAT** Collaboration, A. Abdo *et al.*, "The Spectrum of the Isotropic Diffuse Gamma-Ray Emission Derived From First-Year Fermi Large Area Telescope Data," *Phys.Rev.Lett.* **104** (2010) 101101, arXiv:1002.3603 [astro-ph.HE].

[147] **Fermi-LAT** Collaboration, M. Ackermann *et al.*, "Constraints on the Galactic Halo Dark Matter from Fermi-LAT Diffuse Measurements," *Astrophys.J.* **761** (2012) 91, arXiv:1205.6474 [astro-ph.CO].

[148] A. Abdo *et al.*, "Fermi LAT Search for Photon Lines from 30 to 200 GeV and Dark Matter Implications," *Phys.Rev.Lett.* **104** (2010) 091302, arXiv:1001.4836 [astro-ph.HE].

[149] **Fermi-LAT** Collaboration, M. Ackermann *et al.*, "Fermi LAT Search for Dark Matter in Gamma-ray Lines and the Inclusive Photon Spectrum," *Phys.Rev.* **D86** (2012) 022002, arXiv:1205.2739 [astro-ph.HE].

[150] **Fermi-LAT** Collaboration, M. Ackermann *et al.*, "Search for Gamma-ray Spectral Lines with the Fermi Large Area Telescope and Dark Matter Implications," *Phys.Rev.* **D88** (2013) 082002, arXiv:1305.5597 [astro-ph.HE].

[151] C. Weniger, "A Tentative Gamma-Ray Line from Dark Matter Annihilation at the Fermi Large Area Telescope," *JCAP* **1208** (2012) 007, arXiv:1204.2797 [hep-ph].

[152] T. Bringmann, X. Huang, A. Ibarra, S. Vogl, and C. Weniger, "Fermi LAT Search for Internal Bremsstrahlung Signatures from Dark Matter Annihilation," *JCAP* **1207** (2012) 054, arXiv:1203.1312 [hep-ph].

[153] F. Aharonian, D. Khangulyan, and D. Malyshev, "Cold ultrarelativistic pulsar winds as potential sources of galactic gamma-ray lines above 100 GeV," *Astron.Astrophys.* **547** (2012) A114, arXiv:1207.0458 [astro-ph.HE].

[154] **Fermi-LAT** Collaboration, M. Ackermann *et al.*, "The Fermi Galactic Center GeV Excess and Implications for Dark Matter," *Astrophys.J.* **840** (2017) 43, arXiv:1704.03910 [astro-ph.HE].

[155] Carlberg, R. G. and Yee, H. K. C. and Morris, S. L. and Lin, H. and Ellingson, E. and Patton, D. and Sawicki, M. and Shepherd, C. W., "The Ω_M-Ω_Λ Dependence of the Apparent Cluster Ω," *Apj* **516** no. 2, (May, 1999) 552–558.

[156] R. Bartels, S. Krishnamurthy, and C. Weniger, "Strong support for the millisecond pulsar origin of the Galactic center GeV excess," *Phys.Rev.Lett.* **116** (2016) 051102, arXiv:1506.05104 [astro-ph.HE].

[157] S. K. Lee, M. Lisanti, B. R. Safdi, T. R. Slatyer, and W. Xue, "Evidence for Unresolved γ-Ray Point Sources in the Inner Galaxy," *Phys.Rev.Lett.* **116** (2016) 051103, arXiv:1506.05124 [astro-ph.HE].

[158] **Fermi-LAT** Collaboration, M. Ajello *et al.*, "Characterizing the population of pulsars in the inner Galaxy with the Fermi Large Area Telescope," *Astrophys.J.* (2017) , arXiv:1705.00009 [astro-ph.HE].

[159] W. R. Purcell, D. A. Grabelsky, M. P. Ulmer, W. N. Johnson, R. L. Kinzer, J. D. Kurfess, M. S. Strickman, and G. V. Jung, "OSSE Observations of Galactic 511 keV Positron Annihilation Radiation: Initial Phase 1 Results," *ApJL* **413** (Aug, 1993) L85.

[160] M. Leventhal, C. J. MacCallum, and P. D. Stang, "Detection of 511 keV positron annihilation radiation from the galactic center direction.," *ApJL* **225** (Oct, 1978) L11–L14.

[161] C. Boehm, D. Hooper, J. Silk, M. Casse, and J. Paul, "MeV dark matter: Has it been detected?," *Phys.Rev.Lett.* **92** (2004) 101301.

[162] Y. Ascasibar, P. Jean, C. Boehm, and J. Knoedlseder, "Constraints on dark matter and the shape of the Milky Way dark halo from the 511-keV line," *Mon.Not.Roy.Astron.Soc.* **368** (2006) 1695–1705.

[163] R. J. Wilkinson, A. C. Vincent, C. Bœhm, and C. McCabe, "Ruling out the light weakly interacting massive particle explanation of the Galactic 511 keV line," *Phys.Rev.* **D94** (2016) 103525, arXiv:1602.01114 [astro-ph.CO].

[164] M. Regis, L. Richter, and S. Colafrancesco, "Dark matter in the Reticulum II dSph: a radio search," *JCAP* **1707** (2017) 025, arXiv:1703.09921 [astro-ph.HE].

[165] E. Bulbul, M. Markevitch, A. Foster, R. K. Smith, M. Loewenstein, and S. W. Randall, "Detection of An Unidentified Emission Line in the Stacked X-ray spectrum of Galaxy Clusters," *Astrophys.J.* **789** (2014) 13, arXiv:1402.2301 [astro-ph.CO].

[166] T. E. Jeltema and S. Profumo, "Discovery of a 3.5 keV line in the Galactic Centre and a critical look at the origin of the line across astronomical targets," *Mon.Not.Roy.Astron.Soc.* **450** (2015) 2143–2152, arXiv:1408.1699 [astro-ph.HE].

[167] J. P. Conlon and F. V. Day, "3.55 keV photon lines from axion to photon conversion in the Milky Way and M31," *JCAP* **1411** (2014) 033, arXiv:1404.7741 [hep-ph].

[168] D. Fixsen *et al.*, "ARCADE 2 Measurement of the Extra-Galactic Sky Temperature at 3-90 GHz," *Astrophys.J.* **734** (2011) 5, arXiv:0901.0555 [astro-ph.CO].

[169] N. Fornengo, R. Lineros, M. Regis, and M. Taoso, "Possibility of a Dark Matter Interpretation for the Excess in Isotropic Radio Emission Reported by ARCADE," *Phys.Rev.Lett.* **107** (2011) 271302, arXiv:1108.0569 [hep-ph].

[170] J. Singal *et al.*, "The Radio Synchrotron Background: Conference Summary and Report," *Publ.Astron.Soc.Pac.* **130** (2018) 036001, arXiv:1711.09979 [astro-ph.HE].

[171] V. Barger, W. Y. Keung, D. Marfatia, and G. Shaughnessy, "PAMELA and dark matter," *Phys.Lett.* **B672** (2009) 141–146, arXiv:0809.0162 [hep-ph].

[172] M. Cirelli and G. Giesen, "Antiprotons from Dark Matter: Current constraints and future sensitivities," *JCAP* **1304** (2013) 015, arXiv:1301.7079 [hep-ph].

[173] F. S. Queiroz, "Dark Matter Overview: Collider, Direct and Indirect Detection Searches," in *Proceedings, 51st Rencontres de Moriond on Electroweak Interactions and Unified Theories: La Thuile, Italy, March 12-19, 2016*, pp. 427–436, ARISF. ARISF, 2016. arXiv:1605.08788 [hep-ph].

[174] **CMS** Collaboration, "Search for dark matter and graviton produced in association with a photon in pp collisions at sqrts = 13 TeV,".

[175] **CMS** Collaboration, "Search for dark matter in final states with an energetic jet, or a hadronically decaying W or Z boson using 12.9 fb^{-1} of data at $\sqrt{s} = 13$ TeV,".

[176] **ATLAS** Collaboration, M. Aaboud *et al.*, "Search for dark matter produced in association with a hadronically decaying vector boson in *pp* collisions at $\sqrt{s} = 13$ TeV with the ATLAS detector," *Phys.Lett.* **B763** (2016) 251–268, arXiv:1608.02372 [hep-ex].

[177] **ATLAS** Collaboration, M. Aaboud *et al.*, "Search for new phenomena in events with a photon and missing transverse momentum in *pp* collisions at $\sqrt{s} = 13$ TeV with the ATLAS detector," *JHEP* **1606** (2016) 059, arXiv:1604.01306 [hep-ex].

[178] N. F. Bell, J. B. Dent, A. J. Galea, T. D. Jacques, L. M. Krauss, and T. J. Weiler, "Searching for Dark Matter at the LHC with a Mono-Z," *Phys.Rev.* **D86** (2012) 096011, arXiv:1209.0231 [hep-ph].

[179] N. F. Bell, Y. Cai, and R. K. Leane, "Mono-W Dark Matter Signals at the LHC: Simplified Model Analysis," *JCAP* **1601** (2016) 051, arXiv:1512.00476 [hep-ph].

[180] **ATLAS** Collaboration, J. H. Lindon, "Searches for dark matter and dark energy produced in association with a jet with the ATLAS detector," vol. LeptonPhoton2019, p. 159. 2019.

[181] **CMS** Collaboration, A. M. Sirunyan *et al.*, "Search for dark matter particles produced in association with a Higgs boson in proton-proton collisions at $\sqrt{s} = 13$ TeV," arXiv:1908.01713 [hep-ex].

[182] S. L. Glashow and S. Weinberg, "Natural Conservation Laws for Neutral Currents," *Phys.Rev.* **D15** (1977) 1958.

[183] I. F. Ginzburg and M. Krawczyk, "Symmetries of two Higgs doublet model and CP violation," *Phys.Rev.* **D72** (2005) 115013.

[184] I. Ivanov, "Minkowski space structure of the Higgs potential in 2HDM," *Phys.Rev.* **D75** (2007) 035001.

[185] E. Ma, "Verifiable radiative seesaw mechanism of neutrino mass and dark matter," *Phys.Rev.* **D73** (2006) 077301.

[186] J. Casas and A. Ibarra, "Oscillating neutrinos and muon —¿ e, gamma," *Nucl.Phys.* **B618** (2001) 171–204.

[187] M. Hirsch, R. Lineros, S. Morisi, J. Palacio, N. Rojas, and J. Valle, "WIMP dark matter as radiative neutrino mass messenger," *JHEP* **1310** (2013) 149, arXiv:1307.8134 [hep-ph].

[188] A. Merle, M. Platscher, N. Rojas, J. W. F. Valle, and A. Vicente, "Consistency of WIMP Dark Matter as radiative neutrino mass messenger," *JHEP* **1607** (2016) 013, arXiv:1603.05685 [hep-ph].

[189] M. A. Díaz, N. Rojas, S. Urrutia-Quiroga, and J. W. F. Valle, "Heavy Higgs Boson Production at Colliders in the Singlet-Triplet Scotogenic Dark Matter Model," *JHEP* **1708** (2017) 017, arXiv:1612.06569 [hep-ph].

[190] S. Choubey, S. Khan, M. Mitra, and S. Mondal, "Singlet-Triplet Fermionic Dark Matter and LHC Phenomenology," *Eur.Phys.J.* **C78** (2018) 302, arXiv:1711.08888 [hep-ph].

[191] D. Restrepo and A. Rivera, "Phenomenological consistency of the singlet-triplet scotogenic model," arXiv:1907.11938 [hep-ph].

[192] J. Gunion, R. Vega, and J. Wudka, "Higgs triplets in the standard model," *Phys.Rev.* **D42** (1990) 1673–1691.

[193] J. F. Gunion, H. E. Haber, G. L. Kane, and S. Dawson, "The Higgs Hunter's Guide," *Front.Phys.* **80** (2000) 1–404.

[194] G. 't Hooft, "Naturalness, chiral symmetry, and spontaneous chiral symmetry breaking," *NATO Sci. Ser. B* **59** (1980) 135–157.

[195] G. Passarino and M. Veltman, "One Loop Corrections for e+ e- Annihilation Into mu+ mu- in the Weinberg Model," *Nucl.Phys.* **B160** (1979) 151–207.

[196] W. Rodejohann and J. Valle, "Symmetrical Parametrizations of the Lepton Mixing Matrix," *Phys.Rev.* **D84** (2011) 073011, arXiv:1108.3484 [hep-ph].

[197] M. Reig, D. Restrepo, J. F. Valle, and O. Zapata, "Bound-state dark matter with Majorana neutrinos," *Phys.Lett.* **B790** (2019) 303–307, arXiv:1806.09977 [hep-ph].

[198] J. Leite, O. Popov, R. Srivastava, and J. W. Valle, "A theory for scotogenic dark matter stabilised by residual gauge symmetry," arXiv:1909.06386 [hep-ph].

[199] **CUORE** Collaboration, C. Alduino *et al.*, "First Results from CUORE: A Search for Lepton Number Violation via $0\nu\beta\beta$ Decay of ^{130}Te," *Phys.Rev.Lett.* **120** (2018) 132501, arXiv:1710.07988 [nucl-ex].

[200] **EXO** Collaboration, J. Albert *et al.*, "Search for Neutrinoless Double-Beta Decay with the Upgraded EXO-200 Detector," *Phys.Rev.Lett.* **120** (2018) 072701, arXiv:1707.08707 [hep-ex].

[201] **GERDA** Collaboration, M. Agostini *et al.*, "Improved Limit on Neutrinoless Double-β Decay of ^{76}Ge from GERDA Phase II," *Phys.Rev.Lett.* **120** (2018) 132503, arXiv:1803.11100 [nucl-ex].

[202] **KamLAND-Zen** Collaboration, A. Gando *et al.*, "Search for Majorana Neutrinos near the Inverted Mass Hierarchy Region with KamLAND-Zen," *Phys.Rev.Lett.* **117** (2016) 082503, arXiv:1605.02889 [hep-ex].

[203] **SNO+** Collaboration, S. Andringa *et al.*, "Current Status and Future Prospects of the SNO+ Experiment," *Adv.High Energy Phys.* **2016** (2016) 6194250, arXiv:1508.05759 [physics.ins-det].

[204] **LEGEND** Collaboration, N. Abgrall *et al.*, "The Large Enriched Germanium Experiment for Neutrinoless Double Beta Decay (LEGEND)," vol. 1894, p. 020027. 2017. arXiv:1709.01980 [physics.ins-det].

[205] **nEXO** Collaboration, J. Albert *et al.*, "Sensitivity and Discovery Potential of nEXO to Neutrinoless Double Beta Decay," *Phys.Rev.* **C97** (2018) 065503, arXiv:1710.05075 [nucl-ex].

[206] R. Bouchand and A. Merle, "Running of Radiative Neutrino Masses: The Scotogenic Model," *JHEP* **1207** (2012) 084, arXiv:1205.0008 [hep-ph].

[207] T. Toma and A. Vicente, "Lepton Flavor Violation in the Scotogenic Model," *JHEP* **1401** (2014) 160, arXiv:1312.2840 [hep-ph].

[208] P. Rocha-Moran and A. Vicente, "Lepton Flavor Violation in the singlet-triplet scotogenic model," *JHEP* **1607** (2016) 078, arXiv:1605.01915 [hep-ph].

[209] **MEG** Collaboration, A. Baldini *et al.*, "Search for the lepton flavour violating decay $\mu^+ \to e^+\gamma$ with the full dataset of the MEG experiment," *Eur.Phys.J.* **C76** (2016) 434, arXiv:1605.05081 [hep-ex].

[210] **SINDRUM** Collaboration, U. Bellgardt *et al.*, "Search for the Decay mu+ —¿ e+ e+ e-," *Nucl.Phys.* **B299** (1988) 1–6.

[211] **SINDRUM II** Collaboration, W. H. Bertl *et al.*, "A Search for muon to electron conversion in muonic gold," *Eur.Phys.J.* **C47** (2006) 337–346.

[212] M. E. Peskin and T. Takeuchi, "Estimation of oblique electroweak corrections," *Phys.Rev.* **D46** (1992) 381–409.

[213] **Particle Data Group** Collaboration, M. Tanabashi *et al.*, "Review of Particle Physics," *Phys.Rev.* **D98** (2018) 030001.

[214] A. Abada and T. Toma, "Electric Dipole Moments in the Minimal Scotogenic Model," *JHEP* **1804** (2018) 030, arXiv:1802.00007 [hep-ph].

[215] I. Maturana-Ávila, M. A. Díaz, N. Rojas, and S. Urrutia-Quiroga, "Towards a way to distinguish between IHDM and the Scotogenic at CLIC," 2019. arXiv:1903.11181 [hep-ph].

[216] W. Porod, "SPheno, a program for calculating supersymmetric spectra, SUSY particle decays and SUSY particle production at e+ e- colliders," *Comput.Phys.Commun.* **153** (2003) 275–315.

[217] W. Porod and F. Staub, "SPheno 3.1: Extensions including flavour, CP-phases and models beyond the MSSM," *Comput.Phys.Commun.* **183** (2012) 2458–2469, arXiv:1104.1573 [hep-ph].

[218] W. Porod, F. Staub, and A. Vicente, "A Flavor Kit for BSM models," *Eur.Phys.J.* **C74** (2014) 2992, arXiv:1405.1434 [hep-ph].

[219] F. Staub, "SARAH 4 : A tool for (not only SUSY) model builders," *Comput.Phys.Commun.* **185** (2014) 1773–1790, arXiv:1309.7223 [hep-ph].

[220] F. Staub, "Exploring new models in all detail with SARAH," *Adv.High Energy Phys.* **2015** (2015) 840780, arXiv:1503.04200 [hep-ph].

[221] G. Bélanger, F. Boudjema, A. Pukhov, and A. Semenov, "micrOMEGAs4.1: two dark matter candidates," *Comput.Phys.Commun.* **192** (2015) 322–329, arXiv:1407.6129 [hep-ph].

[222] I. M. Ávila, V. De Romeri, L. Duarte, and J. W. Valle, "Minimalistic scotogenic scalar dark matter," arXiv:1910.08422 [hep-ph].

[223] A. Merle and M. Platscher, "Running of radiative neutrino masses: the scotogenic model — revisited," *JHEP* **1511** (2015) 148, arXiv:1507.06314 [hep-ph].

[224] R. Bouchand and A. Merle, "Running of Radiative Neutrino Masses: The Scotogenic Model," *JHEP* **1207** (2012) 084, arXiv:1205.0008 [hep-ph].

[225] J. Alwall *et al.*, "The automated computation of tree-level and next-to-leading order differential cross sections, and their matching to parton shower simulations," *JHEP* **1407** (2014) 079, arXiv:1405.0301 [hep-ph].

[226] **CLIC** Collaboration, P. Roloff, R. Franceschini, U. Schnoor, and A. Wulzer, "The Compact Linear e^+e^- Collider (CLIC): Physics Potential," arXiv:1812.07986 [hep-ex].

[227] S. Blunier, G. Cottin, M. A. Díaz, and B. Koch, "Phenomenology of a Higgs triplet model at future e^+e^- colliders," *Phys.Rev.* **D95** (2017) 075038, arXiv:1611.07896 [hep-ph].

[228] T. Hambye, F.-S. Ling, L. Lopez Honorez, and J. Rocher, "Scalar Multiplet Dark Matter," *JHEP* **0907** (2009) 090, arXiv:0903.4010 [hep-ph].

[229] L. Lopez Honorez and C. E. Yaguna, "The inert doublet model of dark matter revisited," *JHEP* **1009** (2010) 046, arXiv:1003.3125 [hep-ph].

[230] M. A. Díaz, B. Koch, and S. Urrutia-Quiroga, "Constraints to Dark Matter from Inert Higgs Doublet Model," *Adv.High Energy Phys.* **2016** (2016) 8278375, arXiv:1511.04429 [hep-ph].

[231] **DEAP** Collaboration, R. Ajaj *et al.*, "Search for dark matter with a 231-day exposure of liquid argon using DEAP-3600 at SNOLAB," *Phys.Rev.* **D100** (2019) 022004, arXiv:1902.04048 [astro-ph.CO].

[232] A. Sommerfeld, "Über die Beugung und Bremsung der Elektronen," *Annalen der Physik* **403** (1931) 257–330.

[233] J. Hisano, S. Matsumoto, and M. M. Nojiri, "Explosive dark matter annihilation," *Phys.Rev.Lett.* **92** (2004) 031303.

[234] J. Hisano, S. Matsumoto, M. M. Nojiri, and O. Saito, "Non-perturbative effect on dark matter annihilation and gamma ray signature from galactic center," *Phys.Rev.* **D71** (2005) 063528.

[235] N. Arkani-Hamed, D. P. Finkbeiner, T. R. Slatyer, and N. Weiner, "A Theory of Dark Matter," *Phys.Rev.* **D79** (2009) 015014, arXiv:0810.0713 [hep-ph].

[236] T. A. Chowdhury and S. Nasri, "The Sommerfeld Enhancement in the Scotogenic Model with Large Electroweak Scalar Multiplets," *JCAP* **1701** (2017) 041, arXiv:1611.06590 [hep-ph].

[237] **PAMELA** Collaboration, O. Adriani *et al.*, "An anomalous positron abundance in cosmic rays with energies 1.5-100 GeV," *Nature* **458** (2009) 607–609, arXiv:0810.4995 [astro-ph].

[238] **PAMELA** Collaboration, O. Adriani *et al.*, "Cosmic-Ray Positron Energy Spectrum Measured by PAMELA," *Phys.Rev.Lett.* **111** (2013) 081102, arXiv:1308.0133 [astro-ph.HE].

[239] **AMS** Collaboration, M. Aguilar *et al.*, "First Result from the Alpha Magnetic Spectrometer on the International Space Station: Precision Measurement of the Positron Fraction in Primary Cosmic Rays of 0.5–350 GeV," *Phys.Rev.Lett.* **110** (2013) 141102.

[240] L. Bergstrom, T. Bringmann, I. Cholis, D. Hooper, and C. Weniger, "New Limits on Dark Matter Annihilation from AMS Cosmic Ray Positron Data," *Phys.Rev.Lett.* **111** (2013) 171101, arXiv:1306.3983 [astro-ph.HE].

[241] **AMS** Collaboration, M. Aguilar *et al.*, "Antiproton Flux, Antiproton-to-Proton Flux Ratio, and Properties of Elementary Particle Fluxes in Primary Cosmic Rays Measured with the Alpha Magnetic Spectrometer on the International Space Station," *Phys.Rev.Lett.* **117** (2016) 091103.

[242] A. Cuoco, M. Krämer, and M. Korsmeier, "Novel Dark Matter Constraints from Antiprotons in Light of AMS-02," *Phys.Rev.Lett.* **118** (2017) 191102, arXiv:1610.03071 [astro-ph.HE].

[243] I. Cholis, T. Linden, and D. Hooper, "A Robust Excess in the Cosmic-Ray Antiproton Spectrum: Implications for Annihilating Dark Matter," *Phys.Rev.* **D99** (2019) 103026, arXiv:1903.02549 [astro-ph.HE].

[244] F. Donato, N. Fornengo, and P. Salati, "Anti-deuterons as a signature of supersymmetric dark matter," *Phys.Rev.* **D62** (2000) 043003.

[245] E. Carlson, A. Coogan, T. Linden, S. Profumo, A. Ibarra, and S. Wild, "Antihelium from Dark Matter," *Phys.Rev.* **D89** (2014) 076005, arXiv:1401.2461 [hep-ph].

[246] M. Cirelli, N. Fornengo, M. Taoso, and A. Vittino, "Anti-helium from Dark Matter annihilations," *JHEP* **1408** (2014) 009, arXiv:1401.4017 [hep-ph].

[247] A. Coogan and S. Profumo, "Origin of the tentative AMS antihelium events," *Phys. Rev.* **D96** no. 8, (2017) 083020, arXiv:1705.09664 [astro-ph.HE].

[248] **ATLAS** Collaboration, "$E_{\mathrm{T}}^{\mathrm{miss}}$ performance in the ATLAS detector using 2015-2016 LHC p-p collisions,".

[249] **CMS** Collaboration, "Performance of missing energy reconstruction in 13 TeV pp collision data using the CMS detector,".

[250] U. Haisch and G. Polesello, "Searching for dark matter in final states with two jets and missing transverse energy," *JHEP* **1902** (2019) 128, arXiv:1812.08129 [hep-ph].

[251] **ATLAS** Collaboration, M. Aaboud *et al.*, "Search for new phenomena using the invariant mass distribution of same-flavour opposite-sign dilepton pairs in events with missing transverse momentum in $\sqrt{s} = 13$ TeV pp collisions with the ATLAS detector," *Eur.Phys.J.* **C78** (2018) 625, arXiv:1805.11381 [hep-ex].

[252] **ATLAS** Collaboration, M. Aaboud *et al.*, "Search for dark matter at $\sqrt{s} = 13$ TeV in final states containing an energetic photon and large missing transverse momentum with the ATLAS detector," *Eur.Phys.J.* **C77** (2017) 393, arXiv:1704.03848 [hep-ex].

[253] **CMS** Collaboration, S. Chatrchyan *et al.*, "Observation of a New Boson at a Mass of 125 GeV with the CMS Experiment at the LHC," *Phys.Lett.* **B716** (2012) 30–61.

[254] D. Dercks, N. Desai, J. S. Kim, K. Rolbiecki, J. Tattersall, and T. Weber, "CheckMATE 2: From the model to the limit," *Comput.Phys.Commun.* **221** (2017) 383–418, arXiv:1611.09856 [hep-ph].

[255] T. Sjostrand, S. Mrenna, and P. Z. Skands, "A Brief Introduction to PYTHIA 8.1," *Comput.Phys.Commun.* **178** (2008) 852–867, arXiv:0710.3820 [hep-ph].

[256] **DELPHES 3** Collaboration, J. de Favereau *et al.*, "DELPHES 3, A modular framework for fast simulation of a generic collider experiment," *JHEP* **1402** (2014) 057, arXiv:1307.6346 [hep-ex].

[257] M. Cacciari, G. P. Salam, and G. Soyez, "FastJet User Manual," *Eur.Phys.J.* **C72** (2012) 1896, arXiv:1111.6097 [hep-ph].

[258] A. L. Read, "Presentation of search results: The CL(s) technique," vol. G28, pp. 2693–2704. 2002.

[259] F. Domingo, J. S. Kim, V. Martin-Lozano, P. Martin-Ramiro, and R. Ruiz de Austri, "Confronting the neutralino and chargino sector of the NMSSM to the multi-lepton searches at the LHC," arXiv:1812.05186 [hep-ph].

[260] A. Belyaev *et al.*, "Advancing LHC probes of dark matter from the inert two-Higgs-doublet model with the monojet signal," *Phys.Rev.* **D99** (2019) 015011, arXiv:1809.00933 [hep-ph].

[261] A. Belyaev, G. Cacciapaglia, I. P. Ivanov, F. Rojas-Abatte, and M. Thomas, "Anatomy of the Inert Two Higgs Doublet Model in the light of the LHC and non-LHC Dark Matter Searches," *Phys.Rev.* **D97** (2018) 035011, arXiv:1612.00511 [hep-ph].

[262] P. De Salas, S. Gariazzo, O. Mena, C. Ternes, and M. Tórtola, "Neutrino Mass Ordering from Oscillations and Beyond: 2018 Status and Future Prospects," *Front.Astron.Space Sci.* **5** (2018) 36, arXiv:1806.11051 [hep-ph].

[263] M. Cirelli, N. Fornengo, and A. Strumia, "Minimal dark matter," *Nucl.Phys.* **B753** (2006) 178–194.

[264] M. Klasen, C. E. Yaguna, and J. D. Ruiz-Alvarez, "Electroweak corrections to the direct detection cross section of inert higgs dark matter," *Phys.Rev.* **D87** (2013) 075025, arXiv:1302.1657 [hep-ph].

[265] D. Griffiths, *Introduction to elementary particles*.